

Forensic Testing of Post Tensioned Concrete Girders

Final Report
July 2014

Wing Hong (Louis) Lo
Graduate Student
Utah State University
Logan UT 84332

Paul J. Barr
Professor
Utah State University
Logan UT 84332

Marv W. Halling
Professor
Utah State University
Logan UT 84332

External Project Manager
Russ Scovil
Utah Department of Transportation

In cooperation with
Rutgers, The State University of New Jersey
And
State of Utah
Department of Transportation
And
U.S. Department of Transportation
Federal Highway Administration

Disclaimer Statement

The contents of this report reflect the views of the authors, who are responsible for the facts and the accuracy of the information presented herein. This document is disseminated under the sponsorship of the Department of Transportation, University Transportation Centers Program, in the interest of information exchange. The U.S. Government assumes no liability for the contents or use thereof.

TECHNICAL REPORT STANDARD TITLE PAGE

1. Report No. CAIT-UTC-033	2. Government Accession No.	3. Recipient's Catalog No.	
4. Title and Subtitle Forensic Testing of Post Tensioned Concrete Girders		5. Report Date July 2014	
		6. Performing Organization Code CAIT/Utah State	
7. Author(s) Wing Hong (Louis) Lo, Paul J. Barr, Marv W. Halling		8. Performing Organization Report No. CAIT-UTC-033	
9. Performing Organization, Name and Address Center for Advanced Infrastructure and Transportation Utah State University 4110 Old Main Hill Logan, UT 84332		10. Work Unit No.	
		11. Contract or Grant No. DTRT12-G-UTC16	
12. Sponsoring Agency Name and Address Center for Advanced Infrastructure and Transportation Rutgers, The State University of New Jersey 100 Brett Road Piscataway, NJ 08854		13. Type of Report and Period Covered Final Report 7/1/13 - 7/6/2014	
		14. Sponsoring Agency Code	
15. Supplementary Notes U.S Department of Transportation/Research and Innovative Technology Administration 1200 New Jersey Avenue, SE Washington, DC 20590-0001			
16. Abstract Recently, two separate Interstate 15 highway bridges over the 400 South roadway in Orem, Utah were demolished after 50 years of service. A total of four post-tensioned girders were salvaged from both the north-bound and south-bound bridge. A series of tests was performed with these girders in the System Material And Structural Health Laboratory (SMASH Lab). The girders were tested with different loading criteria to determine the strength and material properties of the girder. The experimental results were compared with the American Association of State Highway and Transportation Officials Load Resistance Factored Design (AASHTO LRFD) Bridge Design Specifications and a finite-element model using ANSYS. The AASHTO LRFD Specification was fairly conservative on predicting capacity and capable of predicting the type of failure that occurred. The ANSYS model was developed and calibrated to model the girder behavior. The concrete properties in the model were significantly adjusted in order to be comparable to the experimental results. Further exploration in ANSYS needs to be done to precisely model the actual behavior of the girder.			
17. Key Words Accelerated Bridge Construction, Precast, Deck, Panels, Losses		18. Distributional Statement	
19. Security Classification Unclassified	20. Security Classification (of this page) Unclassified	21. No. of Pages 113	22. Price

Contents

Chapter 1 INTRODUCTION.....	1
Chapter 2 LITERATURE REVIEW	2
Comparison of Prestress Losses for a Prestress Concrete Bridge Made with High-Performance Concrete (Barr et al., 2008).....	2
Dynamic Characteristic of Post-tensioned Girder with web openings (Grace et al., 1996).....	3
Parametric Study of Posttensioned Inverted-T Bridge System for Improved Durability and Increased Span-to-Depth Ratio (Nayal et al., 2010)	6
Testing of Two 50-Year-Old Precast Post-Tensioned Concrete Bridge Girders (Eder et al., 2005)	8
Structural Evaluation of a 34-Year-Old Precast Post-Tensioned Concrete Girder (Habib Tabatabai, Timothy J. Dickson, 1993).....	9
Evaluation of Effective Prestress Force in 28-Year-Old Prestressed Concrete Bridge Beams (Pessiki et al., 1996)	11
Chapter 3 BRIDGE DESCRIPTION	13
Girder Description	14
Girder Reinforcements.....	16
Chapter 4 EXPERIMENTATION	19
Moment Cracking Test	22
Capacity Testing	26
<i>Flexural Capacity Test</i>	27
<i>1-d Test</i>	32
<i>2-d & 4-d Test</i>	37
Summary of the experimental results.....	45
Chapter 5 COMPARISON OF TESTED RESULTS TO AASHTO LRFD DESIGN AND ANSYS.....	48
Prestressing losses.....	48
Moment Capacity.....	59
Shear Capacity	63
Finite Element Modeling	72

CONCLUSION.....	90
REFERENCE.....	92
APPENDIX A. Cracking Moment Test Data.....	93
APPENDIX B. Bridge Plans	95
APPENDIX C. ANSYS Model Code.....	101

List of Figures

Figure 1 Elevation view of the bridge.....	13
Figure 2 Cross section of the bridge	14
Figure 3 Side view of the girder.....	15
Figure 4 Cross section at the midspan (Section A-A).....	15
Figure 5 Cross section at the end span (Section B-B).....	16
Figure 6 Configuration of the post-tensioned steel rods	18
Figure 7 Mild reinforcing of the girders	18
Figure 8 Set up with the reaction frame and two girders	19
Figure 9 Girders being tested	20
Figure 10 General Loading Schematic.....	20
Figure 11 Positions of Strain Gauges.....	22
Figure 12 Strain gauge attached across the crack on bottom of girder	23
Figure 13 Girder 7 cracking moment test data.....	24
Figure 14 Cracking during midspan flexural test.....	28
Figure 15 Ultimate failure for midspan flexural test.....	29
Figure 16 Moment vs. Deflection for midspan flexural test	29
Figure 17 Shear vs. Deflection for midspan flexural test.....	30
Figure 18 Longitudinal strain distribution at the midspan	31
Figure 19 Longitudinal strain distribution at the third span.....	31
Figure 20 Set up for 1-d tests	32
Figure 21 Shear vs. Deflection plot for G2-1d(a)	33
Figure 22 Shear vs. Deflection plot for G2-1d(b).....	34
Figure 23 Moment vs. Deflection plot for G2-1d(a).....	35
Figure 24 Moment vs. Deflection plot for G2-1d(b).....	36
Figure 25 Cracks under the loading location prior to ultimate failure	36
Figure 26 Diagonal cracks near the support.....	37
Figure 27 Compressive failure for G2-1d(a).....	37
Figure 28 Cracks and crushes prior to failure	38
Figure 29 Shear failure in G1-2d(a).....	39
Figure 30 Moment vs. Deflection plot for G1-2d(a).....	40
Figure 31 Moment vs. Deflection plot for G7-2d(b).....	40
Figure 32 Shear vs. Deflection plot for G1-2d(a)	41
Figure 33 Shear vs. Deflection plot for G7-2d(b).....	41
Figure 34 Compressive failure in G7-4d(a)	42
Figure 35 Moment vs. Deflection plot for G7-4d(a).....	43
Figure 36 Moment vs. Deflection plot for G1-4d(b).....	43
Figure 37 Shear vs. Deflection plot for G7-4d(a)	44
Figure 38 Shear vs. Deflection plot for G1-4d(b).....	44
Figure 39 Overall shear results vs. distance, αL	47

Figure 40 Overall moment results vs. distance, αL	47
Figure 41 Strut-and-tie model of the girder	69
Figure 42 Defined stress-strain curve in ANSYS for the post-tensioned steel	74
Figure 43 Geometric Shape for SOLID65	75
Figure 44 Geometric Shape for LINK8	76
Figure 45 Geometric Shape for CONTA173&TARGE170.....	77
Figure 46 Reinforcing smearing in the deck	78
Figure 47 Initial deformation due to prestressing	79
Figure 48 Elevation view of the 1-d test FEM.....	79
Figure 49 Comparison of the crack propagation near loading location for 1-d test (left: G3-1d(a), right: FEM).....	80
Figure 50 Overview of cracks from the 1-d test FEM	80
Figure 51 Shear vs. deflection curve comparison for 1-d test.....	81
Figure 52 Elevation view of the 2-d test FEM.....	82
Figure 53 Elevation view of the 4-d test FEM.....	83
Figure 54 Comparison of the crack propagation near loading location for 2-d test (left: G1-2d(a), right: FEM).....	83
Figure 55 Comparison of the crack propagation near loading location for 4-d test (left: G7-4d(a), right: FEM).....	83
Figure 56 Overview of cracks from the 2-d test FEM	84
Figure 57 Overview of cracks from the 4-d test FEM	84
Figure 58 Shear vs. deflection curves comparison for 2-d test	85
Figure 59 Shear vs. deflection curves comparison for 4-d test	85
Figure 60 Elevation view of the midspan test FEM.....	86
Figure 61 Comparison of the crack failure near loading location for midspan test (left: G8-midspan, right: FEM).....	87
Figure 62 Overview of cracks from the midspan test FEM	87
Figure 63 Moment vs. deflection curves comparison for midspan test	88

List of Tables

Table 1 Dimensions for each test.....	21
Table 2 Prestressing values for each girder.....	26
Table 3 Overall results for all tests	45
Table 4 Prestress losses using Simplified Method.....	52
Table 5 Time-dependent losses from Refined Method.....	58
Table 6 Prestress losses using Refined Method.....	58
Table 7 Comparison on Effective prestress with different methods	59
Table 8 k value for different types of tendon	62
Table 9 Comparison of the theoretical moment capacity to measured value for each test	62
Table 10 Components in shear capacity for each shear test.....	67
Table 11 Comparison of theoretical shear capacities to measured for each shear test	68
Table 12 Corresponding Material Numbers.....	73
Table 13 Comparison of the capacity between the experimental and FEM results	89

Chapter 1

INTRODUCTION

The 400 South Interstate 15 bridge in Orem, Utah was demolished after 50 years of service. Four girders (two interior girders and two exterior girders) were salvaged from the demolition and further tested in this research. The girders had an AASHTO Type-I cross section with box ends on the each end. The bridge girders were originally designed as a prestressed girder with prestressing strands, however the girders were found to be prestressed by post-tensioned rods. This research is focused on the shear and flexural strength as well as the prestress losses in the girders. The prestress loss of each girder was determined by performing a cracking moment test, where each of the girders was loaded with a point load at the midspan to induce a cracking moment. The capacity tests were performed on each girder by loading the girders until complete failure. Each girder was loaded at different locations along the girder span in order to induce flexural, flexural-shear, and shear failure. Furthermore, the results from the capacity tests were compared with the AASHTO LRFD Specification (AASHTO 2012) as well as a finite-element model using ANSYS. The comparison with the AASHTO 2012 was performed to verify that the predicted capacity from AASHTO 2012 was conservative. The ANSYS model was developed to replicate the girder behavior. The model was then compared to the actual properties of the girder to find the accuracy of the ANSYS modeling on post-tensioned concrete girders.

Chapter 2

LITERATURE REVIEW

Comparison of Prestress Losses for a Prestress Concrete Bridge Made with High-Performance Concrete (Barr et al., 2008)

This research was focused on comparing the experimentally determined prestress losses of high-performance concrete to the predicted losses calculated using the AASHTO LRFD and a HPC method that was based on the findings from NCHRP 18-06. The data was obtained by monitoring a bridge on the SR18/SR516 in the state of Washington for 3 years from the time of casting. This bridge was a precast, prestressed three-span bridge with two span length of 23.3 m (76.4 ft) long of the first and third spans and 40.6 m (133 ft) long for the second span. The width of the bridge was 11.6 m (38 ft) which carries two lanes of traffic. There were five prestressed concrete girders fabricated with high-performance concrete tested in this research. These five girders were from the first and the third girders from Span 1, and the first three girders from Span 2. Each girder was constructed with the Washington W74MG girder cross-section that had a depth of 1867 mm (73.5 in.). Each girder was monitored using four vibrating-wire strain gages with integral thermistors at two 1.52 m (5 ft) from the girder end nearest Pier 2 and at midspan. At each instrumentation location, gages were placed at the bottom of each girder and in the web to monitor the concrete temperature and longitudinal strains.

The test results showed that average measured prestress losses for the Span 2 girders were 385 MPa (55.8 ksi) corresponding to 27.5% of the jacking stress. For the Span 1 instrumented girders the average measured losses were 227 MPa (32.9 ksi) corresponding to 16.2% of the jacking stress. The major sources of these losses were from elastic shortening,

creep, and shrinkage, while the relaxation of the steel was neglected due to its minimal effect. A comparison was performed of the measured and predicted prestress loss after nearly 3 years using the AASHTO LRFD and NCHRP 18-07 method. The AASHTO LRFD prestress loss was 20.0% higher than average measured prestress loss for the Span 2 girder. In contrast, the predicted prestress losses using the NCHRP 18-07 method was 16% smaller. For the Span 1 girders, the AASHTO LRFD calculated loss was within 2% of the measured loss, while calculated loss from the NCHRP 18-07 method was about 22% smaller than the measured value.

This research focused on four major sources of prestress losses, which were elastic shortening, creep and shrinkage, and differential shrinkage. The result showed that the AASHTO LRFD method predicted smaller loss magnitude in comparison to the measured values in terms of the elastic shortening losses for both Span 1 and Span 2 girders. However, the calculated prestress loss values from the NCHRP method were relatively closer to the measured losses. Regarding the creep and shrinkage losses, the AASHTO LRFD method overestimated the losses for the Span 2 girder but not for the Span 1 girder. On the other hand, the NCHRP method underestimated the losses for both Span 1 and Span 2 girders. For the differential shrinkage losses, the NCHRP procedure predicted a fairly close magnitude of the average measured losses for both the Span 1 and Span 2 girders. The AASHTO LRFD method does not explicitly include differential shrinkage into the prestress loss calculations.

Dynamic Characteristic of Post-tensioned Girder with web openings (Grace et al., 1996)

This study focused on investigating the dynamic characteristics of post-tensioned concrete girders with web openings. The investigation was performed with experimental and

analytical specimens subjected to a repeated cyclic loading. There were nine girders constructed and tested with span lengths of 5.0 m (16 ft 5 in.). The girders were cast in groups of three based on their cross-sectional shapes, which were rectangular, T, and I shape. The size of the rectangular girders was 76 mm (3 in.) wide by 203 mm (8 in.) deep. For the T shape, the flange width was 178 mm (7 in.) with a depth of 51 mm (2 in.) and the web had the same size as the rectangular girders. The I-shape girders also had a 178 by 51 mm (7 by 2 in.) flange and a 76 mm (3 in.) wide by 152 mm (6 in.) deep web. Each of the three groups contained three girders constructed with none, one, and two web openings located vertically at the neutral axis of the cross-section and longitudinally at midspan. The openings had a depth of 7.64 cm (3 in.) and width of 40.75 cm (16 in.). The web of each girder was reinforced with two #3 rebars at the top and bottom, and one straight post-tensioned 7-wire strand at one-quarter of the cross-section from the top, plus two post-tensioned 7-wire strands in parabolic shape. The nominal diameter of the strands was 7.94 mm (5/16 in.). The parabolic strands were 25 mm (1 in.) below the neutral axis at the end points. Moreover, for T and I shape girder, there were two extra #3 rebars placed at the flange. Shear reinforcement was placed with a spacing of 15.28 cm (6 in.) through the entire span of each girder but the spacing was reduced to 2.54 cm (1 in.) at the ends and in the regions to each side of the opening.

There were five different tests used to experimentally investigate the girder behavior. They were impact load test, log-decrement test, fatigue load test, static load test, and ultimate load test. The impact load test was used to determine the natural frequencies for each girder through the frequency spectrum response. Subsequently the log-decrement test was used to quantify the damping characteristics. Finally, stiffness, strains, and prestress forces were measured and recorded during the fatigue load test, static load test, and ultimate load test.

Regarding the natural frequencies of each girder, an additional analytical study was utilized to determine the theoretical natural frequencies and the corresponding mode shapes of vibration of the girders. The GTSTRUDL finite element analysis computer program was used to complete the theoretical analysis.

Regarding the natural frequency, the result from both the experimental and theoretical analysis showed that the natural frequency of mode shape 1 had a minimal effect for each girder. However, the placement of web openings significantly affected the natural frequency of mode shape 2. The largest decrease was 16.5% for the I-shape girder with two web openings. The damping ratios were also determined before and after fatigue loading in order to quantify the effect on the damping characteristics for each girder due to fatigue loading. However, there was negligible effect on the damping characteristics of the girders. The cracking patterns were recorded. The cracks were preliminarily concentrated within the midspan region near the web openings due to shear stress and at the bottom of the girder due to flexural stress. Finally, for the ultimate load test, the changes of prestress force and deflection responses were monitored during loading. The results showed that the prestress force remained nearly constant for the top post-tensioned strand until the load was approximately 26.7 kN (6 kips), then the prestress force suddenly increased at the ultimate load, which was 31.15 kN (7 kips). However, the prestress forces of the bottom two parabolic strands exponentially increased until 26.7 kN (6 kips). Likewise, these two strands had large increases between 26.7 and 31.15 kN (6 and 7 kips). Additionally, the deflection responses were approximately linear until 10 kN (2.25 kips). Based on the results of the ultimate load test, the placement of web openings did not significantly affect the overall capacity and deflection response for T and I shape girders but it reduced the ductility

of the girders. For rectangular girders, the load carrying capacity was reduced depending on the placement of web openings.

Parametric Study of Posttensioned Inverted-T Bridge System for Improved Durability and Increased Span-to-Depth Ratio (Nayal et al., 2010)

This study was conducted to investigate the major parameters that limit the performance of a post-tensioned Invert-T (PT-IT) bridge system in order to improve the durability and span-to-depth ratio of PT-IT girders. In this research, five major parameters influenced the performance of the PT-IT bridge system, which were section properties, construction scenario, concrete strength, creep and shrinkage model, and timing.

Regarding the section properties, there were six standard IT-shape cross sections including IT 500, IT 600, IT 700, IT 800, IT 900, and IT 1000. Three concrete compressive strengths were utilized for both the girders and deck, which were 41.37, 55.16, and 68.95 MPa (6, 8, and 10 ksi) for girders and 20.68, 24.13, and 27.58 MPa (3, 3.5, and 4 ksi) for the deck. In order to analyze the creep-and-shrinkage effect, five standard models including AASTO LRFD, American Concrete Institute (ACI) 2009, Comite Euro-International du Beton-Federation International de la Precontrainte (CEB-FIP) 90, National Highway Research Program (NCHRP) 496, and self-consolidating concrete (SCC) were compared. There were four construction scenarios considered for this study in terms of the order of casting and times of post-tensioning. The first scenario was casting the deck and diaphragm concrete at the same time to provide continuity, and then applied post-tensioning to the entire system after the concrete hardened. The second scenario was casting the diaphragm concrete first to provide continuity, then applying the post-tensioning to the IT-section only when the concrete hardened, and cast the deck last. The

third construction scenario was casting the deck after the diaphragm was cast and hardened, and then applying post-tensioning to the entire system. The last scenario contained two stages of post-tensioning. In this scenario, the diaphragm was cast first, then after it hardened, post-tensioning was applied to balance stresses due to the weight of the deck. As soon as the deck was cast and hardened, the second stage of post-tensioning was applied to balance stresses due to the weight of barriers and live load. Lastly, the timing factor for this parametric study was defined by three categories. These three categories were the age of girder when cutting prestressing strands, the time from casting of the deck to applying the post-tensioning, and the time from cutting the prestressing strands to casting the deck.

In conclusion, the construction scenario was determined to be the third option as the best option because of its cost effectiveness, highest span-to-depth ratio, and crack-free deck criteria. Also, the result showed that the increase of the concrete strength of the girder significantly increased the maximum possible span length of the girder. Regarding the creep-and-shrinkage models investigated, there was no significant effect on the estimation of prestress losses in pretensioning strands and post-tensioning tendon but the time-dependent restraining moments were noticeably affected. In the consideration of the effect of timing, the diaphragm concrete was recommended to be cast between two and four months after the girder's casting while the concern for the timing of casting deck concrete was redundant. The recommendation also showed that the post-tensioning force needed to be applied shortly after casting the deck.

Testing of Two 50-Year-Old Precast Post-Tensioned Concrete Bridge Girders (Eder et al., 2005)

Two 50-year-old, I-shape, post-tensioned concrete bridge girders were salvaged from a bridge in Hamilton County, Ohio. The girders were tested in order to determine their ultimate strength for reference to similar girders in service. The two I-shape girders were constructed as a 13.7 m (45 ft) long precast concrete girders with four 29 mm (1-1/8 in.) diameter post-tensioned steel bars. These two girders had a depth of 1016 mm (40 in.) with a 152 mm (6 in.) wide web and 406 mm (16 in.) wide flanges. Two bars were placed at the center of the web and bent at 1.37 m (4.5 ft) apart from the midspan to create a harped profile. Another two straight bars were located at the bottom flange. No. 4 shear reinforcement was utilized at the spacing of 230 mm (9 in.) along the entire length of the girder. A 197-mm (7.75-in.) thick concrete deck was cast prior to testing in order to perform a more realistic in-situ experiment. The concrete compressive and tensile strength of the girders were measured using four compression tests and two split cylinder tests. The average measured compressive strength was 68 MPa (9.8 ksi) and the average measured tensile strength was 6.3 MPa (800 psi). The yield strength of the post-tensioned steel bars was 700 MPa (100 ksi), whereas the tensile strength and elastic modulus were also measured to be 1000 MPa (144 ksi) and 175 GPa (25,300 ksi), respectively.

During the test, cracking visibly initiated at approximately 400 kN (90 kips) of applied load at midspan. Additionally, the cracking moment due to the applied load and a total cracking moment due to both dead load and the applied load were calculated, which were 976 and 1123 kN-m (720 and 828 kip-ft), respectively. The actual moment capacity was also determined by using the measured concrete and steel strength. The analytical capacity was calculated as 2130

kN-m (1570 kip-ft). According to the experimental results, the maximum applied loads were 693 and 670 kN (156 and 151 kips) at midspan for Girder 1 and Girder 2. These loads correspond to maximum moments at midspan of 1690 and 1640 kN-m (1248 and 1208 kip-ft), and the total maximum moment due to both dead load and maximum applied load were 1839 and 1784 kN-m (1356 and 1316 kips-ft). Regarding the post-tensioning forces in the steel bars, the post-tensioning force per bar was calculated to be 223 kN (50 kips) corresponding to a stress of 414 MPa (50 ksi). The post-tensioning losses could not be determined in this study because of the unavailability of information. However, an estimated post-tensioning loss of 37 percent was reasonably assumed given that the yield strength of the bar was 700 MPa (100 ksi).

Structural Evaluation of a 34-Year-Old Precast Post-Tensioned Concrete

Girder (Habib Tabatabai, Timoth J. Dickson, 1993)

A load test of a bridge girder built in 1958 was performed for the study at Skokie, Illinois. The bridge girder was removed from the I-94 bridge over US 81 in Fargo, North Dakota. The purpose of the test was to compare the cracking moment and flexural capacity of the girder with the predicted values. The moment-curvature and load-deflection relationships were also compared between measured result and analytical predicted result.

The tested girder had a length of 13.2 m (43 ft 4 in.) with an AASHTO Type-II cross-section. It contained three post-tensioning tendons arranging in two layers at the bottom. The top tendon included 16 wires that were 6 mm (0.25 in.) in diameter and 12 that were 6 mm (0.25 in.) in diameter for the bottom two tendons. The distance between the centroid of tendons and the

centroid of the cross section was 97 mm (3.83 in.) at the girder ends and 275 mm (10.83 in.) at the midspan.

The load test was designed with two symmetric point loads applied near both ends so that a constant moment region was produced within the midspan region. Also, there were a total of nine strain gauges in groups of three that were attached on the tested girder. Those three sets were all longitudinally located at the midspan region and they were vertically located at the top of the girder, the compressive zone of the girder, and the bottom of the girder, respectively along the depth of the girder. The test included a cracking load and an ultimate load test. Both tests were used to determine the cracking moment, decompression load, and the moment strength. Furthermore, material property tests were performed. Three cores of concrete were extracted from the girder after the failure test and used to determine the compressive strength and the modulus of elasticity of the concrete. Also, four pieces of the post-tensioned wires were tested to determine the modulus of elasticity and the ultimate strength.

Regarding the material properties, the result showed that the average compressive strength was measured to be 74.5 MPa (10,800 psi) and the average concrete modulus of elasticity was 37,600 MPa (5450 ksi). The average ultimate tensile strength of the post-tensioning wire was 1766 MPa (256 ksi) while the average modulus of elasticity was approximately 193,000 MPa (28,000 ksi). The effective prestress in the tendons was measured to be 945 MPa (137 ksi) and the total prestress loss was 17.5%. Regarding the ultimate capacity results, the total moment (applied and self-weight moment) was 934 kN-m (689 kip-ft) where the crack visibly occurred at the midspan. The maximum total moment was 1481 kN-m (1092 kip-ft). At this load, the girder failed in compression at the top flange near the midspan.

Evaluation of Effective Prestress Force in 28-Year-Old Prestressed Concrete Bridge Beams (Pessiki et al., 1996)

The research summarized in this paper was performed with two full-scale, prestressed concrete I-beams, in order to evaluate the effective prestress force within the beams. These two beams were salvaged after a 28-year service life from the Shenango River Bridge on I-80 in Mercer County, Pennsylvania. The beams had a span length of 27.1 m (89 ft) and a depth of 1524 mm (60 in.). The flanges had a width of 610 mm (24 in.) and a depth of 152 mm (6 in.). The web had a width of 203 mm (8 in.). Each beam had a total of 50 11-mm (7/16-in.) diameter prestressed strands where 36 of them were straight and 14 of them were harped.

Four tests were performed in this study, which were cracking load test, decompression load test, ultimate strength test, and material property test. Prior to the cracking load test, four strain gauges were attached on each side of the beam and distributed along the depth of the beam. The externally applied load on the beam was incrementally increased in approximately a step of 26.7 kN (6 kips) until the first crack was visually appeared. The first crack was visually observed on the bottom of the beam at the midspan when the load was approximately 645 kN (145 kips). After the cracks were marked, the beams were repeatedly unloaded and reloaded to determine the decompression load. During the decompression load test, the crack opening was observed visually, and detected using displacement transducers and strain gauges. The average decompression load of the beams was determined to be approximately 489 kN (110 kips). Additionally, the average prestress losses were determined to be about 18%, while the predicted prestress losses were 29, 32 and 33 percent using the Modified Bureau of Public Roads, Lehigh, and AASHTO methods, respectively. At the ultimate strength capacity, the failure occurred due

to crushing of concrete at the compression zone for both beam under the average ultimate load of 1121 kN (252 kips). The average midspan deflection was recorded to be 240 mm (9.45 in.). Lastly, the results from the material property tests showed that the average compressive strength of the concrete was 58.2 MPa (8440 psi), which was 65% greater than the original design strength. The average compressive modulus of elasticity was also determined as 34.1 GPa (4945 ksi).

Chapter 3

BRIDGE DESCRIPTION

For this research, four concrete girders were salvaged from two Orem 400 South Bridges in Utah County, Utah, which was originally constructed in 1962. The two bridges supported three North and Southbound lanes for Interstate-15 and were separated by a 7.47 m (24 ft 6 in.) median. The bridges had a slope of 1.28% longitudinally and 2.08% transversely. These two bridges were constructed symmetrically along the median. Each bridge was comprised by three independent spans where the two end spans were 11.1 m (36 ft 3 in.), and the center span was 11.4 m (37 ft 6 in.). Each bridge deck had a total width of 16.9 m (55 ft 6 in.), which was supported with eleven girders per span with a spacing of 1.52 m (5 ft). Each span was supported laterally with an intermediate diaphragm at the midspan and both end. These two bridges were simply supported with two abutments and two piers. An elevation view is shown in Figure 1. Each abutment was supported by twenty seven 9.14 m (30 ft) concrete piles. Each pier was supported by three 0.914 m by 0.914 m (3 ft by 3 ft) reinforced concrete columns connecting to a 13.7 m long by 2.74 m wide (45-ft long by 9-ft wide) rectangular footing. Each columns footing was supported with six 4.57 m (15 ft) concrete piles.

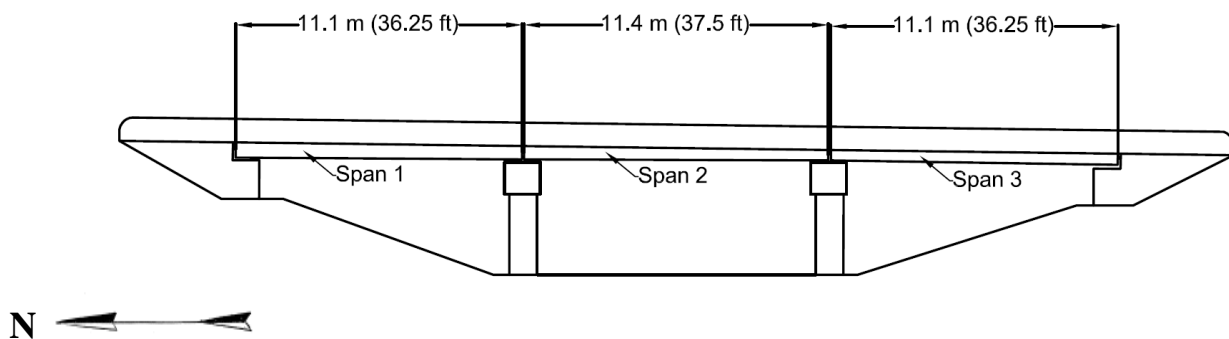


Figure 1 Elevation view of the bridge

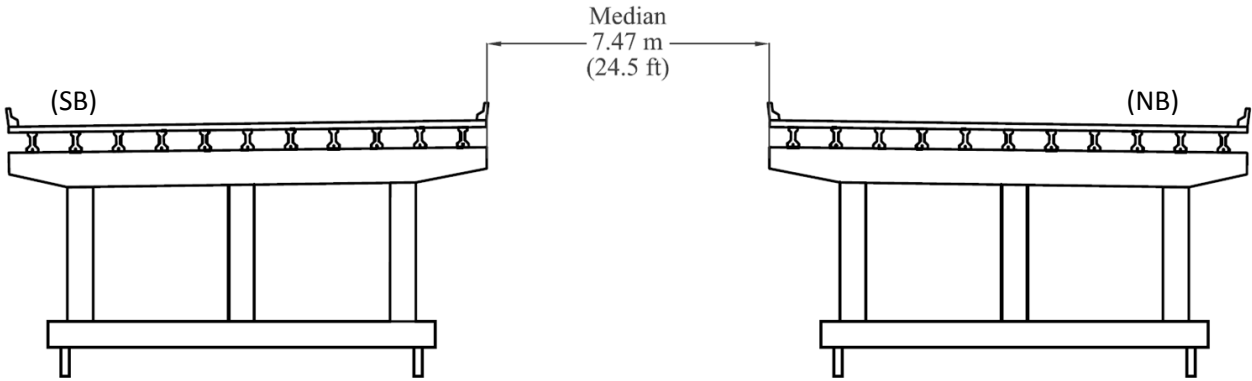


Figure 2 Cross section of the bridge

Girder Description

The four salvaged girders for this research were from the northernmost span (Span 1) of the bridge. Two girders were taken from each of the north and southbound bridge, where one was the interior girder and one was the exterior girder from each bridge. The girders had overall depth of 0.914 m (36 in.) including a 0.2-m (8-in.) concrete decking. A significant damage on the flange after demolition was repaired with new cast-in-place deck concrete. The girder cross section was that of the American Association of State and Highway Transportation Officials (AASHTO) Type-I with box ends, shown in

Figure 4. The box end cross section is shown in Figure 5. The total depth of the girder was 0.711 m (28 in.). The top flange was 0.305 m (12 in.) wide and 0.102 m (4 in.) deep which then tapers into a 0.152-m (6-in.) wide web at a one-to-one slope. The web was 0.279 m (11 in.) tall and angles back to the bottom flange at a one-to-one slope. The bottom flange was 0.406 m (16 in.) wide and 0.127 m (5 in.) tall. The box ends were as wide as the girder with a length of 0.051 m (2 ft) and then tapered back into the web along 0.152 m (0.5 ft) long as shown in Figure 3. In general, box ends were commonly used for post-tensioned girders in order to strengthen the

compressive zone at the end. After post-tensioning the girder, the anchor zone would need to be increased in order to resist the applied compressive forces. The box end design was to prevent the crushing at the end of the girder containing highly concentrated compressive force.

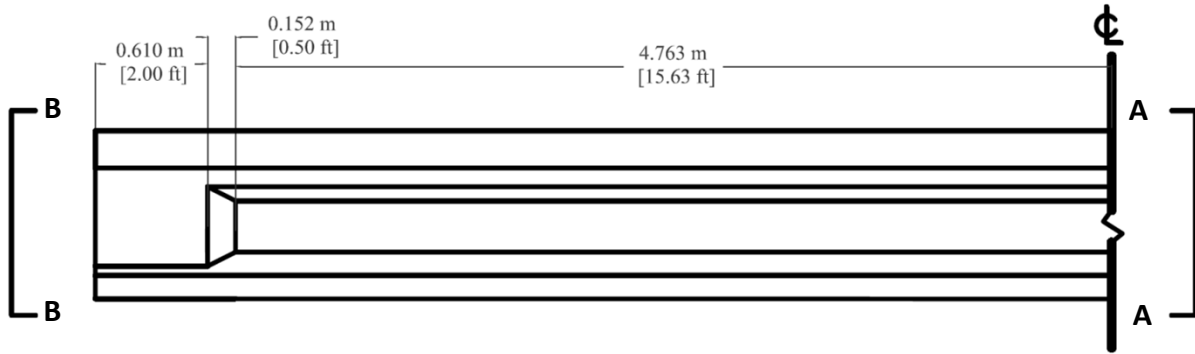


Figure 3 Side view of the girder

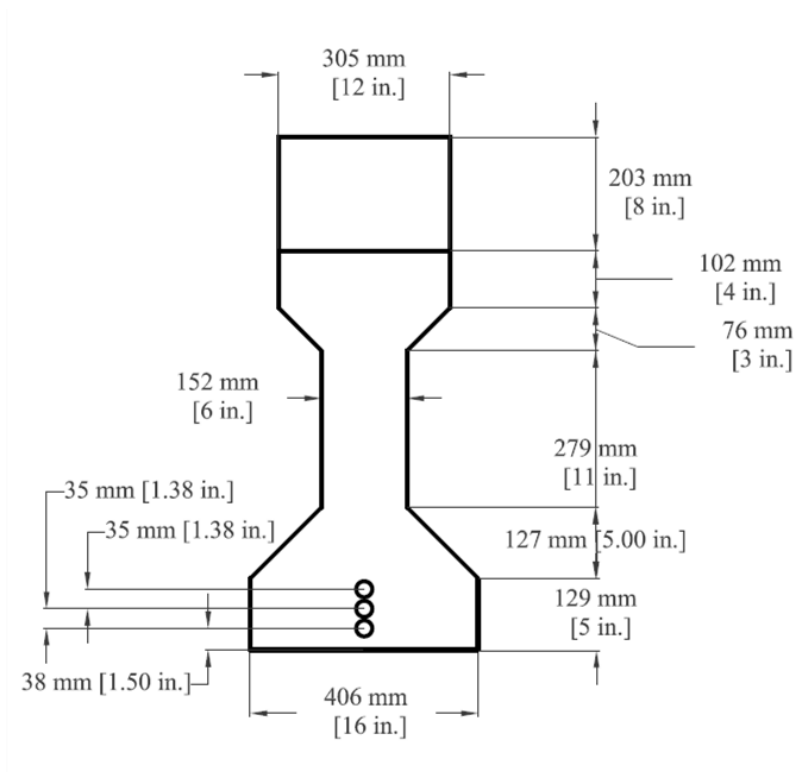


Figure 4 Cross section at the midspan (Section A-A)

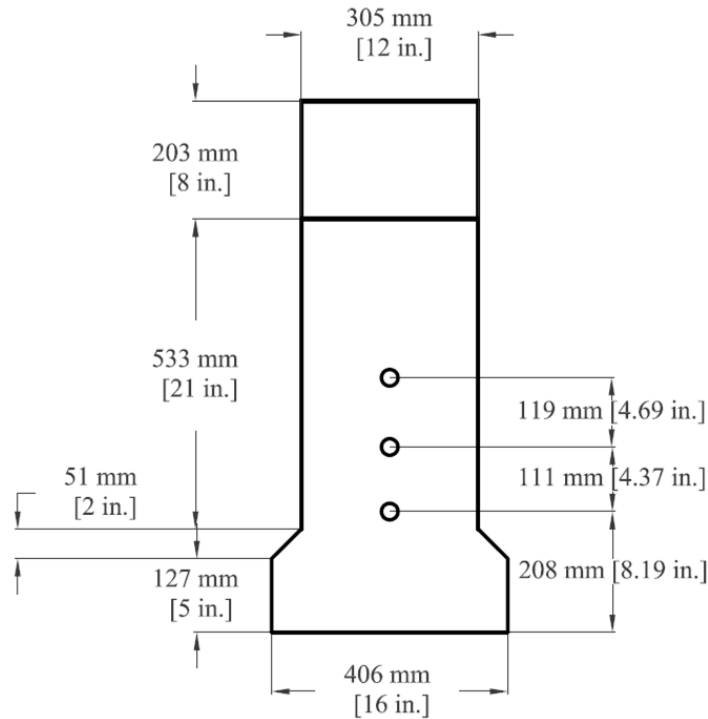


Figure 5 Cross section at the end span (Section B-B)

The compressive strength of the concrete was originally specified to be 27.6 MPa (4,000 psi) at the time of prestressing and 34.5 MPa (5,000 psi) at 28 days. The maximum compressive strength of the concrete was determined experimentally with cored samples and was found to have an average maximum compressive of 51.4 MPa (7460 psi) and 46.4 MPa (6730 psi) for the girder and deck concrete, respectively.

Girder Reinforcements

The prestressing for the tested girders was not the same as shown on the original bridge plan. There were twenty four 9.53-mm (3/8-in.) diameter prestressed strands on the original bridge plan with an ultimate prestressing steel strength of 1.72 GPa (250 ksi). Ten strands in the web were harped at the midspan and fourteen straight strands were specified in the bottom flange at a 50.8 mm (2 in.) center-to-center spacing. Each strand was specified to be pre-tensioned by

62.3 kN (14 kip). After the removal of the girders from the bridge, the actual girders were found to be post-tensioned with three 28.6-mm (1-1/8 in.) diameter post-tensioned steel rods, instead of prestressed strands. The strength of the steel was determined through tensile testing with a result of 965 MPa (140 ksi). The post-tensioned steel rods were placed in a parabolic shape and grouted into a 34.9-mm (1-3/8 in.) diameter corrugated conduit. Each post-tensioned steel rod was anchored at the end of the girder with a steel bearing plate.

The locations of the steel rods along the length of the girder were necessarily determined by measuring because of the inconsistency of the design with the original bridge plan. The elevations of the rods at the end were measured, where the top rod was 0.438 m (17-1/4 in.), the middle rod was 0.319 m (12-9/16 in.), and the bottom rod was 0.208 m (8-3/16 in.) from the bottom of the girder for a centroid of 0.322 m (12.7 in.). The elevations of the rods at the midspan were also measured, where the three conduits were placed tightly next to each other. The edge spacing between the centroid of bottom rod and the bottom of the girder was 0.0381 m (1-1/2 in.) and the center-to-center spacing between rods was 0.0349 m (1-3/8 in.) as the same as the diameter of the conduit providing a centroid at the midspan of 0.073 m (2.88 in.). By having two sets elevations through measuring, the elevations of the parabolic rods at different location were determined by fitting a simply quadratic equation with two given points. The configurations of the post-tensioned steel bars are shown in Figure 6.

For the shear and mild reinforcements of the girders, #4 bars were used along the entire length of the girder with a yielding strength of 414 MPa (60 ksi). Four #4 longitudinal bars were placed to hold the stirrups and hoop steels in place during casting. Four #5 hoop steels were used along the depth of the girder at the box end section.

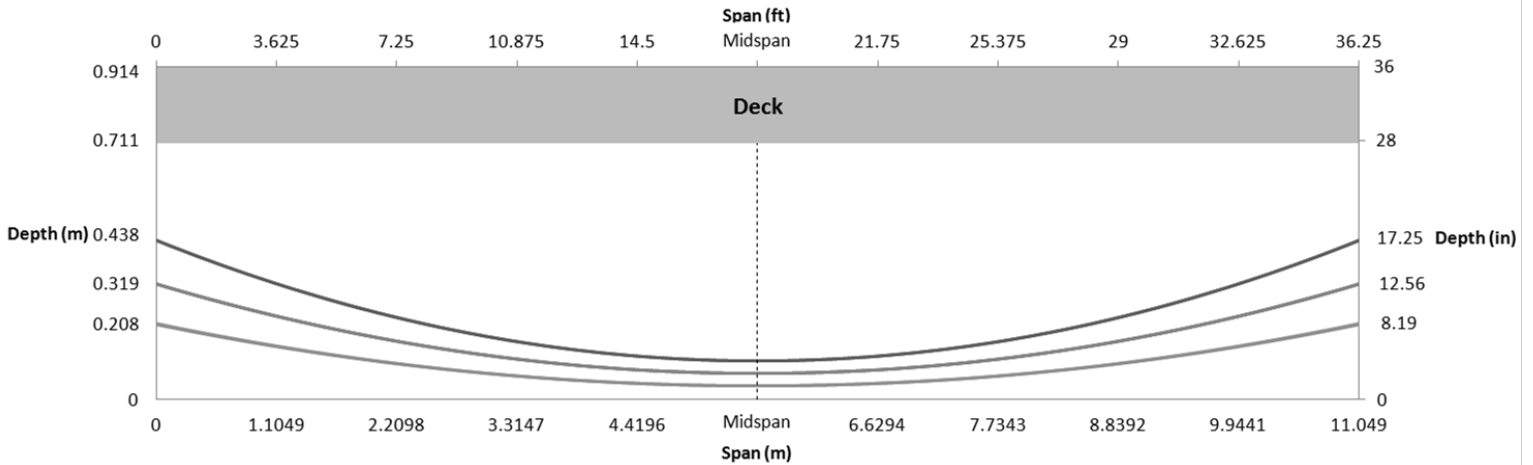


Figure 6 Configuration of the post-tensioned steel rods

The shear reinforcements were two side-by-sides #4 rebars with a top hook extended 0.127 m (5 in.) into the deck. The stirrups started at 0.0381 m (1.5 in.) from the girder end and then had a spacing of 0.152 m (6 in.) for 1.52 m (5 ft). At this point, the stirrup spacing changed to 0.305 m (12 in.) for 7.92 m (26 ft) and then back to a spacing of 0.152 m (6 in.) with a 0.0381 m (1.5 in.) edge spacing at the end. The configuration of shear reinforcements is shown in Figure 7.

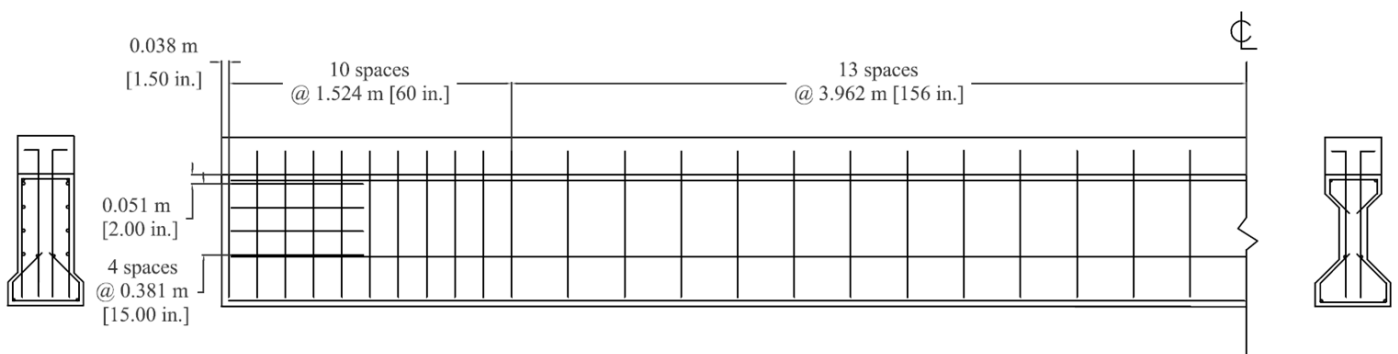


Figure 7 Mild reinforcing of the girders

Chapter 4

EXPERIMENTATION

For this study, four girders were tested to determine the effective prestress force in addition to the flexural and shear capacities. All of the experiments were performed at the System Material and Structural Health Laboratory (SMASH Lab), which is part of the Utah Transportation Center (UTC) at Utah State University. The SMASH Lab is located at 1500 Canyon Road, Logan Utah. It has been used for conducting large-scale structural testing on campus since Spring 2009. The lab is equipped with a strong floor, reaction frame, hydraulic rams, and a Vishay 5000 data acquisition system. The strong floor has a thickness of 0.914 m (3 ft). It is made of reinforced concrete with conduits spaced every 0.914 m (3 ft) in order to adapt the various loading positions of the reaction frame. The reaction frame is a steel frame with two columns, which were bolted to the strong floor through the conduits. The two columns are connected with a steel beam. The hydraulic rams were held at the bottom of the beam. The maximum static load that the ram used in this experiment can apply was 222 kN (500 kip). The Vishay 5000 data acquisition system was utilized for monitoring load cells, strain gauges, and LVDTs that were used for this experiment.



Figure 8 Set up with the reaction frame and two girders



Figure 9 Girders being tested

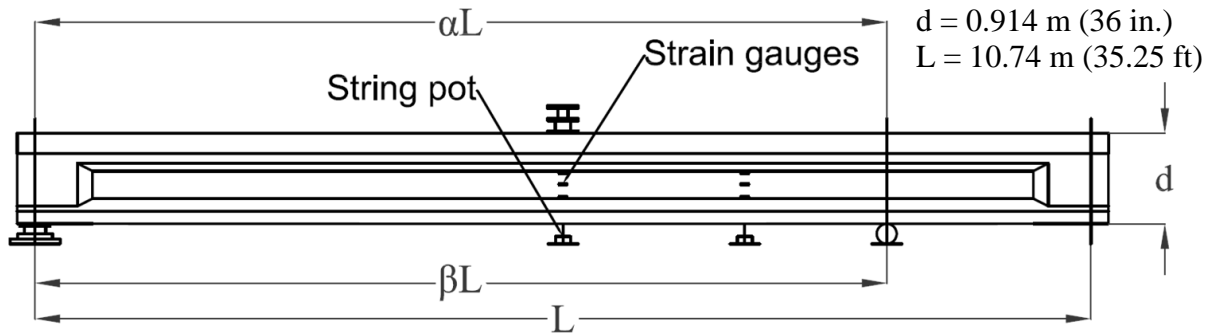


Figure 10 General Loading Schematic

The four tested girders were numbered 1, 2, 7, 8, where another four additional girders (3, 4, 5, 6) were tested for a different study. The numbering was set according to the order of the removal from the bridge. The objective for the experiments was to determine the prestress force with a cracking test and, furthermore, the capacity for either pure moment, predominately shear, or a flexure-shear failure. Four different tests were performed to determine the capacity. They were mid-span, 1- d , 2- d , and 4- d tests, where d was the total depth of the girders including the deck as shown in Figure 10. These four tests represented that the static load was applied at

concentrated location on the girder apart from the support with the corresponding distance, βL , as shown in Table 1.

Table 1 Dimensions for each test

Girder # Test Type	αL	βL
G1-2d (a)	1.83 m (6.00 ft)	10.74 m (35.25 ft)
G1-4d (b)	3.66 m (12.00 ft)	8.50 m (28.00 ft)
G2-1d (a)	0.914 m (3.00 ft)	10.74 m (35.25 ft)
G2-1d (b)	0.914 m (3.00 ft)	9.22 m (30.25 ft)
G7-4d (a)	3.66 m (12.00 ft)	10.74 m (35.25 ft)
G7-2d (b)	1.83 m (6.00 ft)	6.63 m (21.75 ft)
G8 (Mid span)	5.37 m (17.63 ft)	10.74 m (35.25 ft)

For each experiment, strain gauges were used for recording the changes in strain at different locations on the girder. Four strain gauges were attached to the girder at the location of load with four different elevations. Three gauges were placed at the top, the middle, and the bottom of the web, respectively, as shown in Figure 11. The elevations of the gauges from the bottom of the girder were 256 mm (10.0 in.), 393 mm (15.5 in.), and 530 mm (21.0 in.), respectively. The last one was placed at the underside of the bottom flange. All strain gauges were oriented along the longitudinal direction of the girder and only placed on one side of the girder.

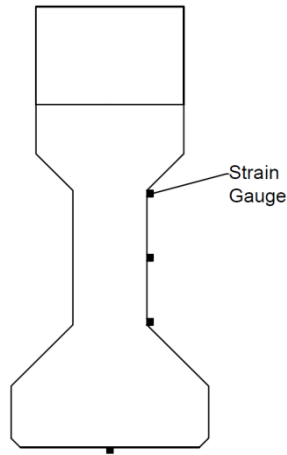


Figure 11 Positions of Strain Gauges

Moment Cracking Test

The moment cracking test was performed by positioning the girders under the reaction frame so that the hydraulic ram could apply a single load at the mid-span of the girder. Each girder end had a 305-mm (12-in.) square steel bearing plate that was placed on the floor directly under the girder. An elastomeric pad was installed in between the plate and the girder. The function of the elastomeric pad was to replicate the in-service bridge girder supports, where it was designed to allow the ends to rotate while still supporting the girder vertically. At the location of applied load, an additional steel plate with the same size was placed on the top of the girder at the mid-span. A spherical bearing was placed and supported by the steel plate. In addition, the bearing was greased to ensure that a pure vertical load was applied during testing. In order to record the magnitude of applied load throughout the test, a load cell was installed between the hydraulic ram and the steel plate.



Figure 12 Strain gauge attached across the crack on bottom of girder

The goal of the moment cracking test was to determine the effective prestress force in the girders. An increasing load was applied at mid-span until the first transverse crack became visible at the bottom flange. The magnitude of the cracking load was then recorded and the location of the crack was marked. Afterward, the girder was unloaded such that the crack closed due to the prestress force. After the load was removed and the crack was completely closed, a 76.2 mm (3 in.) strain gauge was attached across the crack. The girder was then reloaded until the crack was re-opened. A 25% increase of load was applied with the reload in order to ensure that the crack re-opened. The care was taken with the applied reload in order to remain in the elastic range and to avoid permanent damage to the girder.

After the loading of the moment cracking test, the relationship between the applied load and the recorded strain was determined from the load cell and strain gauges. A load versus strain plot was created where the magnitude of the cracking load was determined. The load versus strain plot for Girder 7 is shown in Figure 13.

Girder #7 Cracking Test

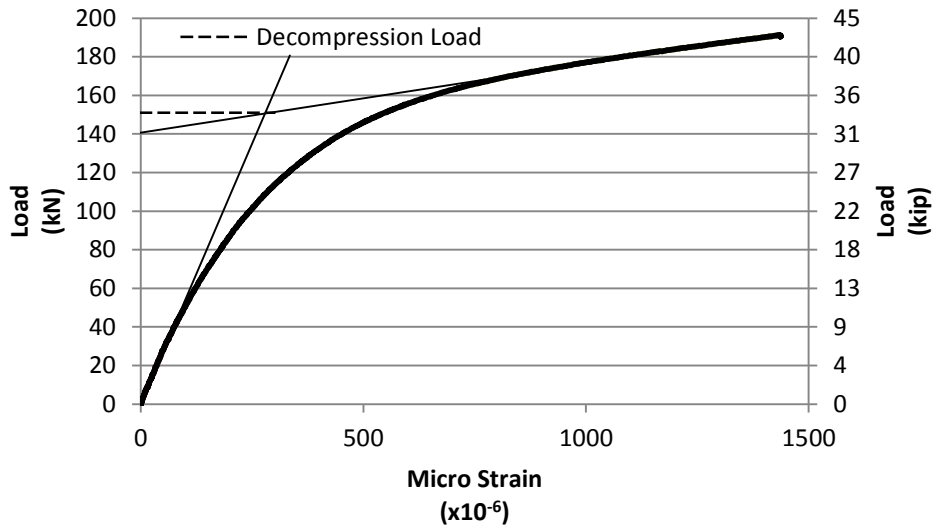


Figure 13 Girder 7 cracking moment test data

The non-linear behavior illustrated that the stiffness of the girder decreased after the crack opened, where the slope of the curve reduced after the crack open. This behavior shows that as the crack was closed, the girder response behaved as an uncracked girder with the full strength due to the completeness of the concrete cross section. However, once the crack opened, the reduction of the cross sectional area subsequently reduced the stiffness of the girder, which is shown by the reduced stiffness and non-linear behavior on the plot.

The decompression load then could be determined from this relationship. The decompression load represents the magnitude of the external load that causes the concrete at bottom of the girder to obtain a magnitude of zero stress. The procedure to determine the decompression load was to find the intersection of the tangent lines of the initial slope and the post cracking slope as shown in Figure 13. The load corresponding to the intersection was

defined as the decompression load for that particular tested girder. The total stress at the bottom of a prestressed concrete girder can be calculated by Eq. 1.

Under the condition with the decompression load, the stress, σ , is zero. Then, Eq. 1 can be used to calculate the total effective prestressing force, P , throughout the entire girder. The prestressing force for each individual rod can be simply calculated by dividing P by the number of post-tensioned rods, which is three for this case. Additionally, prestressing stress on each rod can also be calculated using Eq. 2

The calculated effective prestressing values for the tested girders in comparison to the initial values are shown in Table 2. Since the prestressing design in the plan was different than the actual design, the equivalent initial prestressing values were calculated with the original prestressing force taken from the bridge plan (see Appendix B) and the actual geometry of the post-tensioned rods. The average residual prestressing force was 876 kN (197 kip).

$$\sigma = -\frac{P}{A} - \frac{Pe_{pg}c_g}{I_g} + \frac{M_{sw}c_g}{I_g} + \frac{M_{xt}c}{I}$$

Eq. 1

$$\sigma_{ps} = \frac{P}{A_{ps}}$$

Eq. 2

where

σ = Stress at the bottom of the girder

P = Effective prestressing force

e_p = Eccentricity of the prestressing force from the centroid of the girder

c_g = Distance from the girder neutral axis to the bottom of the girder

c = Distance from the composite neutral axis to the bottom of the girder

M_{sw} = Moment at crack location due to girder self-weight

M_{xt} = Moment caused by decompression load at crack

A = Total cross sectional area of girder and deck concrete

I_g = Moment of inertia of the girder

I = Moment of inertia of the composite section

σ_{ps} = Effective stress of prestressing strands

A_{ps} = Total area of prestressing strands

Table 2 Prestressing values for each girder

Girder #	σ residual (MPa/ksi)	P residual (kN/kip)	Initial Value (kN/kip)	% losses
1	421/61	814/183	1330/299	39%
2	414/60	801/180	1330/299	40%
7	510/74	988/222	1330/299	26%
8	462/67	894/201	1330/299	33%

Capacity Testing

Flexural and shear capacity tests were performed after all the cracking moment tests were completed. While all girders were suitable for the cracking test, a couple one had received some end damage when the girders were removed from the bridge in the field. This girder was used for the flexural capacity test so any damage did not influence the results. Table 1 shows which girder was used for which test(s).

Flexural Capacity Test

Girder 8 was selected for the midspan flexural test. In addition to the strain gauges attached at the midspan from the cracking test, an extra set of strain gauges with the same configuration was also attached at a distance of one third of the span length from one end of the girder. All the strain gauges were only attached on one side of the girder. Furthermore, string potentiometers (String pot) were attached to both sides of the girder at the strain gauges instrumentation location in addition to the center of the supports. The string pots at the supports were to measure the deformation of the elastomeric pad during testing such that the actual girder deflections were obtained by subtracting the pad deformation from the deflection readings.

In order to increase the reliability of the test results and reduce measurement errors, accurate calibration on the sensors were performed prior to testing. All sensors were initialized to zero before the testing initiated. The string pots and load cells were also initially calibrated in order to provide accurate results. The calibration of the load cell was obtained by applying a small load on it and monitoring the output from the Vishay to confirm that the calibration was correct. The calibration of the string pots were performed by lifting the string by a predetermined amount and comparing it with the Vishay output to ensure both values were equivalent.

The applied load for girders was increased monotonically throughout testing until failure. During loading process, the first crack appeared at the bottom flange directly beneath the location of the load. As the loading process continued, additional cracks appeared with a larger angle and propagate out along the bottom flange. The ultimate load was obtained when the concrete in the deck fail in compression. Figure 14 shows the loading and cracking that appeared during the testing.



Figure 14 Cracking during midspan flexural test

Cracking initiated at the bottom flange directly under the applied load at a magnitude of 311 kN (70 kip). As the load increased additional cracks were propagated for approximately 1.5 m (5 ft) on each side of the girder at the load location. The maximum applied load that the girder supported was 578 kN (130 kips), which corresponds to a moment of 1554 kN-m (1146 kip-ft) as shown in Figure 16. After reaching the maximum load capacity, the concrete in the compression block initially started spalling. The load decreased by 89 kN (20 kip) and the deflection kept increasing. The applied load stabilized momentarily at which point the girder reached the ultimate failure. The girder failed suddenly due to the concrete crushing. The top mild steel also buckled. Figure 15 shows the final midspan condition state of the girder at failure. At the third point, where the second set of strain gauges was located, there was minimal cracking that occurred.



Figure 15 Ultimate failure for midspan flexural test

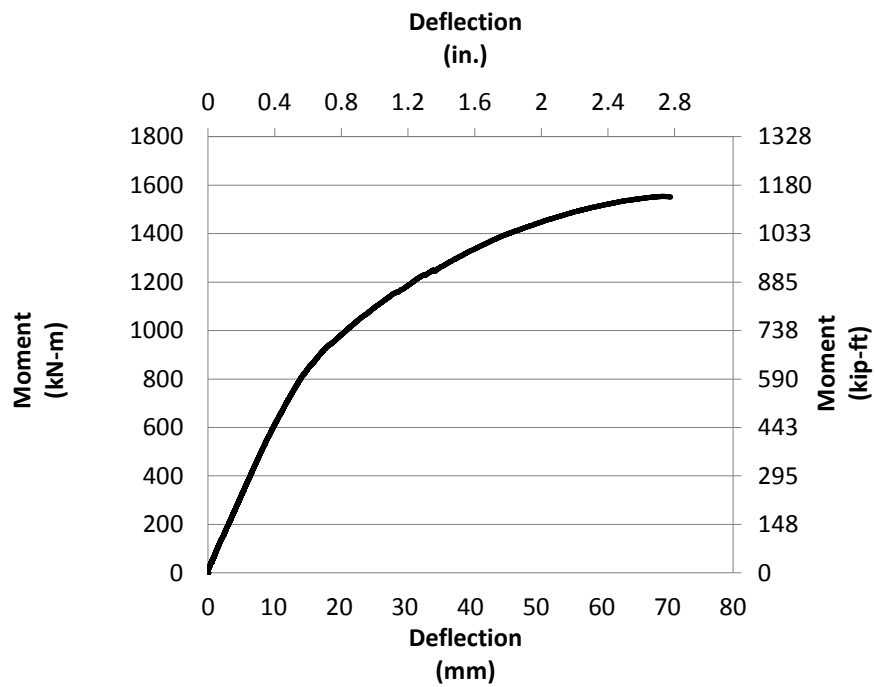


Figure 16 Moment vs. Deflection for midspan flexural test

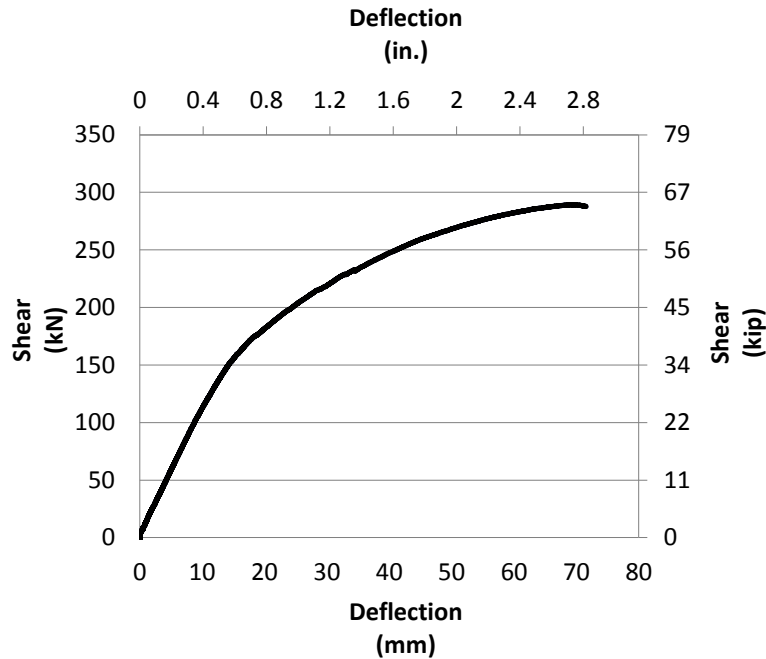


Figure 17 Shear vs. Deflection for midspan flexural test

The shear force was symmetrically equal about the mid-span since the girder was loaded with a single load at mid-span. The maximum shear capacity at the mid-span during the mid-span flexural test was 289 kN (65 kips). The shear development at the mid-span during testing is shown in Figure 17, where the skew in the plot shows the non-linear behavior of the girder directly at the location of loading.

The longitudinal strain distributions along the section at the midspan and at the third distance under different increments of loading are also shown in Figure 18 and Figure 19, respectively. The plane section remained plane until the concrete failed. The plot in Figure 18 shows that the strain at the web started to largely expand because the web started to crush. The neutral axis of the section, where the strain was zero, was also shifting up while loading after cracking. Similarly, Figure 19 shows that the plane section at the third position of the girder also remained plane throughout loading until failure.

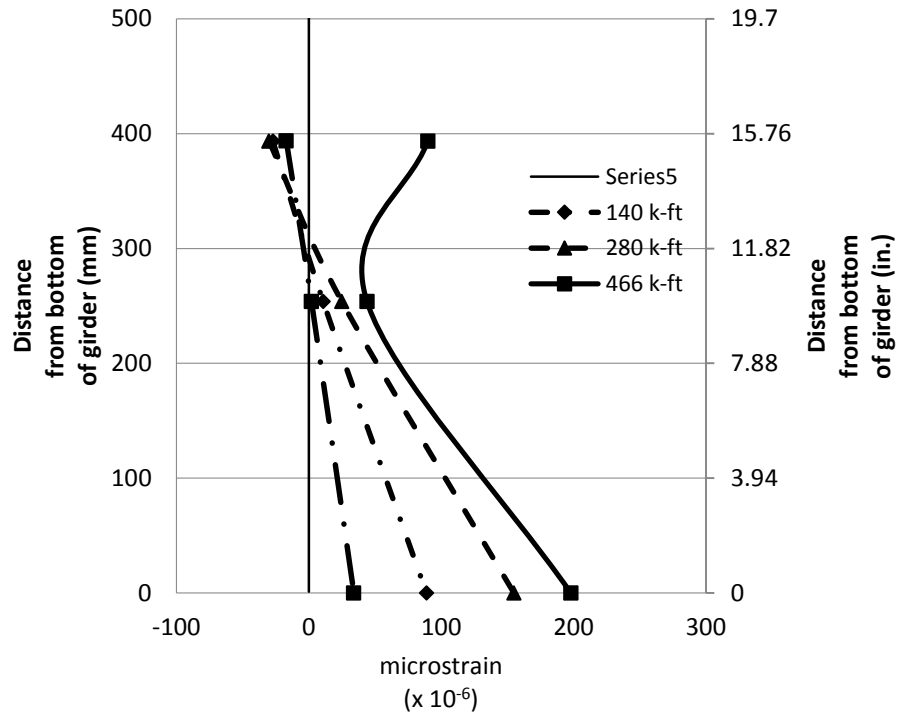


Figure 18 Longitudinal strain distribution at the midspan

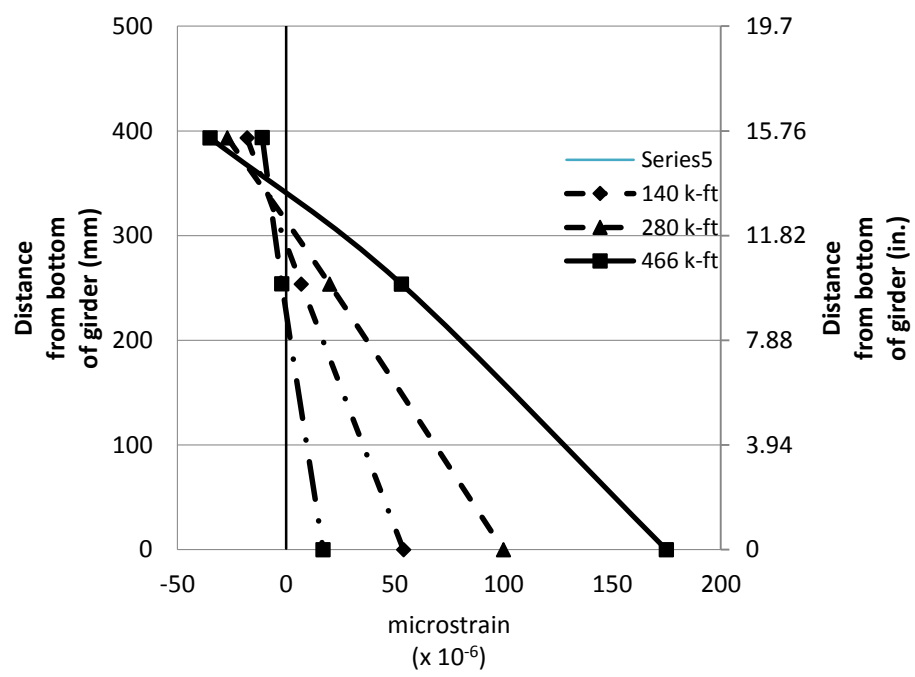


Figure 19 Longitudinal strain distribution at the third span

1-d Test

Due to the brittle nature of shear failures, shear capacity tests were performed at distance of $1-d$, $2-d$, and $4-d$, where d represents the total depth from the girder bottom to the top of the deck concrete. Each testing location performed twice in order to increase the reliability of the results. Girder #2 was used for both of the $1-d$ tests. These tests were named G2-1d(a) and G2-1d(b). The loading was performed by monotonically applying the load from the ram at the first end until failure. The supports were then repositioned and the load was applied at the non-tested end. For this testing, the load was applied at a distance of d , 0.914 m (3 ft) from the center of the support with a span length of 10.9 m (35.25 ft) for G2-1d(a) and 9.0 m (29.64 ft) for G2-1d(b). The change in span length for the second test was adjusted to minimize the effect of one test on another. The ram and load cell positioning for the shear tests were the same as the mid-span flexural test as shown in Figure 20.



Figure 20 Set up for 1-d tests

Shear vs. deflection plots from the $1-d$ tests are shown in Figure 21 and Figure 22. The plot shows that the girder remained nearly elastically until the magnitude of shear reached

approximately 600 kN (135 kip). At this point, visible cracks were observed within the loaded region. The girder stiffness was reduced after cracking, which corresponds to the reduced slope in the plots. In comparison to the flexural test, the cracking does not significantly reduce the stiffness after cracking. The small change in stiffness is believed to be due to the relatively small crack widths that were observed throughout testing. For G2-1d(a), the maximum shear was recorded as 1428 kN (321 kip), where the maximum shear for G2-1d(b) was 1485 kN (334 kip). The average maximum shear capacity was 1457 kN (328 kip), which is the highest recorded shear among all the shear capacity tests in this study.

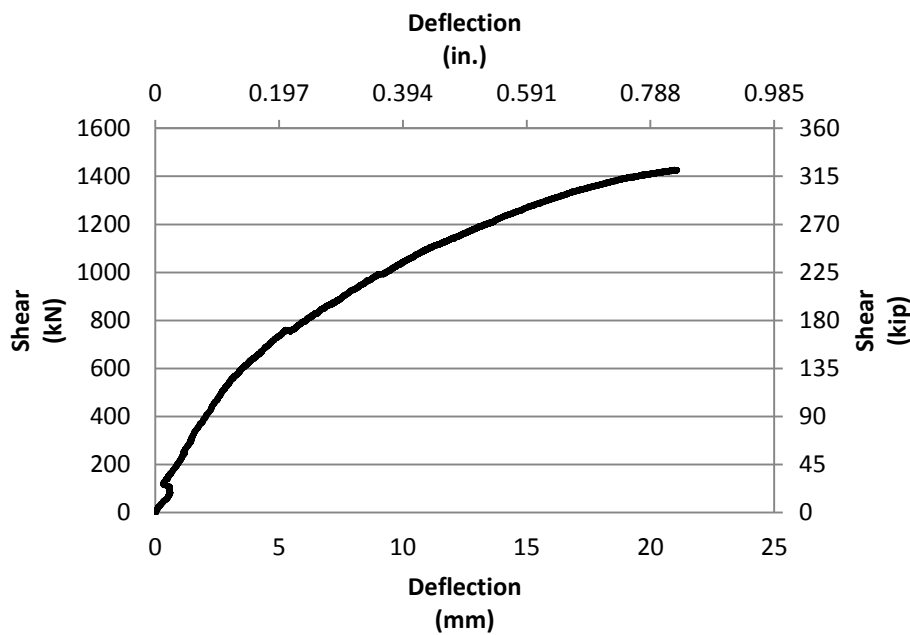


Figure 21 Shear vs. Deflection plot for G2-1d(a)

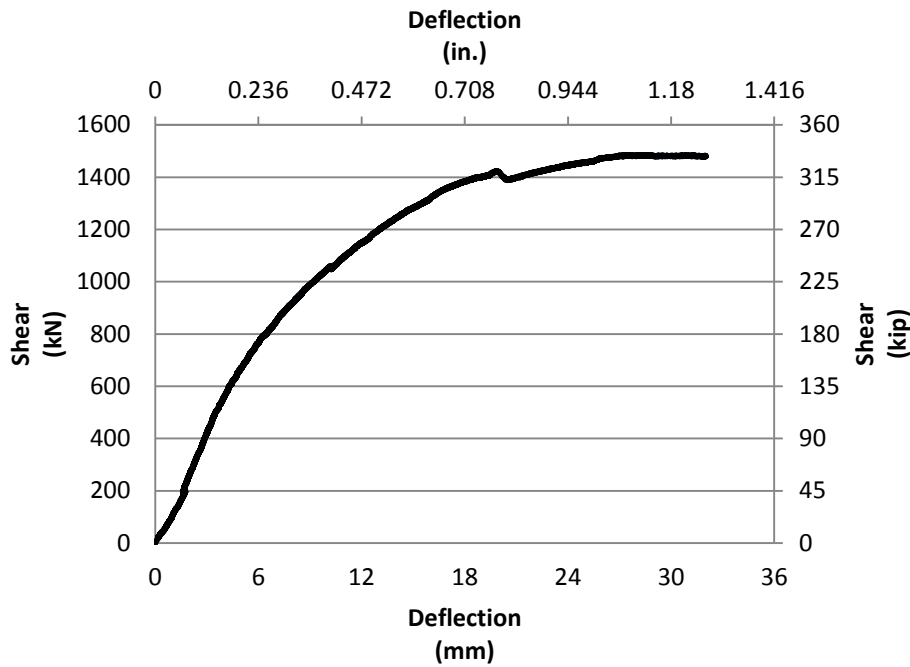


Figure 22 Shear vs. Deflection plot for G2-1d(b)

Moment vs. deflection relationship for the 1-*d* tests was also plotted in Figure 23 and Figure 24. The maximum moment for G2-1d(a) was recorded to be 1305 kN-m (963 kip-ft), whereas the maximum moment for G2-1d(b) was 1358 kN-m (1002 kip-ft). The average maximum moment was 1332 kN-m (983 kip-ft).

The crack propagation at failure is shown in Figure 25. The cracks were relatively minor in comparison to the flexural test. Furthermore, at the end of the girder, diagonal cracks appeared in the web at an approximate 45 degree angle during loading as shown in Figure 26. However, once the crack propagated to the built up end, they were not very visible presumably due to the increased width of the web. The diagonal cracks represent that the girder was under a pure shear failure near the support. The in-angle behavior of the cracks can be explained by the theory of Mohr's Circle. The pure shear failure plane of any element loaded with principal stresses (pure

axial plane stresses with no plane shear) always appears in a 45 degree angle. The concrete element near the end of the girder was under pure axial load on each plane (Principal plane stress) with nearly no plane shear because insufficient bending moments were acting on the girder nearby the support. As the load increased vertical cracks developed. These cracks continued to widen whereas the shear crack widths remained relatively constant. At the ultimate failure, the concrete compression block crushed as shown in Figure 27. Despite the proximity to the end, the 1-*d* tested girder failed under a combined shear and flexural stress due to the presence of the large end block.

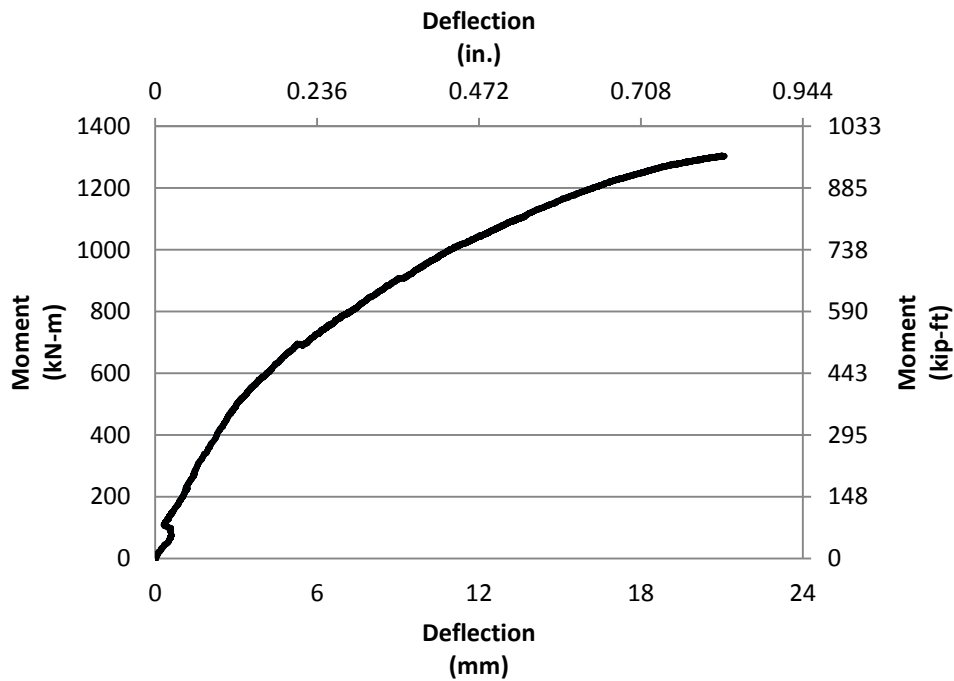


Figure 23 Moment vs. Deflection plot for G2-1d(a)

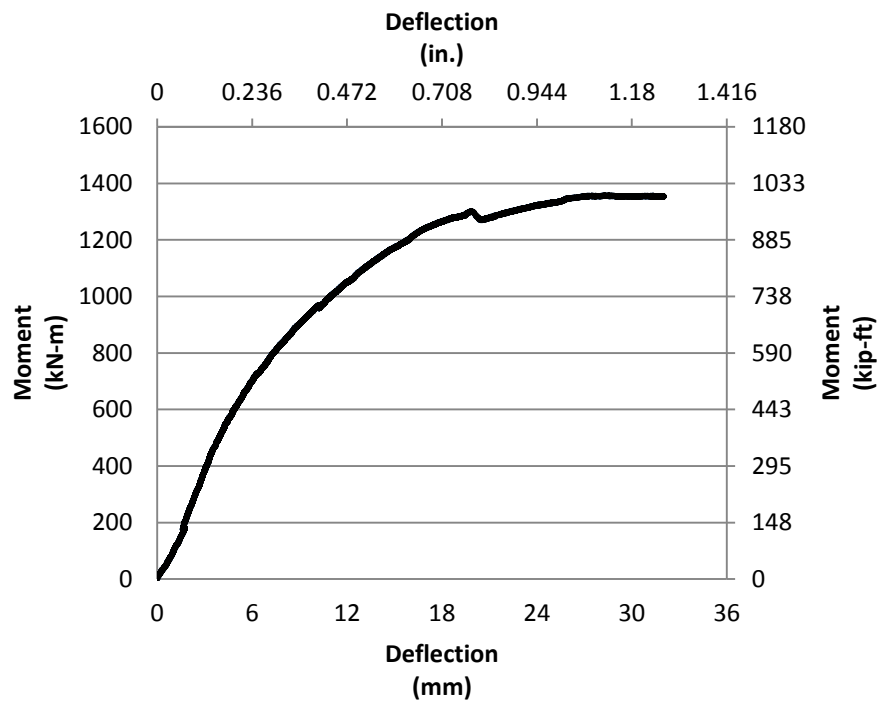


Figure 24 Moment vs. Deflection plot for G2-1d(b)



Figure 25 Cracks under the loading location prior to ultimate failure

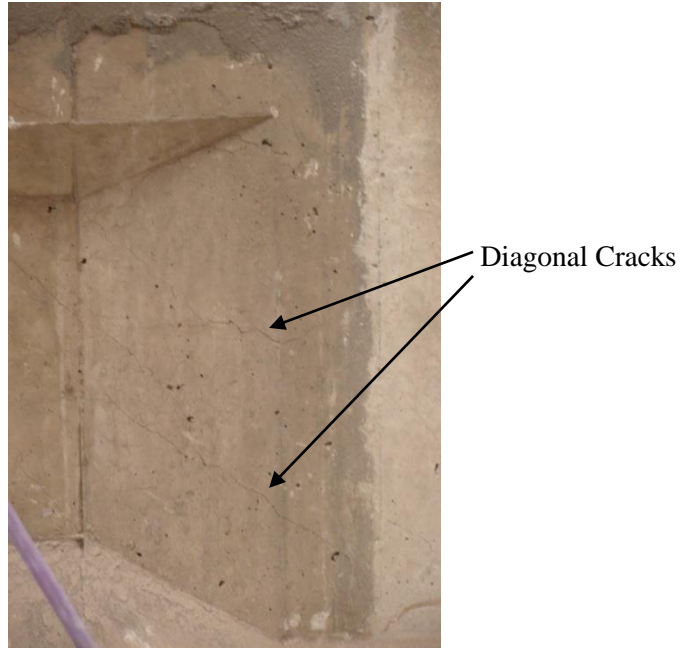


Figure 26 Diagonal cracks near the support



Figure 27 Compressive failure for G2-1d(a)

2-d & 4-d Test

The two remaining shear capacity tests were at the location of 2-*d* and 4-*d* from the supports. These tests were performed similarly as the 1-*d* test. The 2-*d* test was performed by applying a monotonic load on the girder at a distance of 1.83 m (6 ft) from the center of the

support and a distance of 3.66 m (12 ft) for 4-*d* test. Girder #1 and #7 were utilized to perform these two tests. Each test was performed on a girder. Girder #1 was used to perform the 2-*d* test (G1-2d(a)) first on one end, then the 4-*d* test (G1-4d(b)) was performed with a shorter span length of 7.85 m (25.75 ft) on the other end. The 4-*d* test (G7-4d(a)) was first performed on Girder #7 with the full span length. Then the 2-*d* test (G7-2d(b)) was performed on the shorter span length of 6.32 m (20.75 ft). The alternating loading for the testing was performed to minimize the effect from one test to the other.



Figure 28 Cracks and crushes prior to failure

For the 2-*d* tests, the failure occurred when the deck crushed. At failure, the cracks at the bottom flange were wider and propagated at a larger angle in comparison to the 1-*d* tests. Figure 28 shows the cracks and the crushed compression block at the deck and girder for G1-2d(a). For this

test, the girders also exhibited shear characteristics as shown in Figure 29. The shear cracks were approximately at an angle of 45 degree underneath the load.

Figure 30 and Figure 31 show the moment vs. deflection relationship in G1-2d(a) and G7-2d(b), respectively. The slope started to decrease when the moment reached approximately 600 kN-m (442 kip-ft). At this magnitude, the girder cracking initiated such that the effective cross section area was reduced. For G1-2d(a), the maximum load was 970 kN (218 kip) corresponding to the maximum moment of 1472 kN-m (1086 kip-ft). For G7-2d(b), the maximum load was 1060 kN (238 kip) corresponding to the maximum moment of 1379 kN-m (1017 kip-ft). The difference in capacity can be partially attributed to the difference in the effective span lengths, Girder #7 had a higher load capacity than Girder #1. The average maximum moment was 1426 kN-m (1052 kip-ft).

The shear vs. deflection relationship for G1-2d(a) and G7-2d(b) is shown in Figure 32 and Figure 33. The maximum shear was recorded as 805 kN (181 kip) and 754 kN (169 kip), respectively for both 2-*d* tests with an average value of 780 kN (175 kip).



Figure 29 Shear failure in G1-2d(a)

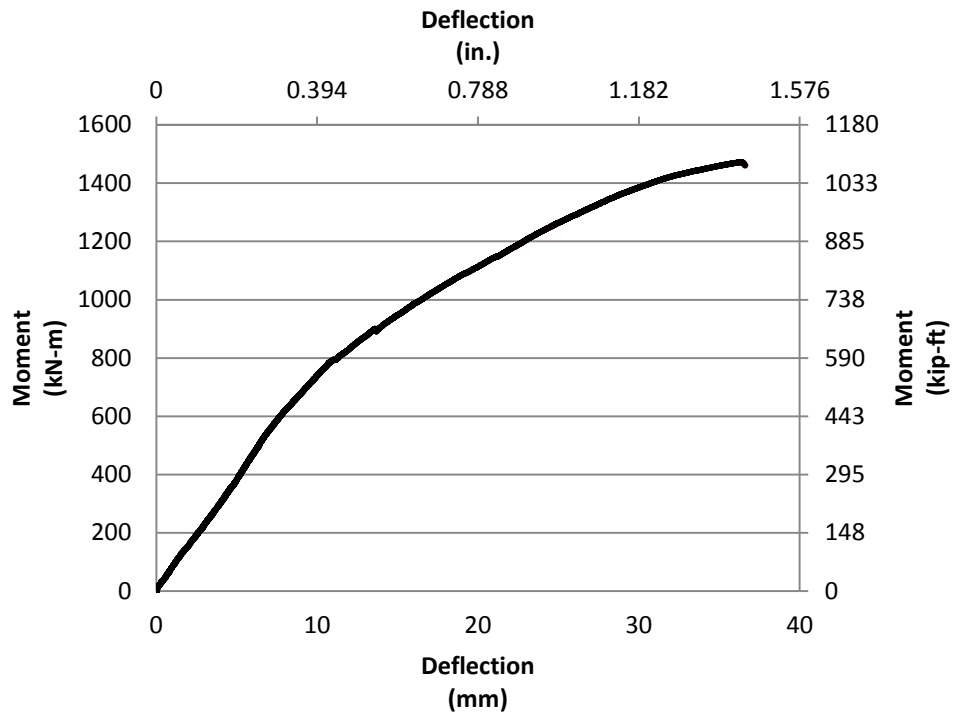


Figure 30 Moment vs. Deflection plot for G1-2d(a)

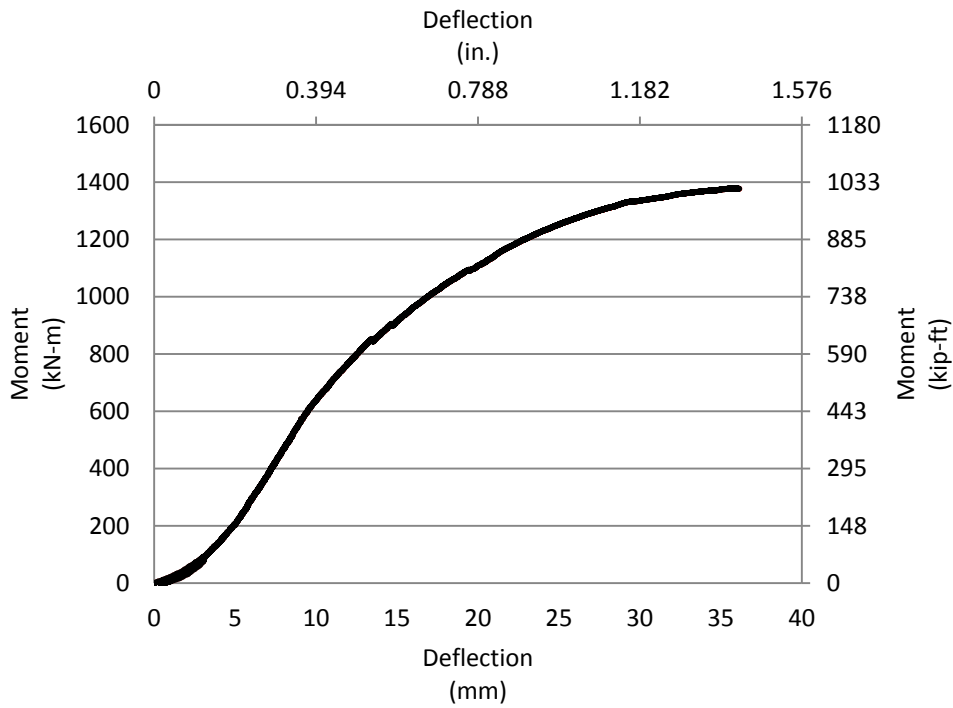


Figure 31 Moment vs. Deflection plot for G7-2d(b)

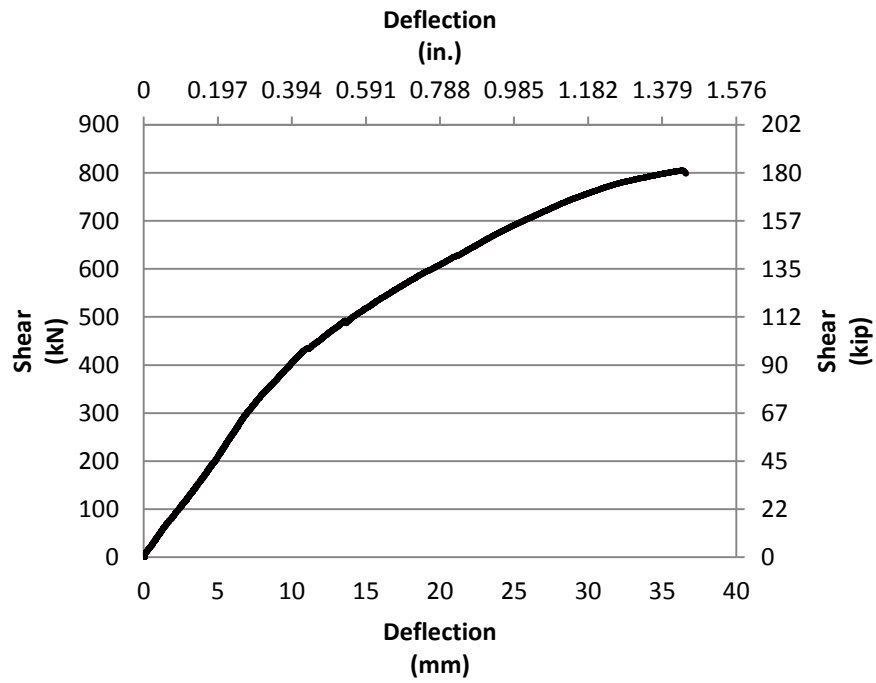


Figure 32 Shear vs. Deflection plot for G1-2d(a)

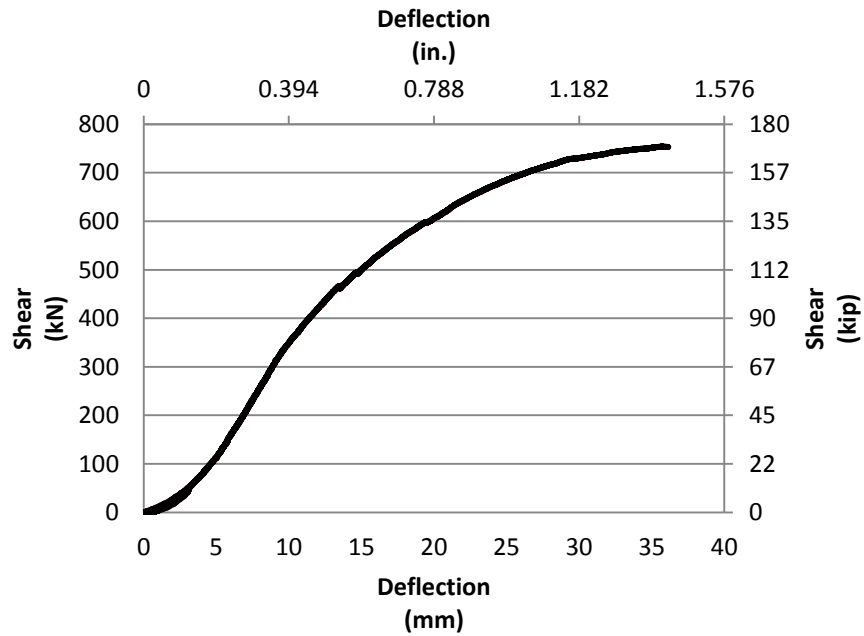


Figure 33 Shear vs. Deflection plot for G7-2d(b)

For the 4-*d* tests, failure occurred in a predominately flexure manner. Figure 34 shows that the concrete deck and the top of the girder were crushed near the loading point. Predominately vertical cracks developed with a few diagonal cracks from the load. The girder failure behavior in the 4-*d* test was similar to the 1-*d* test, except that there were no diagonal cracks appeared during the 4-*d* test. Hence, it is believed that the girder failed in a predominately flexural condition.



Figure 34 Compressive failure in G7-4d(a)

For the plots shown in Figure 35, Figure 36, Figure 37, and Figure 38, the maximum moment for G7-4d(a) and G1-4d(b) is shown as 1531 kN-m (1129 kip-ft) and 1397 kN-m (1031 kip-ft), respectively. This moment is associated with the maximum applied load of 634 kN (143 kip) and 715 kN (161 kip), respectively. It is believed that the load capacity of the girder for the second test was higher than the first one because of the change in span lengths between tests. The average maximum moment was 1464 kN-m (1080 kip-ft). The cracking moment was approximately 700 kN-m (516 kip-ft) where the stiffness of the girder was reduced afterward. The maximum shear was 418 kN (94 kip) and 382 kN (86 kip), respectively, with an average magnitude of 400 kN (90 kip).

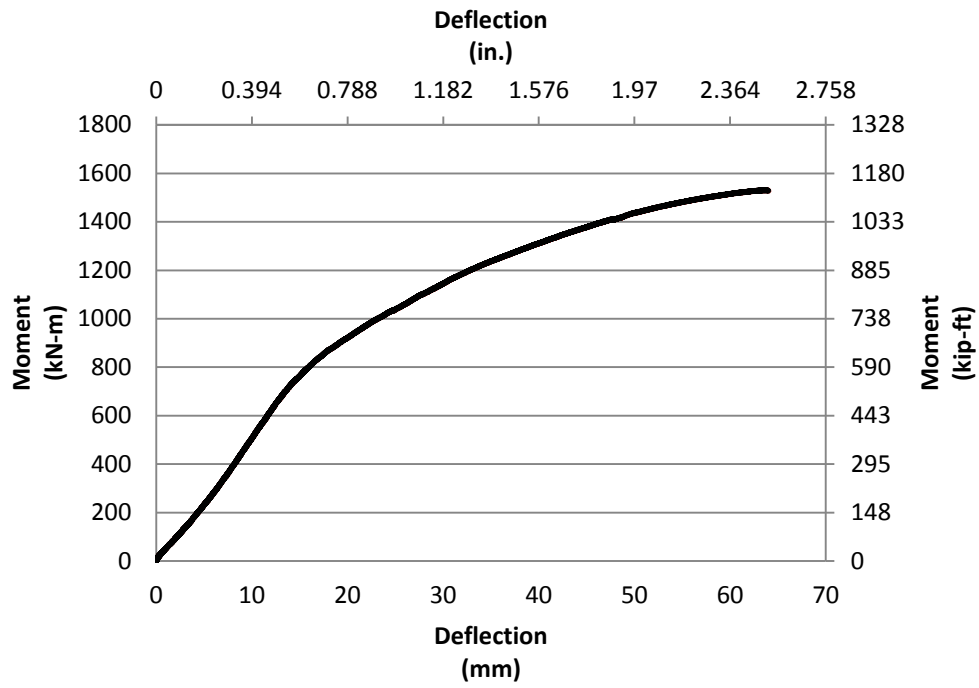


Figure 35 Moment vs. Deflection plot for G7-4d(a)

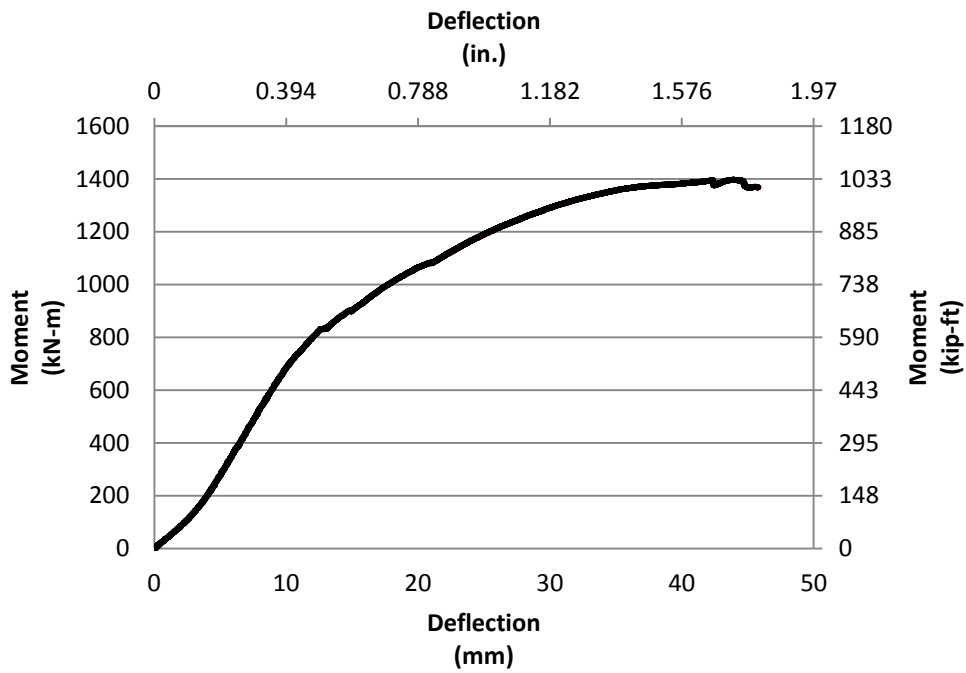


Figure 36 Moment vs. Deflection plot for G1-4d(b)

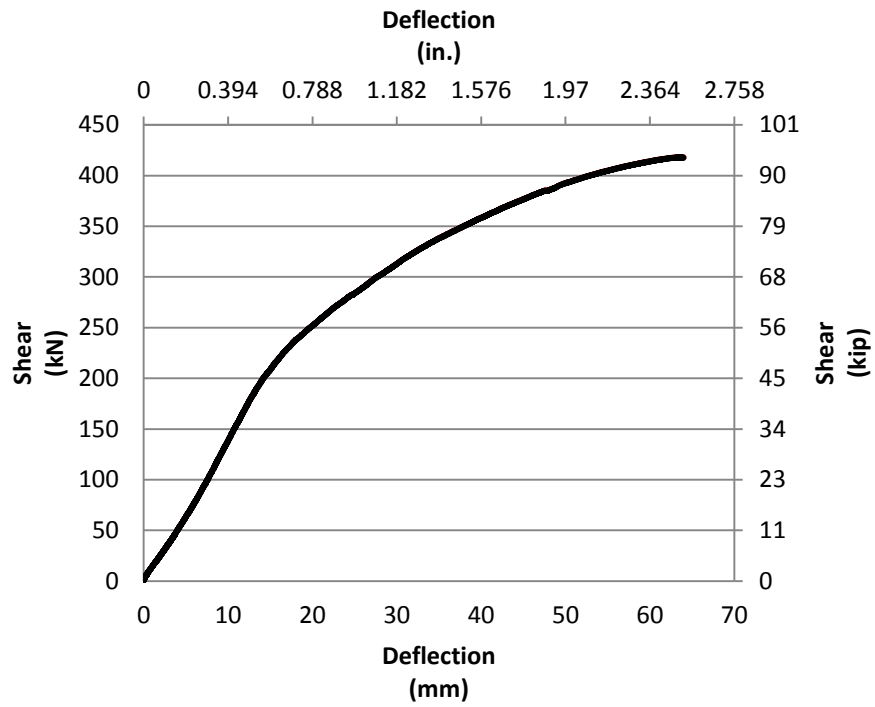


Figure 37 Shear vs. Deflection plot for G7-4d(a)

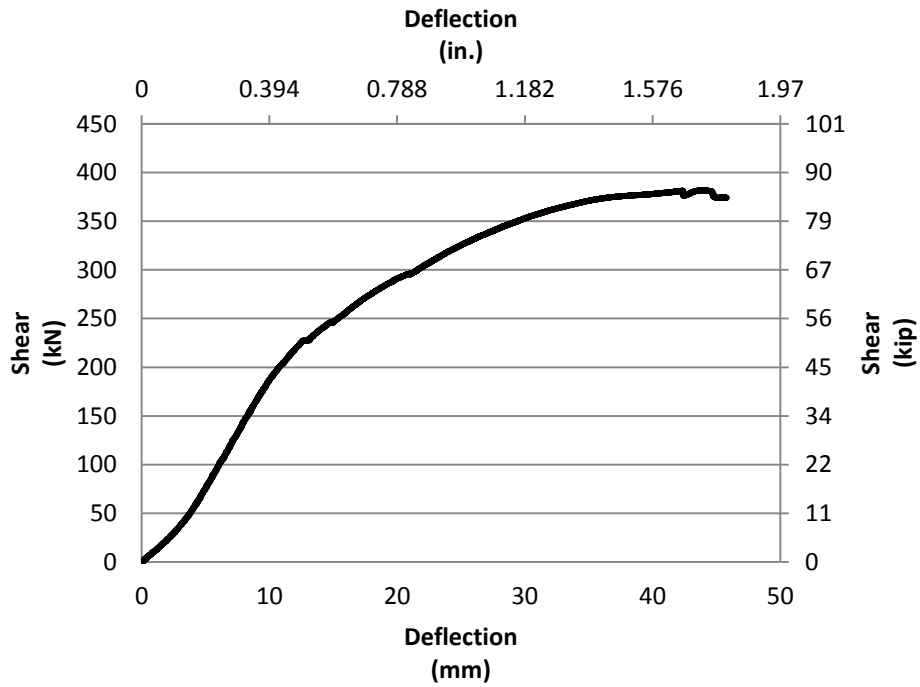


Figure 38 Shear vs. Deflection plot for G1-4d(b)

Summary of the experimental results

The overall result of moment and shear capacities for each test is tabulated in Table 3 and also plotted in Figure 39 and Figure 40. Through the comparison of different tests, it clearly shows that the shear capacity in the 1-*d* test was the highest among all the tests. The applied load was positioned closest to the support out of all other tests, which implies that the shear load was more predominant with respect to the failure condition of the girder. However, the observation from the 1-*d* test shows that the girder primarily failed in flexural through the concrete crushing at the top. The possible reason why the failure of the girder was not in a shear failure manner is because the box end section of the girder near the loading point actually enhanced the strength of the girder. But the vast shear load still affected the girder by having some small diagonal cracks at the box end section as shown in Figure 26 above. The box end section increases the compressive strength of the girder during post-tensioning as well as the shear capacity when the load is near the ends.

Table 3 Overall results for all tests

Test	Moment kN-m (kip-ft)	Shear kN (kip)
G2-1d(a)	1305 (963)	1428 (321)
G2-1d(b)	1358 (1002)	1485 (334)
Average 1d	1332 (982)	1456 (327)
G1-2d(a)	1472 (1086)	805 (181)
G7-2d(b)	1379 (1017)	754 (169)
Average 2d	1425 (1051)	780 (175)
G7-4d(a)	1531 (1129)	418 (94)
G1-4d(b)	1397 (1031)	382 (86)
Average 4d	1464 (1080)	400 (90)
Mid-Span	1554 (1146)	289 (65)

For the 2-*d* test, the shear capacity is the second highest in this study. The failure was in a flexural-shear manner as expected due to the high-shear load. For this test, the box end section did not influence the shear capacity since the load was further away from the girder end in comparison to the 1-*d* test. As the loading was placed further away from the support, the flexural loading effect becomes more significant, in other word, the shear effect becomes less significant. The 4-*d* tests and mid-span had the largest flexural influence as expected with a relatively minor shear load effect. Figure 39 shows the decreasing trend of the shear capacity with respect to the distance between the load and near support, αL .

In addition, the moment capacities for all tests were relatively closed. The average maximum moment among all tests is 1444 kN-m (1065 kip-ft) with a standard deviation of 6%, which means the moment capacities for all tests are not really varied in comparison to the shear capacities. However, there is still a mild increasing trend of moment capacity along with αL , as shown in Figure 40. However, the moment capacities along the entire girder are still fairly consistent.

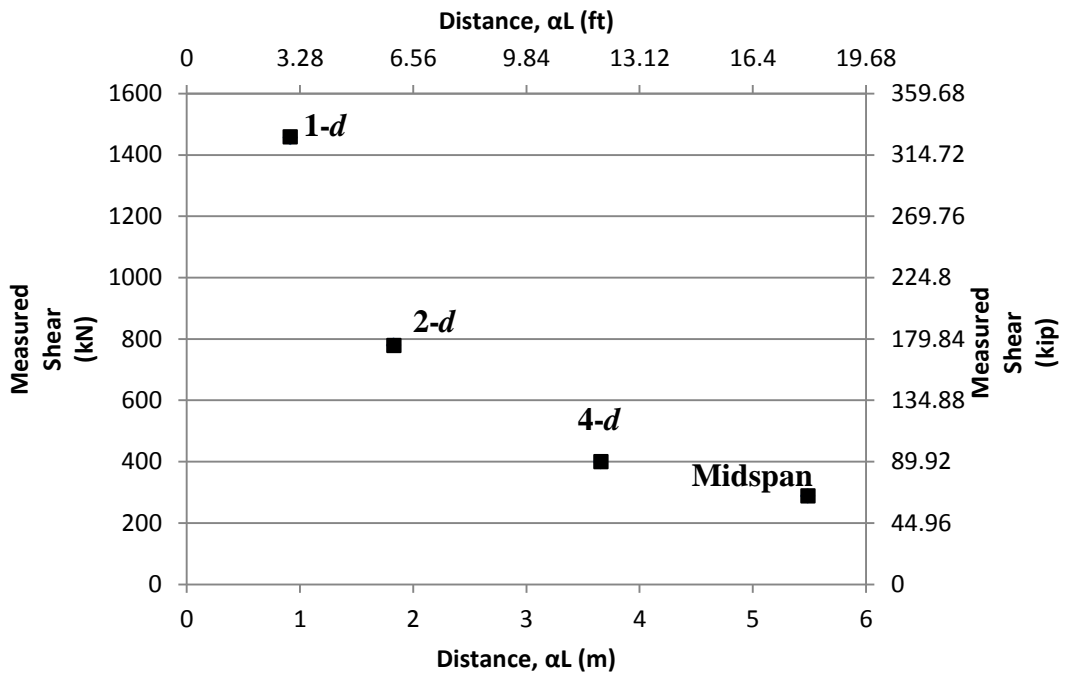


Figure 39 Overall shear results vs. distance, αL

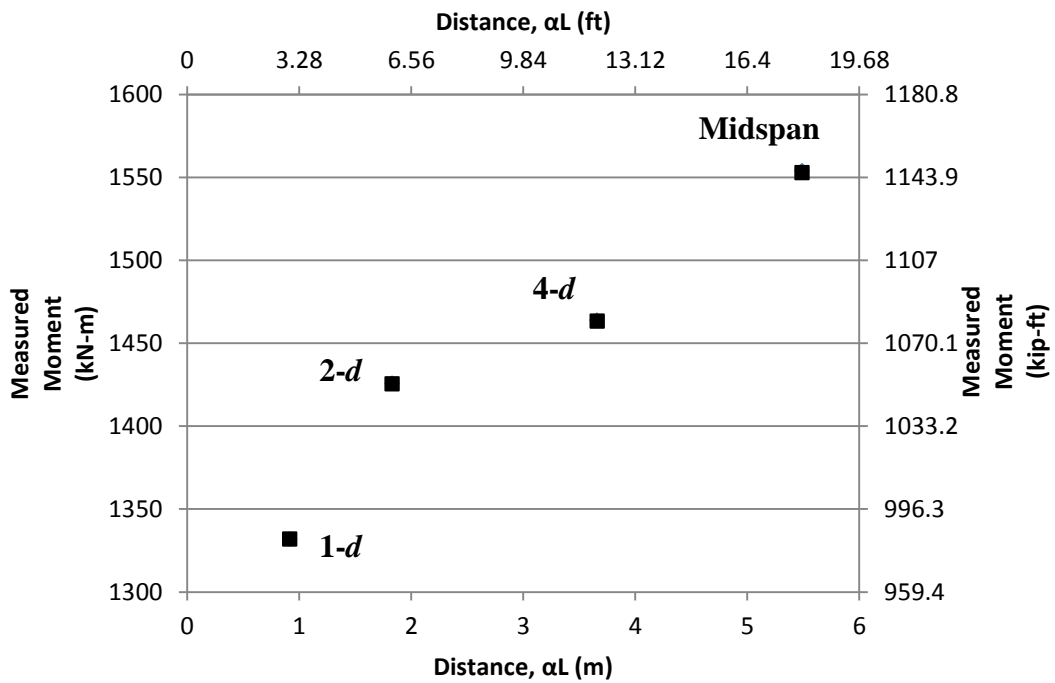


Figure 40 Overall moment results vs. distance, αL

Chapter 5

COMPARISON OF TESTED RESULTS TO AASHTO LRFD DESIGN AND ANSYS

The AASHTO LRFD Specifications 2012 (AASHTO 2012) is the current code for bridge girder design. The experimental results, which consisted of prestressing losses in addition to nominal moment and shear capacities, were compared with the predicted results using the procedures specified in the AASHTO specifications. Since the girders for this study were designed 50 years ago, the comparison will be how current codes predict existing girder behavior. In this chapter, the experimental results were also further compared with a finite-element model using ANSYS.

Prestressing losses

The measured prestress losses for each girder were determined based on the results from the cracking moment tests. The theoretical losses were then calculated following recommended procedure in the AASHTO LRFD specification for further comparison. The recommended methods to calculate the prestressing losses for pretensioned/post-tensioned concrete bridge girders are specified in the Section 5.9.5 of the AASHTO 2012 manual, which includes both a simplified and refined method. Both methods were applied in this research for comparison. According to AASHTO 2012, the total prestress losses are theoretically divided into two different loss categories, instantaneous and time-dependent losses. The instantaneous losses are caused by anchorage set (Δf_{pA}), friction (Δf_{pF}), and elastic shortening (Δf_{pES}), whereas the time-dependent losses (Δf_{pLT}) are due to creep, shrinkage, and relaxation.

Simplified Method

The total prestress losses (Δf_{pT}), according to the simplified method, for a post-tensioned concrete girder are calculated using Eq. 3, which is the sum of the various components of losses mentioned previously in this section.

$$\Delta f_{pT} = \Delta f_{pF} + \Delta f_{pA} + \Delta f_{pES} + \Delta f_{pLT}$$

Eq. 3

The approach to estimate the instantaneous losses is the same for both the simplified and refined method. The friction losses are caused by the friction developed between the internal post-tensioned tendons and the duct wall, which is defined as Eq. 4. The loss due to anchorage set is caused by the axial movement of the tendon prior to seating of the wedges or the anchorage gripping device. The recommended value of movement, δ , for bar tendons is 1.59 mm (0.0625 in.) as recommended in Section C5.9.5.2.1 in AASHTO 2012. The anchorage loss then is calculated based on Hooke's Law using Eq. 5. The loss due to elastic shortening occurs at the time of girder tensioning. For post-tensioned members, the short-term loss due to elastic shortening can generally be minimized by retensioning the post-tensioning strand or bar during construction. The elastic shortening losses in post-tensioned members can be determined by Eq. 6.

$$\Delta f_{pF} = f_{pj}(1 - e^{-(Kx + \mu\alpha)})$$

Eq. 4

$$\Delta f_{pA} = E_p \frac{\delta}{L}$$

Eq. 5

$$\Delta f_{pES} = \frac{N - 1}{2N} \frac{A_{ps} f_{pbt} (I_g + e_m^2 A_g) - e_m M_g A_g}{A_{ps} (I_g + e_m^2 A_g) - \frac{A_g I_g E_{ci}}{E_p}}$$

Eq. 6

where

- f_{pj} = stress in the prestressing steel at jacking (99.7 ksi)
- x = length of a prestressing tendon from the jacking end to any point under consideration (18.125 ft)
- K = wobble friction coefficient (0.0002)
- μ = coefficient of friction (0.3)
- α = sum of the absolute values of angular change of prestressing steel path from jacking end, or from the nearest jacking end if tensioning is done equally at both ends, to the point under investigation (0.1102)
- δ = axial deformation in prestressing tendons prior to seating (0.0625 in.)
- L = length of the tendon (435 in.)
- A_{ps} = area of prestressing steel (2.98 in.²)
- A_g = gross area of girder cross-section (276 in.²)
- E_{ci} = modulus of elasticity of concrete at transfer (4070 ksi)
- E_p = modulus of elasticity of prestressing tendons (29000 ksi)
- e_m = average eccentricity at midspan (8.34 in.)
- f_{pbt} = stress in prestressing steel immediately prior to transfer (99.7 ksi)
- I_g = moment of inertia of the gross concrete section (28500 in.⁴)
- M_g = midspan moment due to member self-weight (46.1 kip-ft)
- N = number of identical prestressing tendons (3.0)

The calculation of time-dependent losses is divided calculated differently depending on the method. The simplified method utilizes Eq. 7 in which correction factors for relative humidity, γ_h , and for concrete strength, γ_{st} , are provided in Eq. 8 and Eq. 9, respectively. The refined method will be discussed in the next section. The simplified method provides a relatively conservative approach to estimate the time-dependent losses in a prestressed or post-tensioned girder.

$$\Delta f_{pLT} = 10.0 \frac{f_{pi} A_{ps}}{A_g} \gamma_h \gamma_{st} + 12.0 \gamma_h \gamma_{st} + \Delta f_{pR} \quad \text{Eq. 7}$$

$$\gamma_h = 1.7 - 0.01H \quad \text{Eq. 8}$$

$$\gamma_{st} = \frac{5}{(1 + f'_{ci})} \quad \text{Eq. 9}$$

where

f_{pi} = prestressing steel stress immediately prior to transfer (99.7 ksi)

H = average annual ambient relative humidity (%) (53.7)

γ_h = correction factor for relative humidity of the ambient air (1.163)

γ_{st} = correction factor for specified concrete strength at time of prestress transfer to the concrete member (0.8333)

Δf_{pR} = an estimate of relaxation loss (3.34)

f'_{ci} = compressive strength of concrete at transfer (5 ksi)

The prestress force at jacking is specified as 62.3 kN (14 kip) per strands in the bridge plan with twenty-four prestressed strands resulting a total prestress force of 1495 kN (336 kip) at jacking. As mentioned, the actual prestressing force for the girder was provided using three parabolic post-tensioned steel rods. The equivalent prestress force was calculated based on the actual configuration of the prestressing resulting an equivalent initial prestress of 687.4 MPa (99.7 ksi) for each of the post-tensioned rods. The effective prestress was then determined by subtracting all of the losses from the initial prestress at jacking. Table 4 shows the prestress losses for all components and the total loss as well as the effective prestress after losses. The calculated prestress loss from the Simplified Method in AASHTO 2012 is 40.4%.

Table 4 Prestress losses using Simplified Method

Prestress losses using Simplified Method	
Δf_{pF}	24.8 MPa (3.59 ksi)
Δf_{pA}	28.8 MPa (4.17 ksi)
Δf_{pES}	26.0 MPa (3.77 ksi)
Δf_{pLT}	198.6 MPa (28.8 ksi)
Δf_{pT}	277.9 MPa (40.3 ksi)
f_{pe}	409.5 MPa (59.4 ksi)

Refined method

The refined method provides a more detail approach to estimate the time-dependent losses, which is intended to provide a more precise value in comparison to using the simplified method. The calculation of instantaneous losses is identical for both methods. The estimation of time-dependent losses with the refined method is defined as Eq. 10 below. This method

considers separate two periods of long-term losses. They are the time between transfer and deck placement, and between deck placement and final time, which correspond to the subscripts *id* and *df*, respectively, in the equation.

$$\Delta f_{pLT} = (\Delta f_{pSR} + \Delta f_{pCR} + \Delta f_{pR1})_{id} + (\Delta f_{pSD} + \Delta f_{pCD} + \Delta f_{pR2} - \Delta f_{pSS})_{df}$$

Eq. 10

where

Δf_{pSR} = prestress loss due to shrinkage of girder concrete between transfer and deck placement

Δf_{pCR} = prestress loss due to creep of girder concrete between transfer and deck placement

Δf_{pR1} = prestress loss due to relaxation of post-tensioning bars between time of transfer and deck placement

Δf_{pR2} = prestress loss due to relaxation of post-tensioning bars in composite section between time of deck placement and final time

Δf_{pSD} = prestress loss due to shrinkage of girder concrete between time of deck placement and final time

Δf_{pCD} = prestress loss due to creep of girder concrete between time of deck placement and final time

Δf_{pSS} = prestress gain due to shrinkage of deck in composite section

The significance of dividing two periods of losses is based on the difference of section properties at these two periods. Eq. 11, Eq. 12, and Eq. 13 are used to calculate the long-term prestress losses between transfer and deck placement with the girder-only properties, where Eq.

14, Eq. 15, Eq. 16 and Eq. 17 calculate that between deck placement and final time with the composite section properties.

$$\Delta f_{pSR} = \varepsilon_{bid} E_p K_{id} \quad \text{Eq. 11}$$

$$\Delta f_{pCR} = \frac{E_p}{E_{ci}} f_{cgp} \psi_b(t_f, t_i) K_{id} \quad \text{Eq. 12}$$

$$\Delta f_{pR1} = \frac{f_{pt}}{K_L} \left(\frac{f_{pt}}{f_{py}} - 0.55 \right) \quad \text{Eq. 13}$$

$$\Delta f_{pSD} = \varepsilon_{bdf} E_p K_{df} \quad \text{Eq. 14}$$

$$\Delta f_{pCD} = \frac{E_p}{E_{ci}} f_{cgp} \psi_b[(t_f, t_i) - \psi_b(t_d, t_i)] K_{df} + \frac{E_p}{E_c} \Delta f_{cdf} \psi_b(t_f, t_d) K_{df} \quad \text{Eq. 15}$$

$$\Delta f_{pR2} = \Delta f_{pR1} \quad \text{Eq. 16}$$

$$\Delta f_{pSS} = \frac{E_p}{E_c} \Delta f_{cdf} K_{df} [1 + 0.7 \psi_b(t_f, t_d)] \quad \text{Eq. 17}$$

$$K_{id} = \frac{1}{1 + \frac{E_p}{E_{ci}} \frac{A_{ps}}{A_g} \left(1 + \frac{A_g e_{pg}^2}{I_g} \right) [1 + 0.7 \psi_b(t_f, t_i)]} \quad \text{Eq. 18}$$

$$\varepsilon_{bdf} = k_s k_{hs} k_f k_{td} 0.48 \times 10^{-3} \quad \text{Eq. 19}$$

$$\Delta f_{cd} = \frac{\Delta P}{A_g} + \frac{\Delta P e_{pg}^2}{I_g} + \frac{M_g e_{pg}}{I_g}$$

Eq. 20

$$\Delta P = (\Delta f_{pEs} + \Delta f_{pSR} + \Delta f_{pCR} + \Delta f_{pR1}) A_{ps}$$

Eq. 21

$$K_{df} = \frac{1}{1 + \frac{E_p A_{ps}}{E_{ci} A_g} \left(1 + \frac{A_c e_{pc}^2}{I_c}\right) [1 + 0.7\psi_b(t_f, t_i)]}$$

Eq. 22

$$\Delta f_{cdf} = \frac{\varepsilon_{ddf} A_d E_{cd}}{[1 + 0.7\psi_b(t_f, t_d)]} \left(\frac{1}{A_c} - \frac{e_{pc} e_d}{I_c}\right)$$

Eq. 23

$$\psi_b(t, t_i) = 1.9 k_s k_{hc} k_f k_{td} t_i^{-0.118}$$

Eq. 24

$$k_s = 1.45 - 0.13(V/S) \geq 1.0$$

Eq. 25

$$k_{hc} = 1.56 - 0.008H$$

Eq. 26

$$k_f = \frac{5}{1 + f'_{ci}}$$

Eq. 27

$$k_{td} = \frac{t}{61 - 4f'_{ci} + t}$$

Eq. 28

where

ε_{bid} = concrete shrinkage strain of girder between the time of transfer and deck placement (0.0002)

- K_{id} = transformed section coefficient that accounts for time-dependent interaction between concrete and bonded steel in the section being considered for time period between transfer and deck placement (0.8507)
- e_{pg} = eccentricity of prestressing force with respect to centroid of girder: positive in common construction where it is below girder centroid (8.34 in.)
- f_{cgp} = concrete stresses at the prestressing centroid due to the prestressing force after jacking and self-weight of the member at the sections of maximum moment (1.65 ksi)
- $\Psi_b(t_f, t_i)$ = girder creep coefficient at final time due to loading introduced at transfer
- t_f = final age (18587 days)
- t_i = age at transfer (28 days)
- t_d = age at deck placement (56 days)
- f_{pt} = stress in prestressing tendons immediately after transfer, taken not less than $0.55f_{py}$ (107.5 ksi)
- K_L = 30 for low relaxation strands and 7 for other prestressing steel (7.0)
- ϵ_{bdf} = shrinkage strain of girder between time of deck placement and final time (0.00022)
- K_{df} = transformed section coefficient that accounts for time-dependent interaction between concrete and bonded steel in the section being considered for time period between deck placement and final time (0.858)
- e_{pc} = eccentricity of prestressing force with respect to centroid of composite section, positive in typical construction where prestressing force is below centroid of section (12.6 in.)
- A_c = area of section calculated using the gross composite concrete section properties of

the girder and the deck and the deck-to-girder modular ratio (372 in.²)

I_c = moment of inertia of section calculated using the gross composite concrete section properties of the girder and the deck and the deck-to-girder modular ratio at service (65218 in.⁴)

Δf_{cd} = change in concrete stress at centroid of prestressing tendons due to long-term losses between transfer and deck placement, combined with deck weight and superimposed loads (0.4 ksi)

Δf_{cdf} = change in concrete stress at centroid of prestressing tendons due to shrinkage of deck concrete (0.9 ksi)

ΔP = change in prestressing force prior to deck placement (58.6 kip)

E_c = modulus of elasticity of concrete at 28 days strength (4070 ksi)

E_{cd} = modulus of elasticity of deck concrete (3640 ksi)

A_d = area of deck concrete (504 in.²)

e_d = eccentricity of deck with respect to the gross composite section, positive in typical construction where deck is above girder (7.04 in.)

H = relative humidity (%). In the absence of better information, H may be taken from Figure 5.4.2.3.3-1 in AASHTO 2012 (53.7)

k_s = factor for the effect of the volume-to-surface ratio of the component (1.054)

k_f = factor for the effect of concrete strength (0.833)

k_{hc} = humidity factor for creep (1.13)

k_{td} = time development factor (0.406)

t = maturity of concrete (day), defined as age of concrete between time of loading for creep calculations, or end of curing for shrinkage calculations, and time being

considered for analysis of creep or shrinkage effects

V = volume of girder (120060 in.³)

S = surface area of girder (39420 in.²)

All of the components of the time-dependent losses from the Refined Method are listed in Table 5, where the total time-dependent loss is shown as 125.5 MPa (18.2 ksi). The total time-dependent loss was then added to the instantaneous losses, which was the same as the value calculated from the Simplified Method, and subtracted from the prestress at jacking [687.4 MPa (99.7 ksi)] to determine the effective prestress on each post-tensioned rod. The prestress loss calculated with Refined Method was determined to be 29.8%.

Table 5 Time-dependent losses from Refined Method

Time-dependent losses from Refined Method	
Δf_{pSR}	+36.3 MPa (+5.27 ksi)
Δf_{pCR}	+35.6 MPa (+5.17 ksi)
Δf_{pRI}	+23.0 MPa (+3.34 ksi)
Δf_{pSD}	+37.8 MPa (+5.48 ksi)
Δf_{pCD}	+10.5 MPa (+1.53 ksi)
Δf_{pR2}	+23.0 MPa (+3.34 ksi)
Δf_{pSS}	-53.8 MPa (-7.80 ksi)
Δf_{pLT}	125.5 MPa (18.2 ksi)

Table 6 Prestress losses using Refined Method

Prestress losses using Refined Method	
Δf_{pF}	24.8 MPa (3.59 ksi)
Δf_{pA}	29.1 MPa (4.17 ksi)
Δf_{pES}	26.7 MPa (3.77 ksi)
Δf_{pLT}	114.6 MPa (18.2 ksi)
Δf_{pT}	195.2 MPa (29.7 ksi)
f_{pe}	492.4 MPa (70.0 ksi)

Comparison between AASHTO and Cracking Moment tests for Effective prestress

The average effective prestress based on the cracking moment tests was 457.1 MPa (65.5 ksi). Table 7 shows a comparison between the average measured results and the values from AASHTO both methods. The effective prestress calculated with AASHTO Simplified method overestimated the prestress losses. The effective stress is 9.31% lower than the tested average, which reflects that the simplified method in AASHTO is considered as the more conservative method as expected. However, the AASHTO Refined Method predicts the calculated effective prestress of 482.7 MPa (70.0 ksi), which corresponds to a difference of 6.87% higher than the tested average. The Refined Method in the AASHTO LRFD specifications underestimated the prestress losses as expected because this method is preferred to be a more precise and less conservative approach.

Table 7 Comparison on Effective prestress with different methods

Method	Calculated Effective Prestress	% difference from tested average
Cracking Moment tests	457.1 MPa (65.5 ksi)	N/A
AASHTO Simplified Method	409.5 MPa (59.4 ksi)	-9.31 %
AASHTO Refined Method	482.7 MPa (70.0 ksi)	6.87%

Moment Capacity

The measured moment capacities for each girder were compared to the calculated value in accordance to procedures from the AASHTO specification (2012) as well as the finite-element model using ANSYS. Section 5.7.3.2 in AASHTO 2012 describes the method of calculating flexural resistance with a prestressed concrete structure. The nominal flexural capacity (M_n) is

calculated using Eq. 29. The resistance factor (ϕ) specified in AASHTO 2012 was neglected in this comparison because this reduction factor is generally used in design situation. Therefore, the nominal flexural capacity according to the procedures in AASHTO (2012) was directly compared with the test results.

$$M_n = A_{ps}f_{ps} \left(d_p - \frac{a}{2} \right) + A_s f_s \left(d_s - \frac{a}{2} \right) - A'_s f'_s \left(d'_s - \frac{a}{2} \right) + 0.85 f'_c (b - b_w) h_f \left(\frac{a}{2} - \frac{h_f}{2} \right)$$

Eq. 29

In which,

$$a = c\beta_1$$

Eq. 30

$$\beta_1 = 0.85 - 0.05(f'_c - 4), \text{ where } 0.65 \leq \beta_1 \leq 0.85 \text{ for all } f'_c$$

Eq. 31

where

A_{ps} = total cross-sectional area of prestressing steel (2.98 in²)

f_{ps} = specified tensile strength of prestressing steel (147 ksi for 1-*d* test, 149 ksi for 2-*d* test, 150 ksi for 4-*d* and flexural tests)

d_p = distance from top of compression block to the centroid of prestressing tendons directly under the load (25.9 in. for 1-*d* test, 28.3 in. for 2-*d* test, 31.0 in. for 4-*d* test, and 31.8 in. for flexural test)

A_s = total cross-sectional area of mild tension reinforcement (0.5 in²)

f_s = stress in the mild steel tension reinforcement (60 ksi)

d_s = distance from top of compression block to the centroid of mild tensile reinforcement (26 in.)

- A'_s = total cross-sectional area of mild compression reinforcement (2 in²)
- f'_s = stress in the mild steel compression reinforcement (60 ksi)
- d'_s = distance from top of compression block to the centroid of mild compression reinforcement (4 in.)
- f'_c = 28-day compressive strength of deck concrete (6.7 ksi)
- b = effective width of the compression face of the member (12 in.)
- b_w = web width of the member (12 in. for 1- d test, 6 in. for other tests)
- h_f = compression flange depth (8 in.)
- a = depth of the equivalent compressive stress block (5.11 in. for 1- d test, 5.17 in. for 2- d test, 5.22 in. for 4- d test, and 5.24 in. for flexural test)
- c = Distance from top of compression block to the neutral axis (7.15 in. for 1- d test, 7.23 in. for 2- d test, 7.30 in. for 4- d test, and 7.32 in. for flexural test)
- β_1 = stress block factor (0.715)

The nominal flexural capacity was determined by taking the moment about the top of the cross section and then combining the resultant moment produced from all structural components in the girder, which are prestressing steel, mild tension reinforcement, mild compression reinforcement, and the concrete in compression. The location of neutral axis (c) for the study was determined by Eq. 32. The constant, k , is specified in AASHTO and is dependent on the yield strength (f_{py}) and ultimate strength (f_{pu}) of the prestressing steel. The k is defined by Eq. 33 or Table 8. The post-tensioned bar for the tested girder is identified as Type 1, high-strength bar, which corresponds to a k value of 0.38 according to Table 8. The tensile stress in the post-tensioned bars during testing for moment capacity is defined by Eq. 34 and it is limited by the ultimate strength of the steel.

$$c = \frac{A_{ps}f_{pu} + A_s f_s - A'_s f'_s}{0.85f'_c \beta_1 b + k A_{ps} \frac{f_{pu}}{d_p}}$$

Eq. 32

$$k = 2 \left(1.04 - \frac{f_{py}}{f_{pu}} \right)$$

Eq. 33

$$f_{ps} = f_{pu} \left(1 - k \frac{c}{d_p} \right) \leq f_{pu}$$

Eq. 34

Table 8 *k* value for different types of tendon

Type of Tendon	f_{py}/f_{pu}	<i>k</i>
Low relaxation strand	0.90	0.28
Stress-relieved strand and Type 1 high-strength bar	0.85	0.38
Type 2 high-strength bar	0.8	0.48

The detail comparison of moment capacity between the experimental results and calculated AASHTO values is listed in Table 9 below. The prediction AASHTO capacity was conservative for the moment capacity by approximate of 5.5% in comparison to all tested results, which shows that the flexural failure predominantly controlled for each test.

Table 9 Comparison of the theoretical moment capacity to measured value for each test

Test	Moment Capacity kN-m (kip-ft)		
	Experimental	AASHTO 2012	% diff. from AASHTO
1- <i>d</i>	1331 (982)	1221 (900)	9.1%
2- <i>d</i>	1425 (1051)	1302 (960)	9.4%
4- <i>d</i>	1464 (1080)	1451 (1070)	0.9%
Midspan	1554 (1146)	1492 (1100)	4.2%

Shear Capacity

The experimental result of all tested girders for shear capacity was compared with the AASHTO (2012) predictive methods and the finite-element model results. AASHTO (2012) specifies two methods for calculating the shear capacity of prestressed girders. The two methods are the simplified procedure and a strut-and-tie model. Both of these methods were used in this research.

Shear Capacity using AASHTO Simplified Procedure for Prestressed Concrete Girders

The simplified procedure to calculate the nominal shear resistance (V_n) of prestressed concrete girders is specified in Section 5.8.3.4.3 of AASHTO 2012. The shear resistance is comprised of three portions of shear resistance, which are the resistances provided by the stirrup (V_s), the vertical prestressing force (V_p) and the concrete from two cracking conditions. The two cracking conditions are combined flexural and shear cracks (V_{ci}) and excessive tensile forces in the web (V_{cw}). The lesser of the two concrete shear resistances is used in Eq. 35 to calculate the total nominal shear capacity. Each component of the nominal shear resistance is determined with Eq 36 through 38

$$V_n = \min \left\{ \begin{matrix} V_{ci} \\ V_{cw} \end{matrix} \right\} + V_p + V_s$$

Eq. 35

$$V_{ci} = 0.02 \sqrt{f'_{cg}} b_v d_v + V_d + \frac{V_i M_{cre}}{M_{max}}$$

Eq. 36

$$V_{cw} = \left(0.06 \sqrt{f'_{cg}} + 0.30 f_{pc} \right) b_v d_v + V_p$$

Eq. 37

$$V_s = \frac{A_v f_y d_v (\cot \theta + \cot \alpha) \sin \alpha}{s}$$

Eq. 38

In which

$$d_v = \min \left\{ \begin{array}{l} d_e - \frac{a}{2} \\ 0.9d_e \\ 0.72h \end{array} \right\}$$

Eq. 39

$$V_d = \frac{w_d}{2} (l - x)$$

Eq. 40

$$M_{cre} = S_c \left(f_r + f_{cpe} - \frac{M_{dnc}}{S_{nc}} \right)$$

Eq. 41

$$f_{cpe} = \frac{P_e}{A_g} + \frac{P_e c_2 c_g}{I_g}$$

Eq. 42

$$S_c = \frac{I_c}{c_c}$$

Eq. 43

$$f_r = 0.2 \sqrt{f'_{cg}}$$

Eq. 44

$$M_{dnc} = \frac{w_d x}{2} (l - x)$$

Eq. 45

$$S_{nc} = \frac{I_g}{c_g}$$

Eq. 46

$$f_{pc} = \frac{P_e}{A_g} - \frac{P_e c_2 (c_c - c_g)}{I_g} + \frac{M_{dnc} (c_c - c_g)}{I_g}$$

Eq. 47

$$\cot \theta = \begin{cases} 1.0 + 3 \left(\frac{f_{pc}}{\sqrt{f'_{cg}}} \right) \leq 1.8, & V_{ci} > V_{cw} \\ 1.0, & V_{ci} < V_{cw} \end{cases}$$

Eq. 48

where

V_{ci} = nominal shear resistance provided by concrete when inclined cracking results from combined shear and moment (kip)

V_{cw} = nominal shear resistance provided by concrete when inclined cracking results from excessive principal tensions in web (kip)

V_s = nominal shear resistance provided by mild reinforcement (kip)

f'_{cg} = compressive strength of the girder concrete (7.5 ksi)

b_v = minimum web width within the depth, d_v (6 in.)

d_v = effective shear depth (25.9 in. for 1- d test, 28.3 in. for 2- d test, 31.0 in. for 4- d test, and 31.8 in. for flexural test)

d_e = distance from the extreme compressive face to the centroid of prestressing (25.9 in. for 1- d test, 28.3 in. for 2- d test, 31.0 in. for 4- d test, and 31.8 in. for flexural test)

a = depth of Whitney stress block (25.9 in. for 1- d test, 28.3 in. for 2- d test, 31.0 in. for 4- d test, and 31.8 in. for flexural test)

h = total depth of the girder (36 in.)

V_d = shear force at distance x along the girder due to dead load (kip)

- V_i = shear force at distance x along the girder due to externally applied loads (kip)
- M_{cre} = cracking moment (25.9 in. for 1- d test, 28.3 in. for 2- d test, 31.0 in. for 4- d test, and 31.8 in. for flexural test)
- M_{max} = maximum moment along the girder due to externally applied loads (kip-ft)
- S_c = section modulus of the composite section (2780 in.³)
- S_{nc} = section modulus of the non-composite section (1807 in.³)
- I_c = moment of inertia of composite section (47739 in.⁴)
- I_g = moment of inertia of non-composite section (22750 in.⁴)
- c_c = distance from the bottom of the girder to the composite neutral axis (17.17 in.)
- c_g = distance from the bottom of the girder to the non-composite neutral axis (12.59 in.)
- f_{cpe} = compressive stress in concrete due to effective prestress forces (ksi)
- M_{dnc} = moment due to dead load acting on the non-composite section (kip-ft)
- f_r = modulus of rupture of concrete (0.58 ksi)
- f_{pc} = compressive stress in concrete after all prestress losses occurred at the composite centroid (ksi)
- P_e = effective prestress force after all prestress losses occurred (199.7 kip)
- c_2 = distance from the centroid of prestressing to the girder neutral axis (in.)
- V_p = vertical component of the effective prestress force (25.9 in. for 1- d test, 28.3 in. for 2- d test, 31.0 in. for 4- d test, and 31.8 in. for flexural test)
- w_d = uniform distributed dead load along the girder (0.387 kip/ft)
- x = distance from the center of near support to the center of applied load (in.)
- l = distance between supports (35.25 ft)
- A_v = area of shear reinforcement within a distance s (in.²)

- s = spacing of transverse reinforcement at a distance x along the girder (in.)
- θ = angle of inclination of diagonal compressive stress (deg)
- α = angle of inclination of transverse reinforcement to longitudinal axis (90°)

The calculated shear components in Eq. 35 are shown in Table 10 below. The midspan test was surely dominated by flexural failure so that the shear capacity comparison is unnecessary for the midspan test. As shown in Table 10 V_{cw} governs among the two kinds of shear resistance due to the concrete in 1- d and 2- d tests, the $\cot(\theta)$ for these two tests was then calculated by Eq. 48. The smaller value of x results in the shear resistance due to the stirrup controlling. It is because the stirrup was distributed with closer spacing near the supports, which reflects that the shear force is majorly significant while loading near the supports. The shear resistance due to prestressing was considered in the calculation of V_{cw} and it occupied approximately 13% of V_{cw} in average of all test results. However, V_{ci} governs in the 4- d test giving that the $\cot(\theta)$ equals to one as shown in Eq. 48, which subsequently obtained a lesser predominant value of V_s than the results from the 1- d and 2- d tests.

Table 10 Components in shear capacity for each shear test

Test	x mm (in.)	V_{ci} kN (kip)	V_{cw} kN (kip)	V_s kN (kip)	V_p kN (kip)
1- d	914 (36)	590 (133)	517 (116)	1428 (321)	65.7 (14.8)
2- d	1829 (72)	332 (75)	284 (64)	753 (169)	49.3 (11.1)
4- d	3658 (144)	200 (45)	251 (56)	231 (52)	25.0 (5.62)

Table 11 provides the comparison of the calculated shear capacity to the average measured shear value for each shear tests. The percentage difference between the theoretical and measured shear values on 1- d and 2- d tests is more than 30%. This discrepancy indicates that the

AASHTO simplified procedure provided an overly conservative value of the shear capacity when the load was applied at a distance of $1-d$ and $2-d$ from the support for the tested girders. The box end section of the girders significantly increase the shear capacity near the supports such that the girders predominantly failed in a flexural manner, where the maximum measured shear did not really represent the actual shear capacity. In addition for the $1-d$ test, a more accurate value of shear capacity was also determined with a strut-and-tie model and will be discussed in the next section. However, the AASHTO simplified procedure obtained a relatively accurate estimation of shear capacity for the $4-d$ test with a percent difference of only 13.8%. This indicates that the box end section did not significantly affect the result when the load was far away from the supports.

Table 11 Comparison of theoretical shear capacities to measured for each shear test

Test	V_n kN (kip)	V_i kN (kip)	% Difference
$1-d$	2020 (454)	1456 (327)	38.9%
$2-d$	1086 (244)	778 (175)	39.5%
$4-d$	455 (102)	400 (90)	13.8%

AASHTO LRFD Strut-and-tie Model

The strut-and-tie procedure to estimate the shear capacity of prestressed concrete members is specified in Section 5.6.3 of AASHTO (2012). This method is believed to provide a more accurate estimate of shear strength when the distance between the center of the applied load and the center of the support is less than twice of the member thickness (AASHTO 2012). A graphical representation of the strut-and-tie model for this research is shown in Figure 41. Nodes A and C represent the supports while node B represents the bearing plate where the load was applied. The post-tensioned bars were represented by the tie AC, which located at the centroid of

the prestressing. Two types of nodal regions were assigned for each node. Node B was defined as the nodes surrounded by compressive struts and a compressive bearing area (c-c-c) and nodes A and C were defined as the nodes with one direction tension tie anchored in (c-c-t).

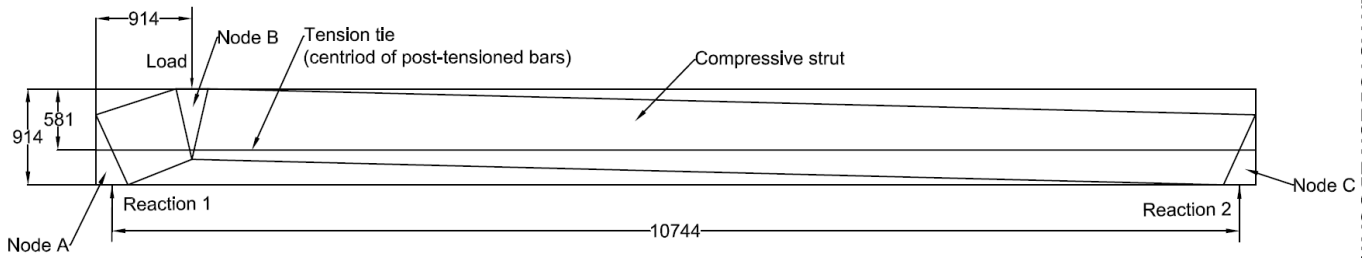


Figure 41 Strut-and-tie model of the girder

This method, with the simple truss model shown in Figure 41, was used for the 1-*d* test in this research to calculate the shear strength since the location of loading satisfied the preference of this method. The shear capacity of the strut-and-tie model was determined using Eq. 49 through Eq. 57. The strength reduction factor was neglected for this research so that the nominal shear capacity was utilized for a direct comparison. The calculated shear capacity using the strut-and-tie model was 1472 kN (331 kip), which obtains a difference of 1.71% in comparison to the measured result of 1456 kN (327 kip). The AASHTO (2012) procedure with a strut-and-tie model was highly accurate on predicting the shear capacity when the location of loading was within a distance of 2-*d* from the center of support, where *d* is the depth of the girder.

$$M_B = f_{ce} h_b t (H - c_p - h_b)$$

Eq. 49

$$f_{ce} = \begin{cases} 0.75f'_c, & (c - c - t) \\ 0.85f'_c, & (c - c - c) \end{cases}$$

Eq. 50

$$\alpha = \tan^{-1} \left(\frac{H - \frac{h_b}{2} - c_p}{x} \right)$$

Eq. 51

$$F_{AB} = \frac{R_A}{\sin \alpha}$$

Eq. 52

$$\varepsilon_1 = \varepsilon_s + (\varepsilon_s + 0.002) \cot \alpha^2$$

Eq. 53

$$f_{cu} = \frac{f'_c}{0.8 + 170\varepsilon_s}$$

Eq. 54

$$P_n = f_{cu} A_{cs}$$

Eq. 55

$$A_{cs} = (l_b \sin \alpha + h_a \cos \alpha) t$$

Eq. 56

$$V = P_n \sin \alpha$$

Eq. 57

where

M_B = moment due to applied load at node B (11700 kip-ft)

f_{ce} = limiting concrete compressive stress for each nodal region type (ksi)

f'_c = compressive strength of concrete at each node (ksi), deck strength at node B and girder strength at node A and C (6.7 ksi for deck strength, and 7.5 ksi for girder strength)

h_b = depth of nodal influence, solved from Eq. 49 (9.43 in.)

t = thickness of the girder (12 in.)

- H = total depth of the girder (36 in.)
- c_p = distance from bottom of the girder to centroid of the prestressing (13.125 in.)
- α = angle between strut AB to tie AC (26.8°)
- x = distance from center of the support to center of the applied load (36 in.)
- F_{AB} = axial compressive force in strut AB (722 kip)
- R_A = reaction force at node A due to loading at node B
- ε_l = principal tensile strain in cracked concrete due to applied loads (0.0161)
- ε_s = tensile strain in concrete in the direction of tie AC (0.00165)
- f_{cu} = limiting concrete compressive stress (2.12 ksi)
- P_n = nominal concrete compressive force in strut AB (735 kip)
- A_{cs} = effective cross-sectional area of the strut (346 in.²)
- l_b = width of the bearing plate at node A (12 in.)
- h_a = twice of c_p (26.25 in.)
- V = nominal shear capacity of the girder (331 kip)

The AASHTO 2012 Simplified Procedure discussed in previous section overpredicted shear capacity for this research. The box end section of the tested girders significantly increased the shear capacity of the girder near the reaction. It is believed that this is because the girder predominantly failed in flexure, where the measured shear capacity was not representative for the actual shear capacity. However, the strut-and-tie model still provided an accurate prediction on the shear capacity for the 1-*d* test.

Finite Element Modeling

ANSYS Mechanical 13.0 was the finite element modeling software used for this research to demonstrate and analyze the nonlinear behavior of the girders. Finite element modeling is a way to accurately analyze the behavior of a mechanism by discretizing the model into small elements with a finite size, then performing an analysis on each element until all results converge. ANSYS was utilized for this research to replicate the physical testing and provide a computerized analysis on each girder for additional comparison of results.

For this research, an identical finite-element model was used to perform each test, which are the 1-*d*, 2-*d*, 4-*d*, and flexural tests. Each analysis was performed by changing the location of the applied load to the location of the corresponding experiment. ANSYS can be operated by either utilizing the Graphical User Interface (GUI) or by inputting commands. For this research, the entire preprocessing procedure was performed by using the command option, where the post-processing procedure was performed using the GUI. The preprocessing procedure involved an iterative process to create an optimized model. A text file was then created to save all the commands to conveniently iterate the procedure by importing the commands directly from the text file. The command text file is shown in Appendix C.

At the beginning of the preprocessing, 3-D solid volumes were needed to model the prototype of the girder. There are many predefined commands to create volumes. Two ways were used in this research. Volumes were created by connecting “keypoints” or using a predefined command in ANSYS called “BLOCK”. However, the command “BLOCK” is limited to create hexahedral volumes only. Therefore, this command was applied when only creating the prototype of steel plates and the decking. Keypoints were defined with a coordinate in x, y, and z direction and a user defined number for being called out during the entire procedure. At least

four keypoints, at most eight, were needed to create a volume. Keypoints were shared for adjacent volumes. Each volume in the girder prototype was created by connecting keypoints.

Material

Once the volumes were created, they were assigned with a material type, real constant, and element type in ANSYS to demonstrate the actual material behavior. Each material type was defined with a user defined number. Table 12 provides a list of the material number corresponding to each girder component. Each material type was assigned with the material properties such as modulus of elasticity, Poisson’s ratio, and density. All material properties were based on the measured values, however some properties were adjusted to optimize the result to match the actual result from the experiments. Some material properties were also defined in tables or using real constants in ANSYS.

Table 12 Corresponding Material Numbers

Material Number	Material
1	Girder Concrete
2	Steel plate & mild steel
3	Post-tensioned steel
4	Anchorage steel plate
5	Deck Concrete

Table

Tables are used to define certain material properties that are varied under a particular relationship, whether linear or nonlinear. Three types of tables were used in this research, which were CONCR table and BISO table. The CONCR table defined the strength of the concrete while loading. Four constants were assigned in the concrete table, which were the shear transfer coefficients for an open crack and for a closed crack, uniaxial tensile cracking stress, and

uniaxial crushing stress. The shear transfer coefficient is defined as a value between 0 and 1, which represents the percentage of shear transfer based on the condition of the crack face, 0 means smooth face and no shear transfer while a value of 1 means rough face and 100% transfer. The shear transfer coefficients for an open crack and a closed crack were 0.3 and 1, respectively, based on previous research (Dahmani et al. 2010). The uniaxial tensile cracking stress and crushing stress were defined as the tensile strength and the compressive strength of the concrete, respectively.

The BISO table represents a bi-slope table, which means that two slopes of curves can be defined in this table. The nonlinear stress-and-strain relationship of the steel was defined with a BISO table with the steel yielding strength and the secondary modulus of the steel (the slope of the stress-strain curve after yielding). The stress-strain relationship of the post-tensioned steel defined in ANSYS is shown in Figure 42. This curve was idealized from the experimental curve produced by the tensile test.

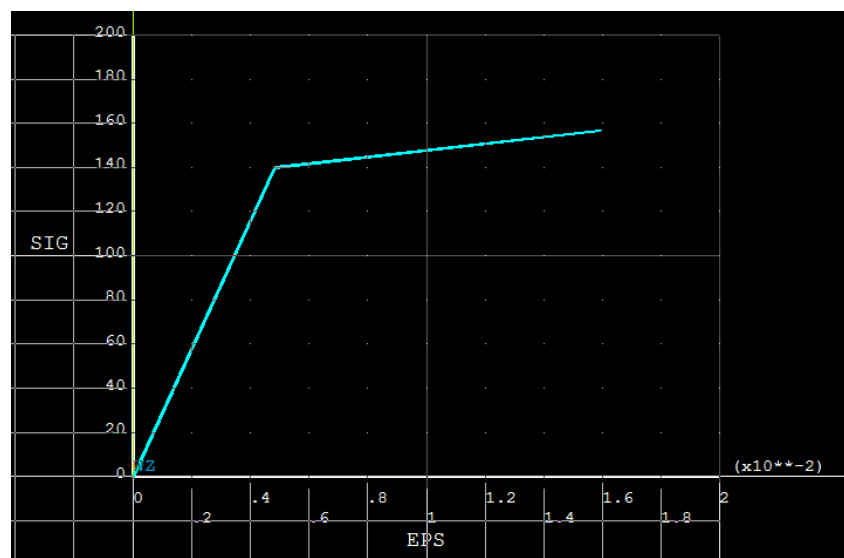


Figure 42 Defined stress-strain curve in ANSYS for the post-tensioned steel

Element Types

ANSYS provides the user a large library of element types to best-fit the specific material behavior. Five types of element were utilized in this research, which were SOLID65, SOLID45, LINK8, TARGE170, and CONTA173. The SOLID65 is a concrete type of element that is capable of modeling a 3-D solid with cracking in tension and crushing in compression, where the reinforcing steel in the concrete can also be modeled. The specification of reinforcing will be discussed in the *Real Constant* section below. The SOLID45 was applied to model the steel components of the model. This type of element replicates the behavior of elastic material such as steel. The element type utilized for the post-tensioned rods was the LINK8 element, which is a 3-D spar element and also a uniaxial compression-tension element. Prestressing is able to be applied to this element, which will be discussed in the *Real Constant* section. TARGE170 and CONTA173 is a pair of elements that was used to model the surface-to-surface contact between the deck and the girder for this research. This pair of element type is also able to connect two surfaces with dissimilar meshing. TARGE170 is usually used on the stiffer surface (girder) and CONTA173 is on the softer surface (deck).

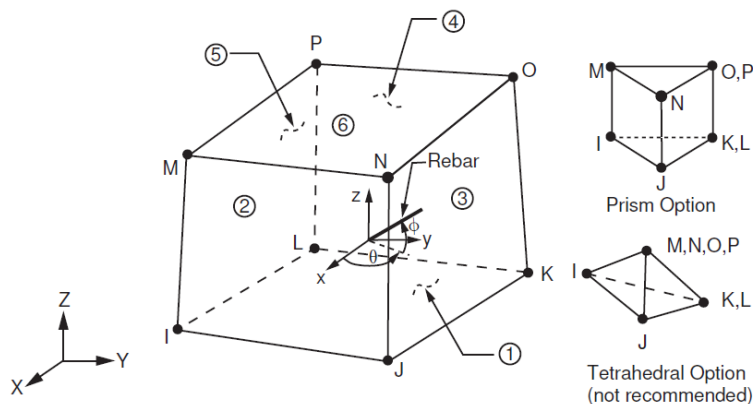


Figure 43 Geometric Shape for SOLID65

Real Constant

The definition of real constants is different depending on the corresponding element type. As mentioned, the reinforcing in the concrete (Solid65) was able to be defined using the real constant command. The reinforcing steel in the concrete was specified using the volume ratio between the concrete and reinforcing, the material type of the bars, and the orientation of the bars. ANSYS is able to visually display the orientation of the user-defined reinforcing as shown in Figure 46, where the red lines are the reinforcing smearing and the blue lines are the element edge lines. The prestressing in the girder was defined in the real constant of the post-tensioned bars as an initial strain. The cross-sectional area of the post-tensioned steel was also defined using the real constant command. For the contact elements, a command called “KEYOPT” was used to specify the behavior of the contact. For this research, the behavior of the contact was set to be “always bonded” in order to replicate the composite behavior of the girder and deck. The corresponding real constants that were used in this research are the normal penalty stiffness factor (FKN) and the initial contact closure (ICONT).

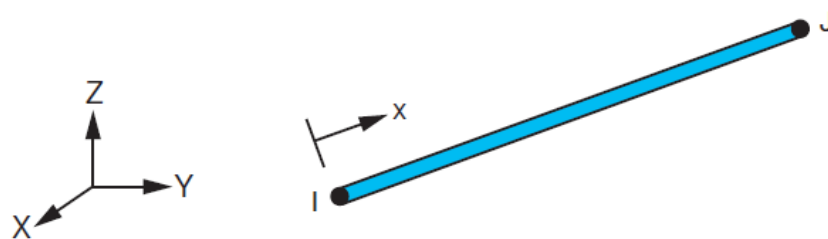


Figure 44 Geometric Shape for LINK8

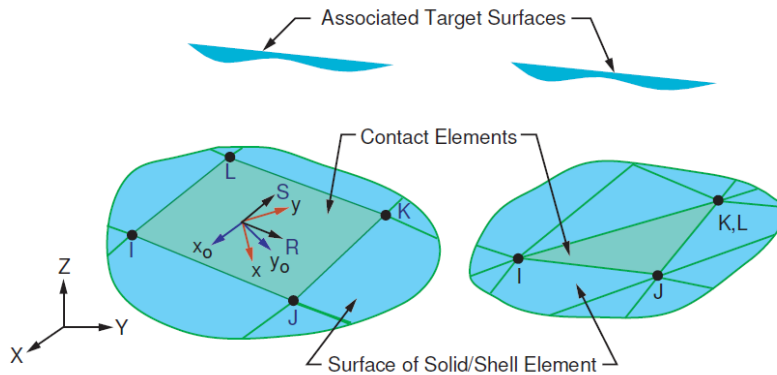


Figure 45 Geometric Shape for CONTA173&TARGE170

Prototype

Some modifications were contained in the prototype of the model in comparison to the actual girder in order to model the girder behavior and optimize the analysis. The taper section between the box end and I-shape sections in the actual girder was simplified in the model with an extended box section of 0.076 m (3 in.). This modification minimized the number of shape angles within the volume so that the quality of meshing in ANSYS was able to be optimized. Two stiff anchorage steel plates were attached at each end of the girder in the model as well as the each end of the post-tensioned rods to demonstrate the locking that kept the post-tensioned rods in tension for the actual girder.

Running the model

After the model was developed and material properties were assigned properly, the model was meshed into small elements with a defined size. The size of the element varied depending on the meshing quality and volume shape. For this research, the size of elements was defined as 2, which means 50.8 mm (2 in.) wide element. However, the elements were not necessarily in this exact size and a cubical shape because the shapes of volumes were not all rectangular. The corners of elements were nodes, similar to keypoints. Boundary conditions were defined on the

node at the support. In order to perform a pin-roller supported girder analysis, only one row of nodes at each support was assigned the boundary condition in order to replicate the performance of the elastomeric pad in the experiment. The applied force was evenly distributed to the nodes at the top of bearing plate on the girder.

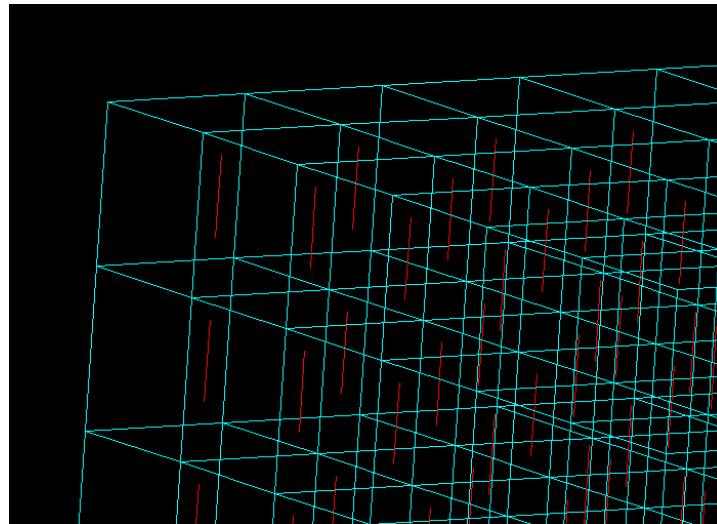


Figure 46 Reinforcing smearing in the deck

After meshing, the girder model was then loaded using a time step range from 1 to 100, which corresponded to the percentage of the predefined load. Each time step was automatically calculated in ANSYS based on the convergence of the previous time step. The predefined load was intentionally set higher than the experimental capacity for each test so that the model was able to perform to failure before a time of 100.

ANSYS Models

The same girder model was used to replicate each experiment test performed in the laboratory. The respective tests were analyzed by modifying the position of the load in the model to match the corresponding experimental load location. The predefined load was also modified accordingly. The load was incrementally applied on the model until convergence occurred and

the model reached the theoretical ultimate failure. In ANSYS, the failure of the model was achieved by concrete crushing having excessive element deflections. The result from each of the finite-element analyses will be discussed in the following section along with the comparison with the experimental result.

ANSYS model for 1-d test

Each girder model was prestressed by attributing an initial strain on each post-tensioned rods. Figure 47 shows the girder camber at the initial state due to prestressing before the load was applied. For the finite-element analysis that replicated the 1-*d* test, the graphical model setting is shown in Figure 48. The triangle symbols at the girder ends represent the support condition, where the red arrows represent the loading and its direction. In order to ensure that the model was representative of the actual experimental tests, three checks had to be satisfied, which were the crack propagation, failure mode, and the load-deflection relationship.

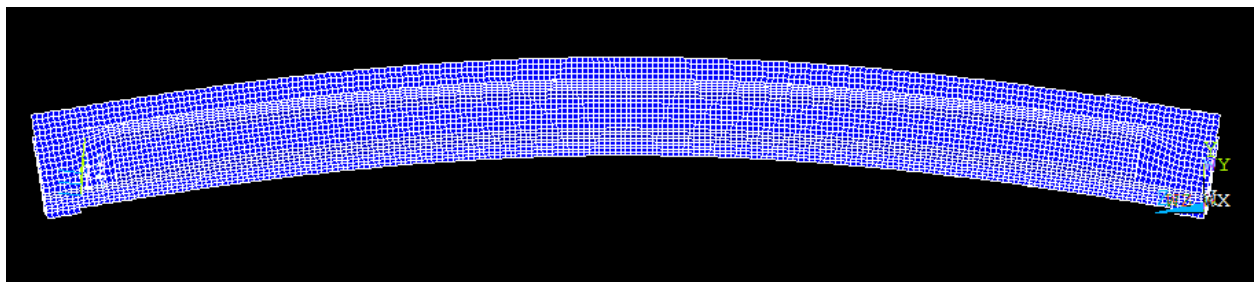


Figure 47 Initial deformation due to prestressing

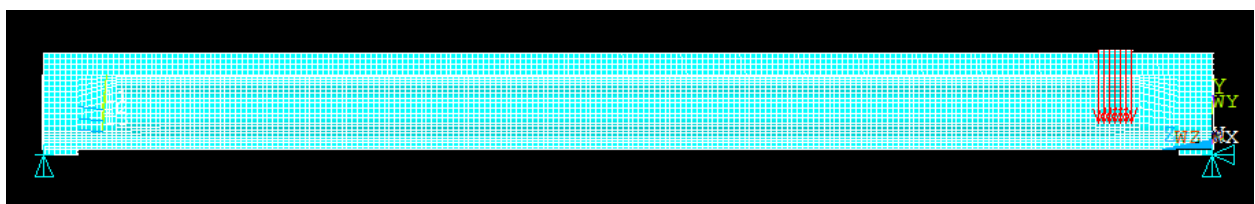


Figure 48 Elevation view of the 1-d test FEM

ANSYS has the capability of displaying the cracked and crushed concrete elements at different time step of loading. Figure 49 shows a comparison of the 1-*d* experiment test and the finite-element model for crack propagation near the location of loading before rupture. The cracks under the location of loading appeared vertically in both the experimental and FEM results, which showed that the crack was due to flexural failure. The crack propagation on the entire model is also shown in Figure 50, where most of the cracks appeared vertically. However, there were diagonal cracks at the short end similar to the result from the 1-*d* physical test.

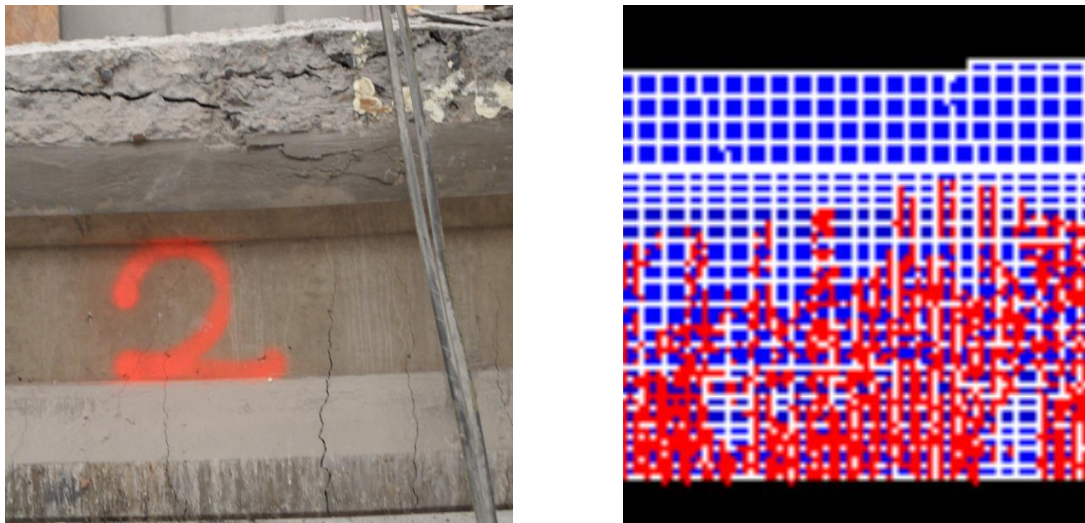


Figure 49 Comparison of the crack propagation near loading location for 1-d test (left: G3-1d(a), right: FEM)

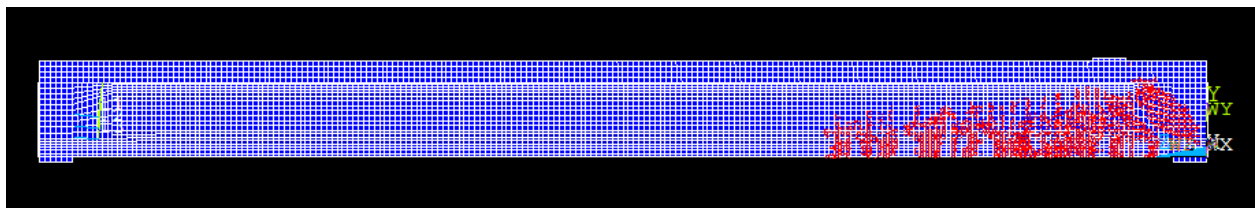


Figure 50 Overview of cracks from the 1-d test FEM

In addition, the load vs. deflection curve was the compared to ensure that the FEM properly replicate the experiment. The resultant displacement of the model was exported from

ANSYS and further plotted to compare with the experimental result. The location of the displacement in the FEM was identical to the experiment test, which was at the bottom of the girder directly underneath the loading point. This was where the string pot was instrumented during the experiment. The comparison of the results for the 1-*d* test is shown in Figure 51, where the result from the G2-1d(a) was selected because this test was performed with the full span length. However, only the shear vs. deflection relationship was compared because the shear capacity was more critical for shear tests. As shown in Figure 51, the measured maximum shear capacity was 1428 kN (321 kip), whereas the FEM resulted for the maximum shear capacity was 1388 kN (312 kip), which was 97.2% of the experimental result. Also, the stiffness of the girder from both tests was similar through the similarity of the slope of the curve shown in Figure 51.

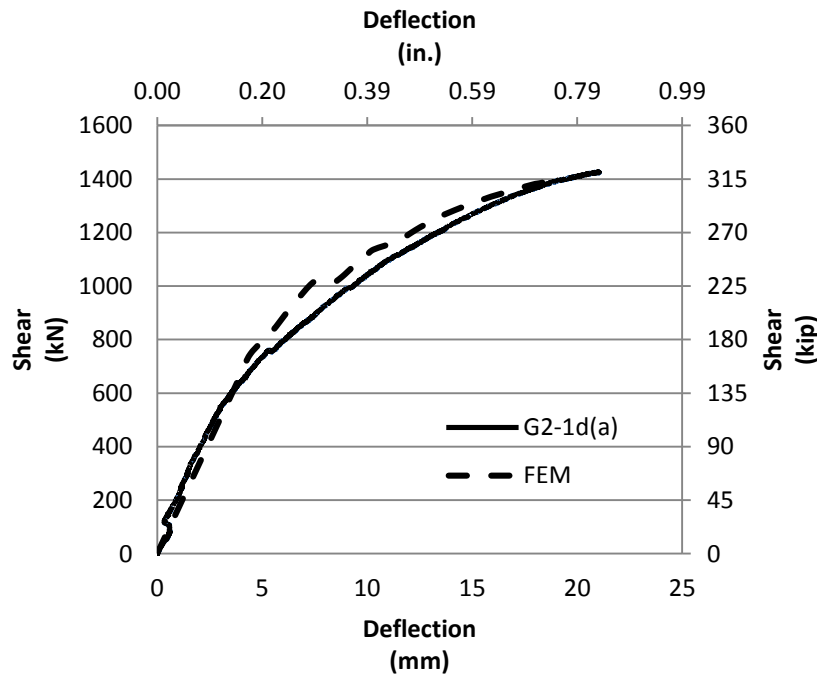


Figure 51 Shear vs. deflection curve comparison for 1-d test

ANSYS model for 2-d & 4-d test

The same model was used to analyze the 2-d and 4-d tests that was used for the 1-d test. The only modification was changing the location of loading to match the corresponding physical tests. The similar ANSYS setups for the 2-d and 4-d tests are shown in Figure 52 and 53. The support condition remained consistent throughout all the analyses.

The FEM results for the 2-d and 4-d tests were compared to the experimental result similar to the 1-d test in regards to the crack propagation and shear-deflection relationship. For the comparison of the crack propagation, the results from the FEM for the 2-d and 4-d tests were similar. Diagonal cracks appeared at the short end of the girder in both tests. Figure 54 and 55 show the comparison of the crack propagation near the location of loading between the FEM and experimental result for the 2-d and 4-test, respectively. From the overview of the crack propagation results from the FEM for the 2-d and 4-d test through Figure 56 and 57, most cracks appeared vertically, where some diagonal cracks appeared at the web at the short end of the girder. In addition, the cracks in the 4-d test were propagated to a longer distance in comparison to the 2-d test. It is believed that the flexural failure had a higher influence in the 4-d test compared to the 2-d test.

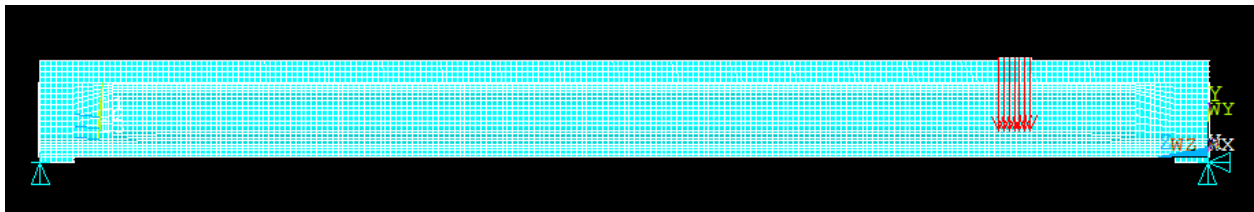


Figure 52 Elevation view of the 2-d test FEM

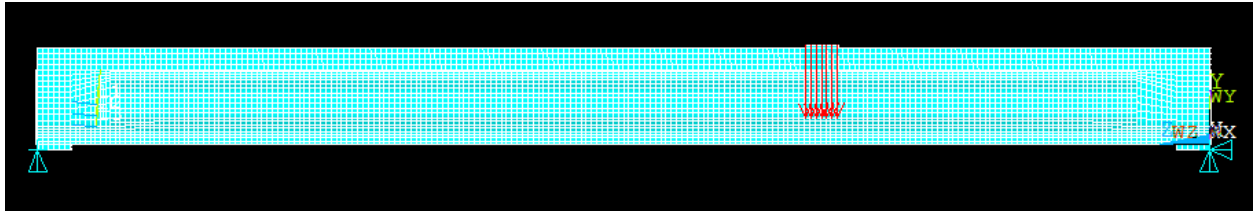


Figure 53 Elevation view of the 4-d test FEM

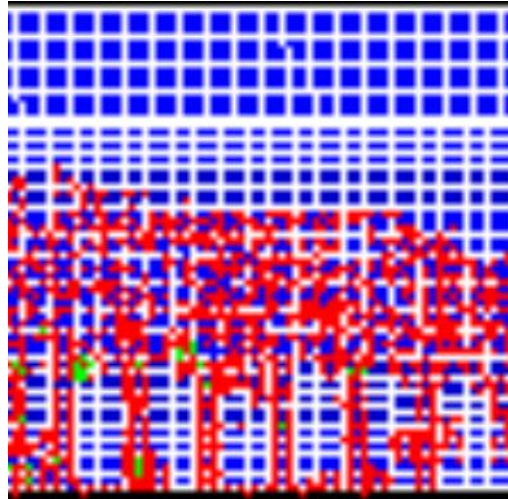


Figure 54 Comparison of the crack propagation near loading location for 2-d test (left: G1-2d(a), right: FEM)

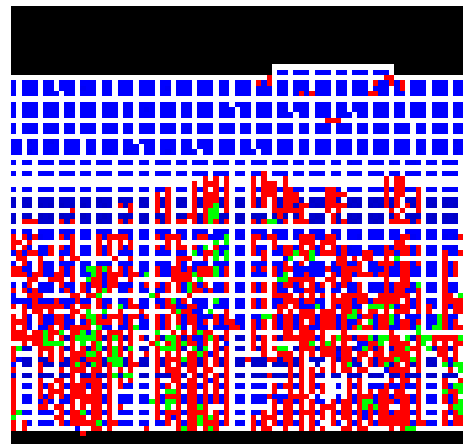


Figure 55 Comparison of the crack propagation near loading location for 4-d test (left: G7-4d(a), right: FEM)

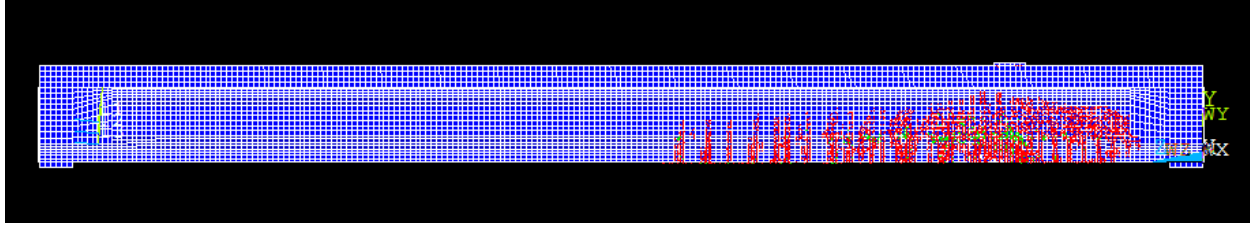


Figure 56 Overview of cracks from the 2-d test FEM

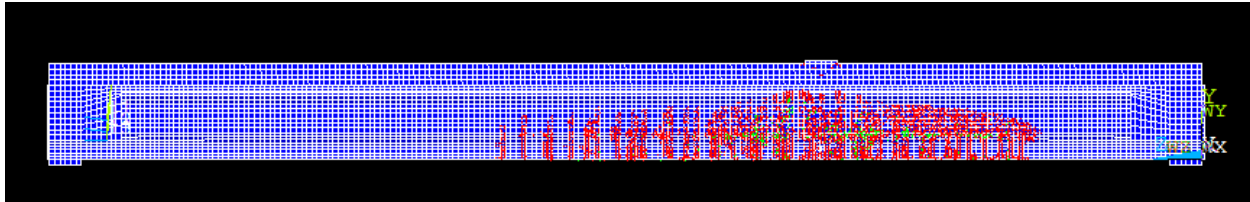


Figure 57 Overview of cracks from the 4-d test FEM

In addition to cracking, a comparison of the shear-deflection relationship was also performed for the 2-d and 4-d tests, which is shown in Figure 58 and 59. For the 2-d test, the stiffness of the girder from the experimental test was close except that the FEM underpredicted the stiffness after cracking. Hence, the shear capacity from the FEM was underpredicted as well in comparison to the experimental result. The shear capacity from the FEM was 756 kN (170 kip) whereas the experiment results had a maximum shear capacity of 805 kN (181 kip). The FE capacity was 93.9% of the experimental capacity. On the other hand, the stiffness of the girder was well modeled by the 4-d test FEM as shown in Figure 59. The figure also shows that they have similar shear capacities, which were 423 kN (95 kip) from the FEM and 418 kN (94 kip) from the experimental result. The FE capacity was 101% of the experimental capacity. However, the FEM overpredicted the deflection at failure by approximately 5.08 mm (0.2 in.).

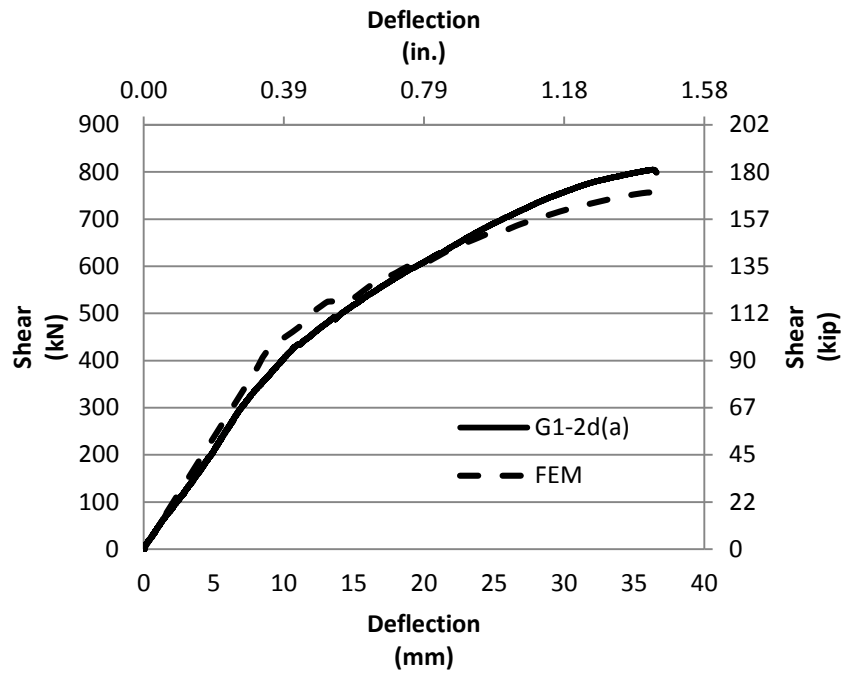


Figure 58 Shear vs. deflection curves comparison for 2-d test

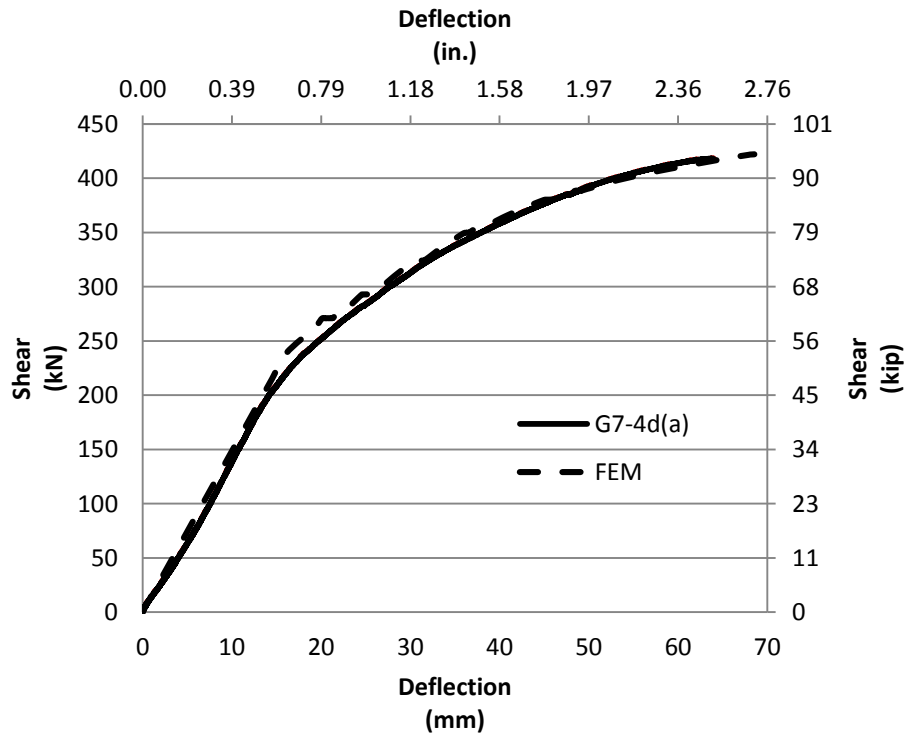


Figure 59 Shear vs. deflection curves comparison for 4-d test

ANSYS model for mid-span test

The midspan test was modeled with the same FEM that was used for the shear comparisons. The location of loading was moved to the middle of the span as shown in Figure 60 to replicate the midspan test. The load was incrementally applied until the girder reached the theoretical ultimate failure. Figure 61 shows the comparison of the crack propagation between the experimental and FEM results. The crack propagation from the midspan test FEM, as shown in Figure 62, appeared similar as the result from the 4-d test model. For this test the crack distribution levels were similar, however, there were lesser diagonal cracks appearing at the web during the midspan test. By comparing the appearance of cracks from all the FEM results, it is believed that the shear did not have a significant influence for the midspan test in comparison to the shear tests due to the minimal amount of diagonal cracks developing during the midspan test. The controlling factor on cracking in the FEM was the tensile strength of the girder. The actual tensile strength of the girder concrete was difficult to determine through cored concrete. The tensile strength used in the FEM was initially assumed to be approximately 10% of the measured compressive strength and it was further adjusted by matching the cracking scheme to the experimental result.

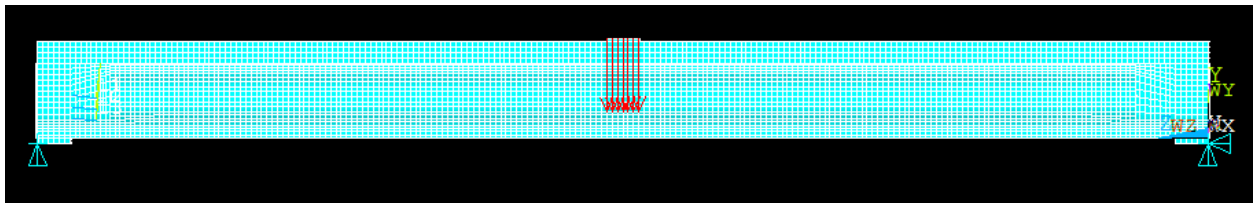


Figure 60 Elevation view of the midspan test FEM

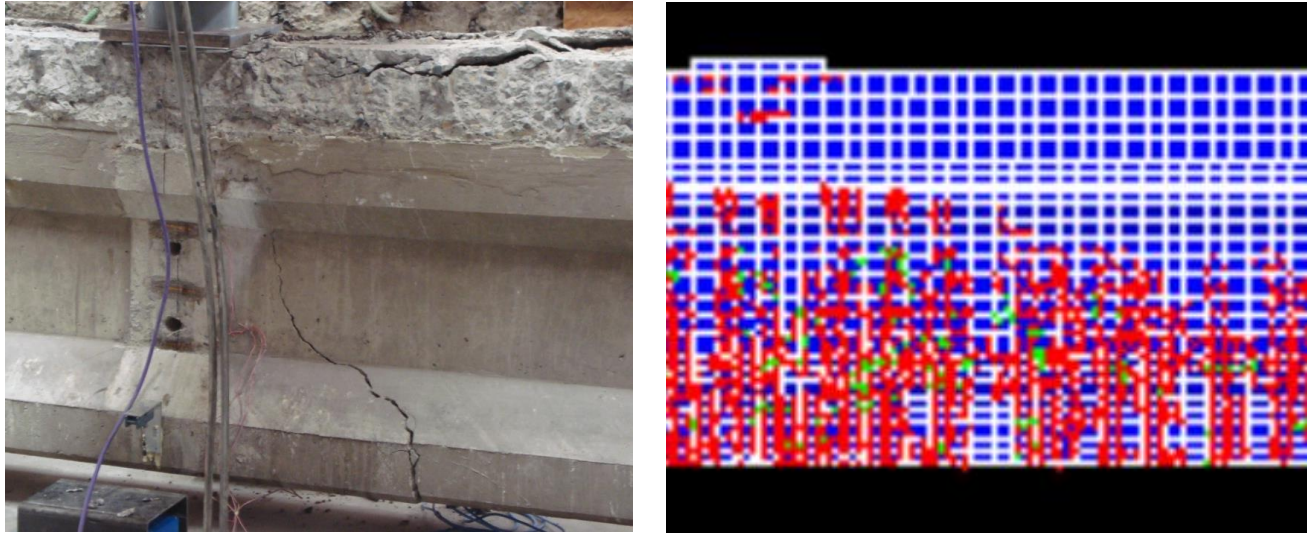


Figure 61 Comparison of the crack failure near loading location for midspan test (left: G8-midspan, right: FEM)

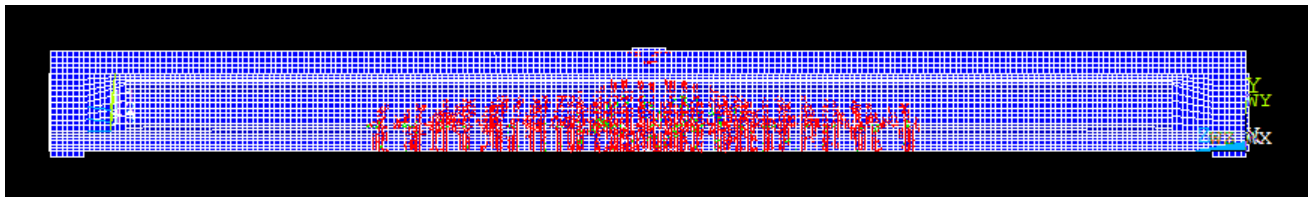


Figure 62 Overview of cracks from the midspan test FEM

Since the flexural failure governed for the midspan test, the relationship between the moment and deflection was compared as shown in Figure 63. The moment capacities from the FEM and experimental results were approximately the same. The maximum moment capacity from the experimental result was 1554 kN-m (1146 kip-ft), where the FEM predicted the maximum moment capacity of 1552 kN-m (1145 kip-ft). The FE capacity was within 99.9% of the experimental capacity. However, the FEM predicted maximum deflection at the midspan was overpredicted in comparison to the experimental result by approximately 7.62 mm (0.3 in.). Moreover, the actual girder was slightly stiffer than the model by comparing the slope of the curves in Figure 63.

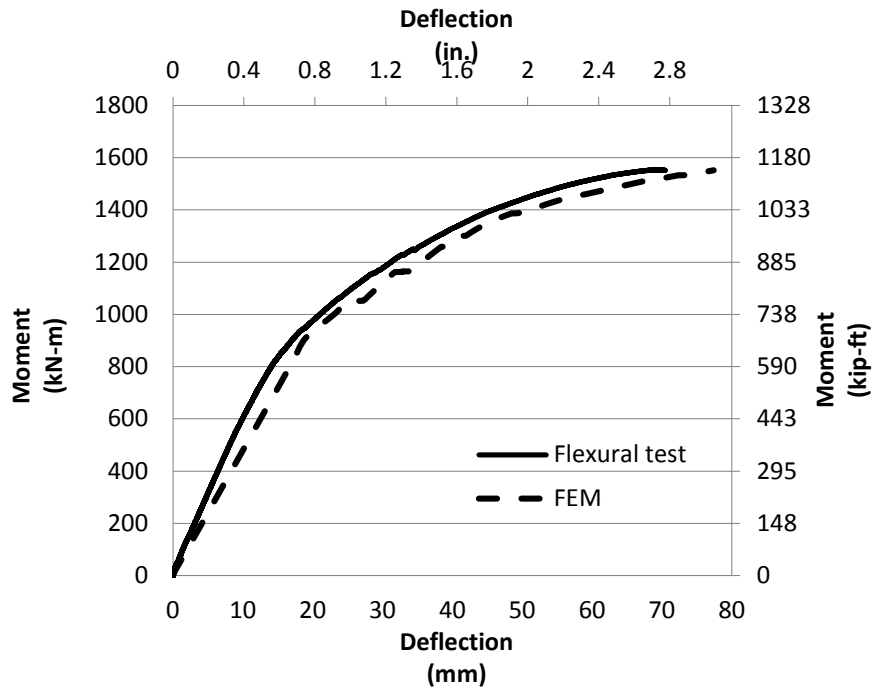


Figure 63 Moment vs. deflection curves comparison for midspan test

Summary of ANSYS models

Overall, the ANSYS model accurately predicted the load capacity of the girder, for all tests, to within 6%. The detail comparison is shown in Table 13. The model also predicted similar stiffnesses in comparison to the actual tested girders. However, the strength and modulus of elasticity of the concrete were modified in comparison to the measured value from the cylinder test. The strength of the concrete for the deck and girder were increased by 45% from the measured value in order to obtain a comparable result to the experiment. The stiffness of the concrete was also reduced in the model. There were two possible reasons to produce this inconsistency. The strength of the concrete from the cylinder test was possibly damaged with the coring process which resulted in a lower compressive strength. Alternatively the ANSYS model

may be needed to be modeled in a more detail configuration using discrete elements for the reinforcing steel in the concrete.

By using the same model for each test with identical material properties, ANSYS provided an accurate prediction on load capacity and deflection as well as the crack propagation.

Table 13 Comparison of the capacity between the experimental and FEM results

	Experimental	FEM	% Difference
1-d test (Shear)	1428 kN (321 kip)	1388 kN (312 kip)	-2.8%
2-d test (Shear)	805 kN (181 kip)	756 kN (170 kip)	-6.1%
4-d test (Shear)	418 kN (94 kip)	423 kN (95 kip)	1.2%
Midspan (Moment)	1554 kN-m (1146 kip-ft)	1552 kN-m (1145 kip-ft)	-0.1%

CONCLUSION

Four 50-year-old post-tensioned girders were tested to determine the prestress losses, shear and moment capacities. The results were then compared to the AASHTO LRFD Specification and an ANSYS finite-element model.

The measured prestress losses of the girders was 35% on average, where the AASHTO LRFD Specification predicted an upper and lower bound of the prestress losses with the Simplified Method and Refined Method. The prestress losses predicted using the Simplified Method was 40.4% and 29.8% using the Refined Method. The Simplified Method provided a more conservative result as expected. It is interesting to notice that the prestress losses of the post-tensioned girders in this research was approximately 35% after 50 years of service, which was closed to the assumed prestress losses in Eder et al., 2005, for the 50-year-old post-tensioned bridge girder. The AASHTO 2012 obtained a fairly accurate prediction on determining the moment capacity in comparison to the experimental result. The average percent difference between both results was approximately 5.5%. However, the shear capacity was overly predicted using the procedures in the AASHTO LRFD Design in comparison to the shear tested result. The percent difference for the 1-d, 2-d, and 4-d tests was 38.9%, 39.5%, and 13.8%, respectively. The average percent difference was approximately 31%. This overprediction indicated that the girders were failed in a flexural manner, which matched the compressive failure on the girders during the experiments.

The ANSYS model was able to obtain a comparable result in terms of modeling the stiffness of the girder, the shear and moment capacity for each test, and the deflection. The percent difference in capacity between the experimental and FEM results was 2.8% for the 1-d test, 6.1% for the 2-d test, 1.2% for the 4-d test, and 0.1% for the midspan test. This was less

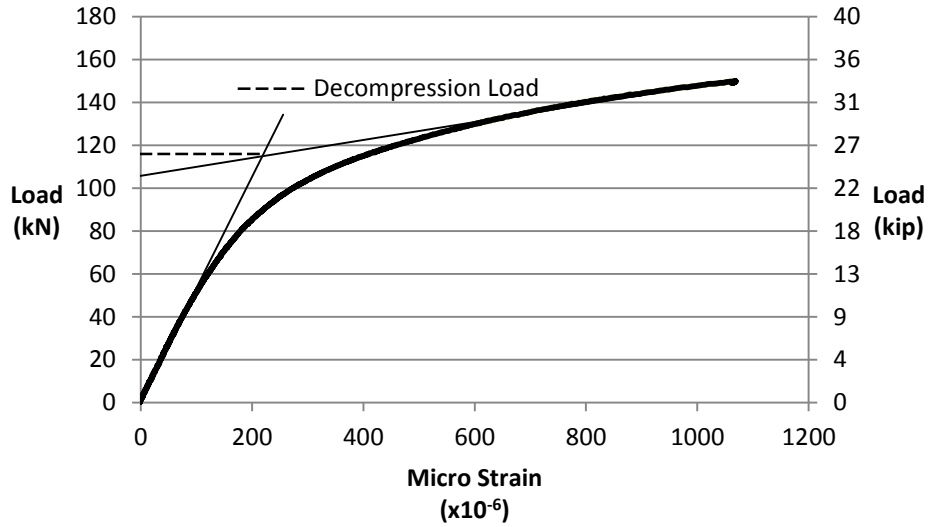
than 3% on average. However, the concrete material properties in the model were increased significantly comparing to the actual properties. Further understanding on ANSYS modeling may be required to idealize the FEM result.

REFERENCE

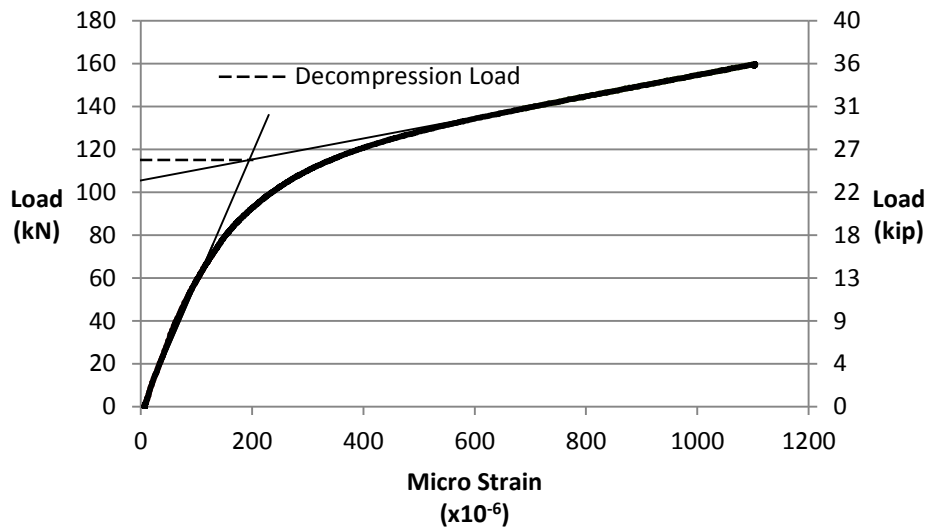
- AASHTO. (2012). AASHTO LRFD Design Manual. AASHTO, Washington, D.C.
- ANSYS, Inc. (2009). Element Reference. ANSYS, Canonsburg, PA.
- Barr, P. J., Kukay, B. M., and Halling, M. W. (2008), "Comparison of Prestress Losses for a Prestress Concrete Bridge Made with High-Performance Concrete." *Journal of Bridge Engineering*, 468-475.
- Dahmani, L., Khennane, A., and Kaci, S. (2010), "Crack Identification in Reinforced Concrete Beams Using ANSYS Software." *Strength of Materials*, 42(2), 232-240.
- Eder, R. W., Miller, R. A., Baseheart, T. M., and Swanson, J. A. (2005). "Testing of Two 50-Year-Old Precast Post-Tensioned Concrete Bridge Girders." *PCI Journal*, 90-95.
- Grace, N. F., and Ross, B. (1996), "Dynamic Characteristic of Post-Tensioned Girder with web openings." *Journal of Structural Engineering*, 643-650.
- Nayal, R., Peterman, R. J., and Esmaily, A. (2010), "Parametric Study of Posttensioned Inverted-T Bridge System for Improved Durability and Increased Span-to-Depth Ratio." *Journal of Bridge Engineering*, 731-739.
- Pessiki, S., Kaczinski, M., and Wescott, H. H. (1996). "Evaluation of Effective Prestress Force in 28-Year-Old Prestressed Concrete Bridge Beams." *PCI Journal*, 78-89.
- Tabatabai, H., and Dickson, T. J. (1993). "Structural Evaluation of a 34-Year-Old Precast Post-Tensioned Concrete Girder." *PCI Journal*, 50-63.

APPENDIX A. Cracking Moment Test Data

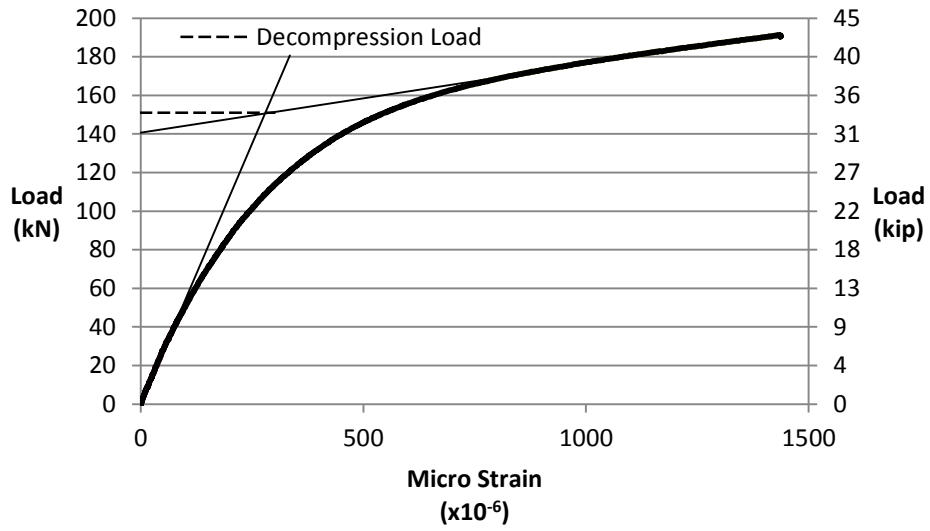
Girder #1 Cracking Test



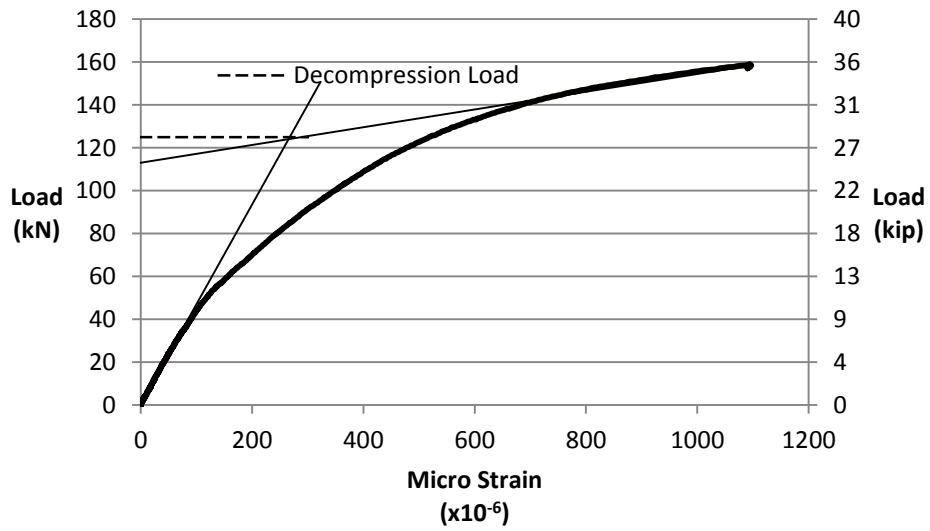
Girder #2 Cracking Test



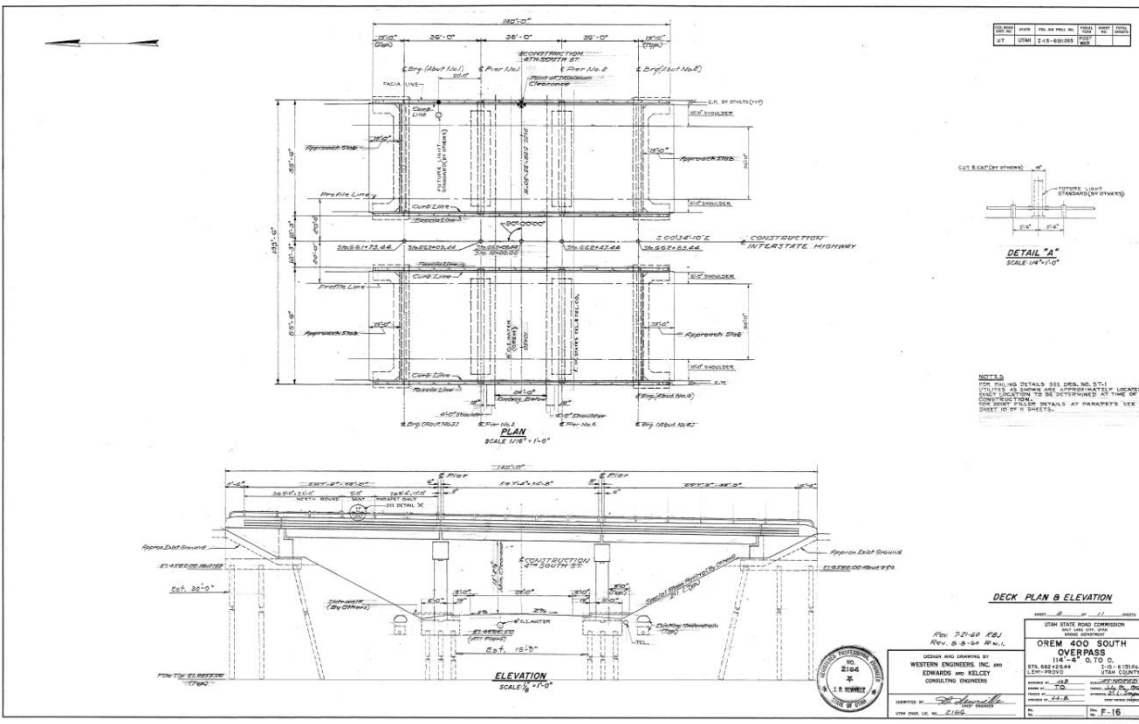
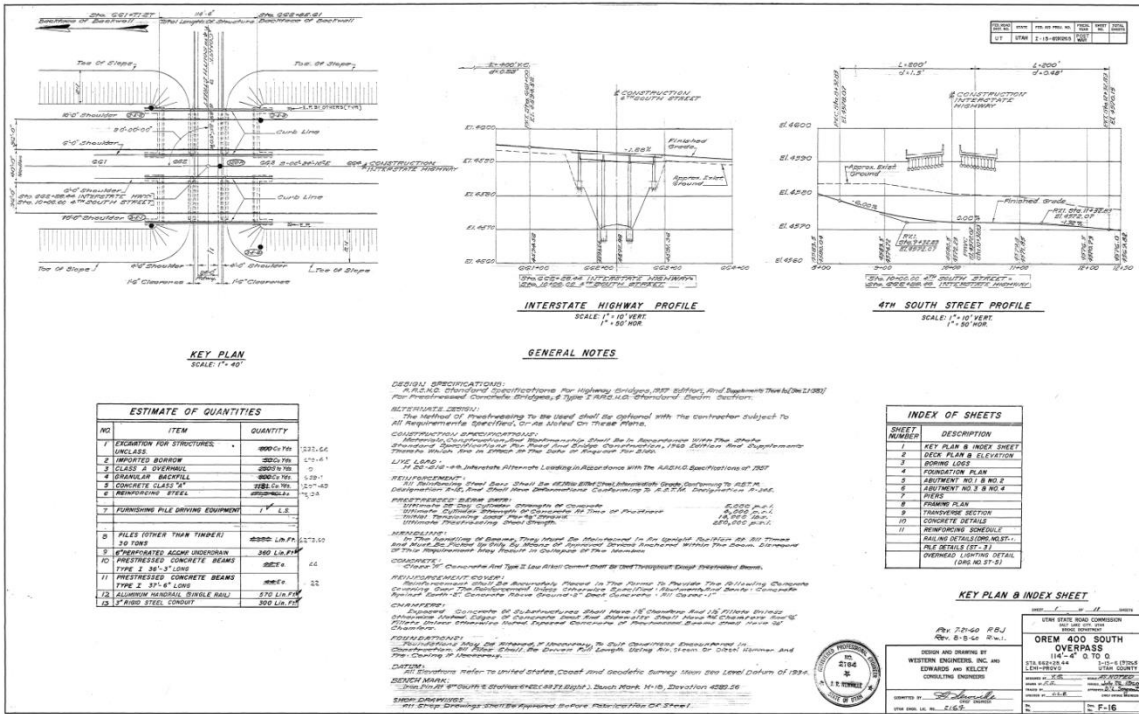
Girder #7 Cracking Test

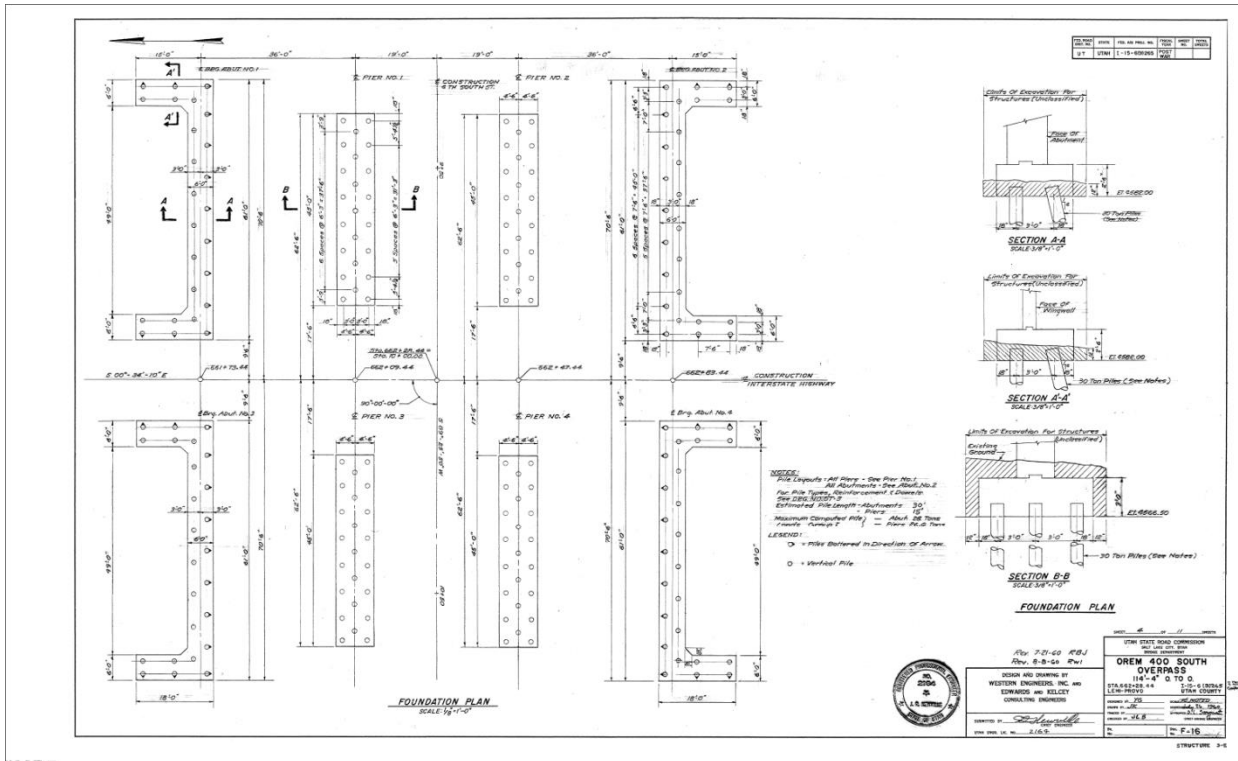
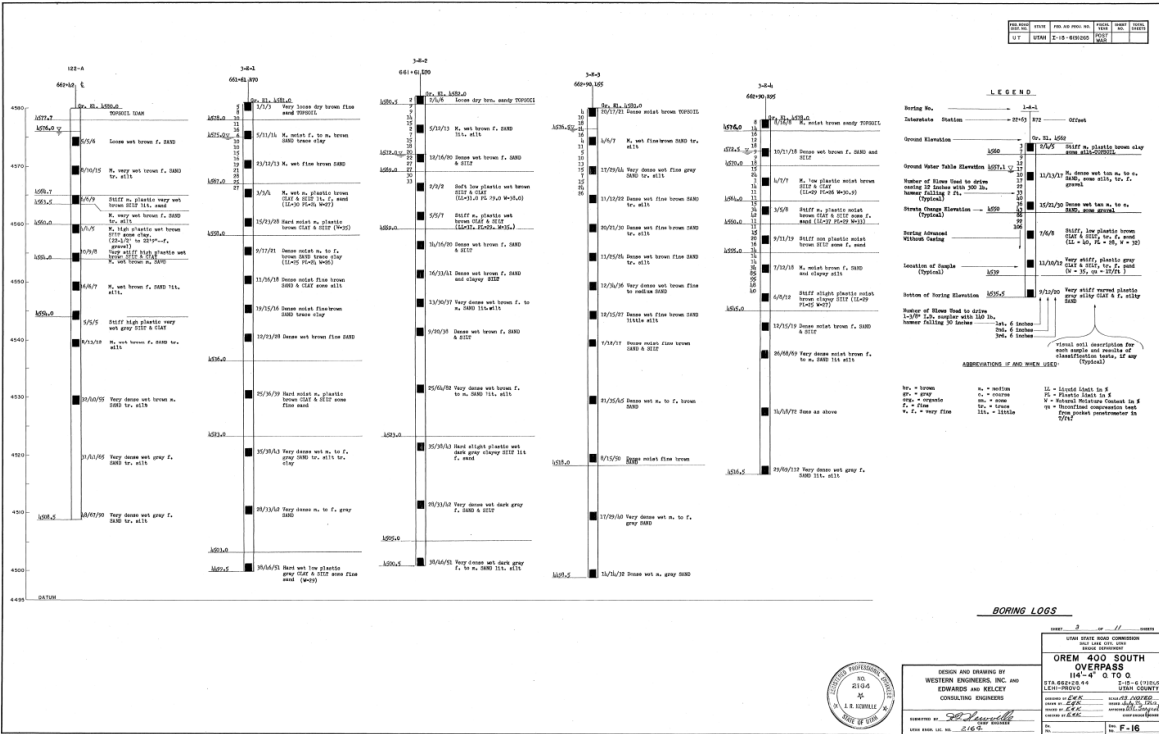


Girder #8 Cracking Test



APPENDIX B. Bridge Plans





APPENDIX C. ANSYS Model Code

<pre> finish /clear /title,GIRDER /VIEW,1,1,1,1 ! Window 2 ISO (isometric projection) view /prep7 !Units in Kips and inches Es=29000 Emus=0.3 fy=60 Eps=29000 fpsy=140 Esu=5000000 fyu=10000 Ec=4500 fc=10.5 ft=1.2 Emuc=0.2 Ecd=2000 !Deck fcd=9.7 ftd=1.1 Emucd=0.2 MP,EX,1,Ec MP,PRXY,1,Emuc MP,DENS,1,1.188E-4 TB,CONCR,1 TBDATA,,0.3,1,ft,fc !see element types MP,EX,2,Es MP,PRXY,2,Emus TB,BISO,2 TBDATA,,fy,2.9 MP,EX,3,Eps MP,PRXY,3,Emus TB,BISO,3 TBDATA,,fpsy,1500 MP,EX,4,Esu </pre>	<pre> MP,PRXY,4,0 TB,BISO,4 TBDATA,,fyu,500000 MP,EX,5,Ecd MP,PRXY,5,Emucd MP,DENS,5,1.188E-4 TB,CONCR,5 TBDATA,,0.3,1,ftd,fcd R,1 R,3,1,0.003 !post-tensioned steel R,4,2,0.011,90 !6"oc shear reinforcements R,5,2,0.0056,90 !12"oc shear reinforcements R,6,2,0.018,90 !deck reinforcements R,8,,0.01,,1E-10 R,10,2,0.022,90,,2,0.009 RMORE,,90 !6"oc at box end with double reinf. ET,1,Solid65 ET,2,Link8 ET,3,Solid45 ET,4,Targe170 ET,5,CONTA173 KEYOPT,5,4,2 KEYOPT,5,2,2 KEYOPT,5,6,0 KEYOPT,5,7,0 KEYOPT,5,8,2 KEYOPT,5,9,1 KEYOPT,5,11,0 KEYOPT,5,12,5 !Volume K,1,0,0 K,2,2,0 K,3,7,0 K,4,9,0 K,5,14,0 K,6,16,0 K,7,0,5 </pre>
--	--

K,8,2,7	v,7,1,2,8,21,15,16,22
K,9,14,7	v,37,33,34,38,51,47,48,52
K,10,16,5	v,35,29,30,36,49,43,44,50
K,11,7,28	
K,12,9,28	vsel,all
K,13,2,28	vsel,u,loc,x,7,9
K,14,14,28	WPOFF,,,12
	VSBW,all
Kgen,2,1,14,1,,,27	WPOFF,,,411
Kgen,2,1,14,1,,,408	VSBW,all
Kgen,2,1,14,1,,,435	WPSTYL,DEFA
K,57,2,24,27	vsel,all !cut for different stirrup spacing
K,58,14,24,27	WPOFF,,,27
K,59,5,21,27	VSBW,all
K,60,11,21,27	WPOFF,,,34.5
K,61,5,10,27	VSBW,all
K,62,11,10,27	WPOFF,,,312
K,63,5,0,27	VSBW,all
K,64,11,0,27	WPOFF,,,34.5
K,65,5,28,27	VSBW,all
K,66,11,28,27	WPSTYL,DEFA
Kgen,2,57,66,1,,,381	!Bearing plates
	*DO,i,0,423,423
K,77,2,36	BLOCK,0,2,0,-2,0+i,12+i
K,78,14,36	BLOCK,2,7,0,-2,0+i,12+i
K,79,2,36,435	BLOCK,7,9,0,-2,0+i,12+i
K,80,14,36,435	BLOCK,9,14,0,-2,0+i,12+i
	BLOCK,14,16,0,-2,0+i,12+i
v,11,3,4,12,53,45,46,54 !middle long rectangle	vsel,s,loc,y,-2,0
	vsel,r,loc,z,0+i,12+i
v,13,2,3,11,27,16,17,25	vglue,all
v,12,4,5,14,26,18,19,28	*ENDDO
v,54,46,47,56,40,32,33,42	vsel,all
v,55,44,45,53,41,30,31,39	vglue,all
v,26,18,64,66,40,32,74,76 !side rectangles in the middle	!Rods plates
v,65,63,17,25,75,73,31,39	BLOCK,5,7,0,28,-0.75,0
	BLOCK,7,9,0,28,-0.75,0
v,62,64,20,24,72,74,34,38 !side trapezoid in the middle	BLOCK,9,11,0,28,-0.75,0
v,21,15,63,61,35,29,73,71	BLOCK,5,7,0,28,435,435.75
	BLOCK,7,9,0,28,435,435.75
v,66,60,58,28,76,70,68,42	BLOCK,9,11,0,28,435,435.75
v,27,57,59,65,41,67,69,75	vsel,all
	vglue,all
	!infinite stiff side plates
v,9,5,6,10,23,19,20,24 !side trapezoid at the end	vsel,s,loc,z,0,27
	vsel,a,loc,z,412,435

WPROTA,,,-90
 WPOFF,,,-5
 VSBW,all
 WPOFF,,,-6
 VSBW,all
 WPSTYL,DEFA

 !Parabolic post-tensioned rods
 vsel,all
 WPROTA,,,-90
 WPOFF,,,-8
 VSBW,all
 WPSTYL,DEFA

 vsel,all

 !CUTTING for Rods
 INC=21.75
 *DO,PR,-217.5,217.5-INC,INC
 *IF,PR,NE,217.5-INC,THEN
 WPOFF,,PR+217.5+INC
 vsel,s,loc,x,7,9
 VSBW,all
 WPSTYL,DEFA
 *ENDIF
 *IF,PR,EQ,-217.5,THEN
 vsel,s,loc,z,(PR+217.5-5),(PR+217.5+INC)
 *ELSEIF,PR,EQ,217.5-INC,THEN
 vsel,s,loc,z,(PR+217.5),(PR+217.5+INC+5)
 *ELSE
 vsel,s,loc,z,(PR+217.5),(PR+217.5+INC)
 *ENDIF
 vsel,r,loc,x,7,9
 !Top Rod
 WPOFF,,PR+217.5

 SP1=(PR*PR)/3638.94217084792+1.5+2*1.375

 SP2=((PR+INC)*(PR+INC))/3638.9421708479
 2+1.5+2*1.375
 WPROTA,,,-90
 WPOFF,,SP1
 *AFUN,DEG
 WPROTA,,ATAN((SP1-SP2)/INC)
 VSBW,all
 WPSTYL,DEFA
 !MIDDLE ROD
 WPOFF,,PR+217.5

 SP3=(PR*PR)/4883.22576355819+1.5+1.375

SP4=((PR+INC)*(PR+INC))/4883.2257635581
 9+1.5+1.375
 WPROTA,,,-90
 WPOFF,,SP3
 *AFUN,DEG
 WPROTA,,ATAN((SP3-SP4)/INC)
 VSBW,all
 WPSTYL,DEFA
 !BOTTOM ROD
 WPOFF,,PR+217.5
 SP5=(PR*PR)/7073.83158449819+1.5

 SP6=((PR+INC)*(PR+INC))/7073.8315844981
 9+1.5
 WPROTA,,,-90
 WPOFF,,SP5
 *AFUN,DEG
 WPROTA,,ATAN((SP5-SP6)/INC)
 VSBW,all
 WPSTYL,DEFA
 *ENDDO

 Block,2,14,28,36,0,435 !concrete Deck

 !MOVE THIS BLOCK TO MOVE LOAD
 BLOCK,2,14,36,37,72-6,72+6 !midspan
 test:217.5,1-d:36,2-d:72,4-d:144

 vsel,s,loc,y,28,37
 vglue,all

 vsel,s,loc,z,0,27
 vsel,a,loc,z,408,435
 vsel,r,loc,y,0,28
 vatt,1,10,1 !box end

 vsel,s,loc,z,27,61.5
 vsel,a,loc,z,373.5,408
 vsel,r,loc,y,0,28
 vatt,1,4,1 !near end
 concrete 6" oc

 vsel,s,loc,z,61.5,373.5
 vsel,r,loc,y,0,28
 vatt,1,5,1 !Middle
 concrete 12" oc

 vsel,s,loc,z,-0.75,0
 vsel,a,loc,z,435,435.75
 vatt,4,1,3

```

!Assign properties and mesh the rods
*DO,PR,-217.5,217.5-INC,INC

SP1=(PR*PR)/3638.94217084792+1.5+2*1.375

SP2=((PR+INC)*(PR+INC))/3638.9421708479
2+1.5+2*1.375

SP3=(PR*PR)/4883.22576355819+1.5+1.375

SP4=((PR+INC)*(PR+INC))/4883.2257635581
9+1.5+1.375
  SP5=(PR*PR)/7073.83158449819+1.5

SP6=((PR+INC)*(PR+INC))/7073.8315844981
9+1.5

!Top rod
  *IF,PR,EQ,-217.5,THEN
    lsel,s,loc,z,(PR+217.5-5),(PR+217.5+INC)
  *ELSEIF,PR,EQ,217.5-INC,THEN
    lsel,s,loc,z,(PR+217.5),(PR+217.5+INC+5)
  *ELSE
    lsel,s,loc,z,(PR+217.5),(PR+217.5+INC)
  *ENDIF
  lsel,r,loc,x,8
  *AFUN,DEG
  LOCAL,11,0,8,SP1,PR+217.5,,ATAN((SP1-
SP2)/INC)
  lsel,r,loc,y,0
  latt,3,3,2
  ESIZE,2
  LMESH,all
  CSYS,0
!Mid rod
  *IF,PR,EQ,-217.5,THEN
    lsel,s,loc,z,(PR+217.5-5),(PR+217.5+INC)
  *ELSEIF,PR,EQ,217.5-INC,THEN
    lsel,s,loc,z,(PR+217.5),(PR+217.5+INC+5)
  *ELSE
    lsel,s,loc,z,(PR+217.5),(PR+217.5+INC)
  *ENDIF
  lsel,r,loc,x,8
  *AFUN,DEG
  LOCAL,12,0,8,SP3,PR+217.5,,ATAN((SP3-
SP4)/INC)
  lsel,r,loc,y,0
  latt,3,3,2
  ESIZE,2
  LMESH,all

```

```

  CSYS,0
!Bottom rod
  *IF,PR,EQ,-217.5,THEN
    lsel,s,loc,z,(PR+217.5-5),(PR+217.5+INC)
  *ELSEIF,PR,EQ,217.5-INC,THEN
    lsel,s,loc,z,(PR+217.5),(PR+217.5+INC+5)
  *ELSE
    lsel,s,loc,z,(PR+217.5),(PR+217.5+INC)
  *ENDIF
  lsel,r,loc,x,8
  *AFUN,DEG
  LOCAL,13,0,8,SP5,PR+217.5,,ATAN((SP5-
SP6)/INC)
  lsel,r,loc,y,0
  latt,3,3,2
  ESIZE,2
  LMESH,all
  CSYS,0
*ENDDO

  vsel,s,loc,y,36,37
  vsel,a,loc,y,-2,0
  vatt,2,1,3

  vsel,s,loc,y,28,37
  vsel,a,loc,y,-2,0

  vsel,all
  vplot,all

  vsel,s,loc,y,-2,28
  esize,2
  vsweep,all

  esel,s,mat,,1
  nsle,s
  nsel,r,loc,y,28
  REAL,8
  TYPE,4
  ESURF

  vsel,s,loc,y,28,36
  vatt,5,6,1
  concrete
  !deck

  vsel,s,loc,y,28,37
  esize,2
  vsweep,all

  esel,s,mat,,5
  nsle,s

```

```
nselect, r, loc, y, 28
REAL, 8
TYPE, 5
ESURF
```

```
Allselect, all
!TAKES CORD SYSTEM BACK TO
DEFAULT POSITION
wpstyle, defa
```

```
NSELECT, S, LOC, Y, -2
NSELECT, R, LOC, Z, 435.5
d, all, ux
d, all, uy
```

```
NSELECT, S, LOC, Y, -2
NSELECT, R, LOC, Z, 0
d, all, ux
d, all, uz
d, all, uy
```

```
finish
```

```
/solu
```

```
Nselect, s, loc, y, 37
*Get, Ncount, node, 0, count
F=250
!midspan test: 150, 1-d: 400, 2-d: 250, 4-d: 160
```

```
f, all, Fy, -F/Ncount
```

```
allselect, all
cnvtol, f, , 0.05, 2, 0.01
nsubst, 200
outres, all, all
autots, 1
ncnv, 2
LNSRCH, AUTO
NLGEOM, OFF
```

```
neqit, 200
pred, on
time, 100
```

```
!Percent of the force you wanna go to
solve
```